

**FLEXIBLE NEURAL INTERFACES FOR
RECORDING AND STIMULATION OF
PERIPHERAL AND VISCERAL NERVES**

SANGHOON LEE

**A THESIS SUBMITTED FOR
THE DEGREE OF DOCTOR OF PHILOSOPHY**

**DEPARTMENT OF ELECTRICAL AND COMPUTER
ENGINEERING**

NATIONAL UNIVERSITY OF SINGAPORE

2017

Supervisors:

Associate Professor Chengkuo Lee, Main Supervisor
Assistant Professor Shih-Cheng Yen, Co-Supervisor

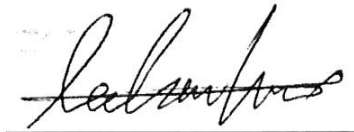
Examiners:

Associate Professor Ng, Vivian
Associate Professor Heng Chun Huat
Professor Jeffrey Da-Jeng Yao, National Tsing Hua
University

DECLARATION

I hereby declare that the thesis is my original work and it has been written by me in its entirety. I have duly acknowledged all the sources of information which have been used in the thesis.

This thesis has also not been submitted for any degree in any university previously.

A handwritten signature in black ink, appearing to read 'Sanghoon Lee', is written over a solid horizontal line.

SANGHOON LEE

January 2017

ACKNOWLEDGMENT

Firstly, I would like to express my heartfelt gratitude to my supervisor A/Prof. Chengkuo Lee and co-supervisor Assis. Prof. Shih-Cheng Yen for their continuous encouragement and excellent guidance in this research throughout my Ph. D. study. I gratefully thank Prof. Lee for his suggestions and valuable time for discussion. It has made my Ph.D. candidature a truly enriching experience. Furthermore, I would like to sincerely appreciate Prof. Yen and Prof. Nitish Thakor for unwavering support and valuable advice on neuroscience/engineering field.

I am especially grateful to SINAPSE and members including Dr. Ignacio Delgado-Martinez, Miss. Swathi Sheshadri, Dr. Kian Ann NG, Dr. Wendy Yen Xian Peh, Mr. Leong Khay Wai, Mr. Gil Gerald L. Gammad, and Prof. John S. Ho for their aid in various aspects of my experimental work and for use of their facilities.

In addition, I would like to express my sincere gratitude to all my colleagues and friends in CICFAR lab: Dr. Xiang Zhuolin, Dr. Chongpei, Dr. Pitchappa Prakash, Dr. Lokesh Dhakar, Dr. Hao Wang, Dr. Tao Wang, Mr. Qiongfeng Shi, Mr. Dihan Hasan, Jiahui Wang and so on. I appreciate Mrs. Chiow Mooi Ho and Mr. Chee Keong Koo for their continuous technical supports.

I could handle the PhD journey thanks to my great Korean friends and Mr. Manzar Siddik by their support and belief.

I am deeply indebted to my parents and my younger brother for their love, unlimited support, faith, and advice during my whole study period.

TABLE OF CONTENTS

ACKNOWLEDGMENT	1
SUMMARY	6
LIST OF TABLES	8
LIST OF FIGURES	9
LIST OF SYMBOLS	15
CHAPTER 1. INTRODUCTION	16
1.1. Background and Motivation.....	16
1.2. Research Objectives.....	19
1.3. Organization of Thesis.....	21
CHAPTER 2. OVERVIEW OF NEURAL INTERFACE	22
2.1. Neural interface.....	22
2.1.1. Regenerative Interface	25
2.1.2. Penetrating Interface.....	27
2.1.3. Intra-fascicular interface.....	28
2.1.4. Extra-neural Interface.....	30
2.2. Materials	32
2.2.1. PDMS (Polydimethylsiloxane).....	34
2.2.2. Parylene.....	34
2.2.3. Polyimide	35
2.3. Recent trend of neural interface	36
CHAPTER 3. FLEXIBLE EPINEURAL STRIP ELECTRODE (FLESE) FOR RECORDING IN SMAL NERVE.....	38
3.1. Motivation.....	38
3.2. Device Design.....	39
3.3. Methods	41
3.3.1. Device Fabrication	41
3.3.2. Device Releasing and Packaging	42
3.3.3. Au-CNT Nanocomposites coating	44
3.3.4. Electrochemical Impedance Spectroscopy (EIS) Characterization.....	46

3.3.5.	<i>Rat Preparation for in vivo test</i>	47
3.3.6.	<i>Physiological Characterization</i>	48
3.3.7.	<i>Stimulation Electrode and Recording Configuration</i>	48
3.3.8.	<i>Data Analysis</i>	49
3.4.	Results.....	49
3.4.1.	<i>In Vivo Recording (FLESE#1 and Bipolar Configuration) Elicited by a Concentric Bipolar Electrode</i>	49
3.4.2.	<i>In Vivo Recording (FLESE#2 and Differential Bipolar Configuration) Elicited by a Hook Electrode</i>	51
3.5.	Discussion.....	53
CHAPTER 4. FLEXIBLE SPLIT RING ELECTRODE FOR SELECTIVE STIMULATION AND NEURAL RECORDING		55
4.1.	Motivation.....	55
4.2.	Device Design.....	55
4.3.	Methods	57
4.3.1.	<i>Device Fabrication</i>	57
4.3.2.	<i>Electrochemical Impedance Spectroscopy (EIS) Characterization</i>	58
4.3.3.	<i>Physiological Characterization</i>	60
4.3.4.	<i>Data Analysis</i>	61
4.4.	Results.....	62
4.4.1.	<i>Selective stimulation of a sciatic nerve</i>	62
4.4.2.	<i>Neural recording with transverse differential bipolar configuration</i> ..	64
4.4.3.	<i>Acute recordings using commercial Pt cuff electrode</i>	67
4.5	Discussion.....	68
CHAPTER 5. FLEXIBLE AND ADJUSTABLE SLING ELECTRODE WITH SELECTIVE NERVE RECORDING AND STIMULATION		70
5.1.	Motivation.....	70
5.2.	Device Design	71
5.3.	Electrochemical Interface	73
5.3.1.	<i>Pt-black coated neural interfaces</i>	73
5.3.2.	<i>Electrochemical characterization</i>	74
5.4.	In vivo experiment	76

5.4.1. Neural recording of evoked CNAPs on sciatic nerves.....	76
5.4.2. Selective Stimulation on sciatic nerve.....	78
5.4.3. Hemodynamic measurement by functional photoacoustic microscopy (fPAM).....	81
5.5. Discussion.....	83
CHAPTER 6. BATTERY-FREE NEURAL INTERFACE USING FLEXIBLE SLING ELECTRODE AND TRIBOELECTRIC NANOGENERATOR (TENG)	85
6.1. Motivation.....	85
6.2. System Design	87
6.3. Device Configuration and Working Mechanism	88
6.4. In vitro characterization of triboelectric nanogenerators (TENGs)	90
6.5. In vivo test of triboelectric nanogenerators and neural interface	102
6.6. Discussion.....	104
CHAPTER 7. NOVEL FLEXIBLE CLIP (FNC) INTERFACE FOR NEUROMODULATION OF SMALL PERIPHERAL NERVES TOWARD BIOELECTRONIC MEDICINE	106
7.1. Motivation.....	106
7.2. Interface Design.....	108
7.3. Methods	111
7.3.1. Device fabrication.....	111
7.3.2. Iridium oxide coating	112
7.3.3. Electrochemical characterization.....	114
7.3.4. Physiological Characterization of bladder functions	115
7.3.5. Wireless Flexible Neural Clip.....	115
7.2. Stimulation of sciatic nerve branch for muscle activation	117
7.3. Stimulation of vagus nerve for controlling heart rate	121
7.4. Stimulation of pelvic nerve for modulation of bladder function.....	124
7.5. Wireless Stimulation of pelvic nerve for modulation of bladder function.....	130
7.5. Discussion	134
CHAPTER 8. CONCLUSION AND FUTURE WORK.....	138
8.1. CONCLUSION.....	138
8.2. Future Work.....	141
BIBLIOGRAPHY	143

Appendix 1: Detailed fabrication process for Photosensitive Polyimide	153
Appendix 2: Rat Preparation for in vivo experiments	155

SUMMARY

Modulation of nerve signals using implantable bioelectronics has recently been recognized as a potentially powerful way to modulate bodily conditions or control neuroprostheses. Depending on the application, the ability to record and discriminate nerve signals and/or the ability to stimulate or block nerve signals may be required. However, creating a bioelectronic implant with a general purpose neural interface that is easy to implant, and can closely attach to small peripheral nerves without causing damage remains a grand challenge. The ability of one electrode design to reliably and selectively record and stimulate nerves across a range of dimensions has not been reported yet, although such a neural interface will greatly pave the way for enabling neuromodulation.

In this thesis, various designs of epineural interfaces fabricated by soft materials were investigated for recording and stimulation of peripheral and visceral nerves. Firstly, a flexible epineural strip electrode (FLESE) was demonstrated for recording from small nerves in rats. Small strip-shaped FLESEs enabled to easily and closely stick on various sized nerves for less damage in a nerve and optimal recording quality. Bipolar and differential bipolar configurations for the recording were investigated to optimize the recording configuration of the FLESEs.

Secondly, a split-ring electrode was investigated for selective stimulation of sciatic nerves, which was confirmed by different corresponding muscle activation patterns. In addition, neural recordings were demonstrated on the rat sciatic nerve using a transverse differential bipolar configuration of the split-ring electrode. A commercial cuff electrode was also implanted on the sciatic

nerve to confirm the recording setup, and to act as a benchmark for the flexible split-ring electrode.

Thirdly, a flexible and adjustable sling neural interface was explored for selective recording and stimulation with good electrical contact but minimal pressure on rat sciatic nerves. It showed the high quality of recordings using a mixed tripole configuration. This design also provided longitudinal tripolar and transverse configurations for selective stimulation on a nerve so that effective muscle activations were demonstrated. Furthermore, the results of blood flow measurements demonstrated that the pressure applied on the nerve by the neural interface was less than that applied by commercial cuff electrodes.

Battery-free neural interface as an advanced version was demonstrated by combining Triboelectric nanogenerators (TENGs) and the sling neural interface. The TENGs were optimized and demonstrated as a potential power source. Towards next step of battery-free platforms, direct stimulation using the TENGs combined with the sling interface was demonstrated on sciatic nerves and sciatic nerve branches, i.e., a common peroneal (CP) nerve in rats to activate tibialis anterior (TA) muscle.

Finally, a novel flexible neural clip (FNC) interface was investigated as not only a general purpose design of peripheral and visceral neural interfaces, but a wireless bioelectronic implant for bioelectronic medicines. Small peripheral nerves (sciatic nerve branches, vagus nerves, and pelvic nerves) in rats were stimulated using the FNC to validate the feasibility of the design. Finally, we demonstrated mid-field wireless pelvic nerve stimulation using the active FNC to evaluate possibility of the advanced FNC for bioelectronic medicine applications.

LIST OF TABLES

Table 1	Various neural interfaces with feature, subject, and target nerves.....	32
Table 2	The recorded compound neural action potentials (CNAPs).	66

LIST OF FIGURES

Figure 1.1	Schematic diagram of the comparison of the developed neural interfaces.	20
Figure 2.1	Schematic representation of nerve organization [54]	24
Figure 2.2	Various types of peripheral neural interfaces	24
Figure 2.3	(a) Polymeric micro channel electrode array for peripheral nerve interfacing [55]. (b) Schematic of in vitro and in vivo designs using a scaffold based regenerative electrode [19]. (c) Polyimide 3D channel array with embedded micro-electrode and inserted in a silicone tube [17]	26
Figure 2.4	(a) Representative SEM of a USEA consisting of 10 rows of 10 electrodes each, and (b) schematic showing positioning of the array in the cat sciatic nerve and the location of nerve segments (c) Representative implantation site from the short-term group. Connective tissue build-up has occurred around the silicone and wires (arrows) (d) In the short-term group, the tissue beneath the array appears firm, clearly showing each electrode penetration profile [12]. (e) SEM image for an HD-USEA device that was implanted for eight weeks. The image on the bottom shows a close-up of one of the electrode tips with sparse organic material adhering to the surface of the device. Scale bars = 1 mm, (f) One rat had a partially implanted HD-USEA at the end of the study period and the waffle pattern after array explantation on these devices showed marked increases in fibrosis [13]	28
Figure 2.5	Bidirectional control of hand prosthesis and characterization of neural stimulation A) the current was delivered as a function of the prosthetic hand sensor readouts B) photograph of the surgical insertion of a TIME in the median nerve of the participant C) Depiction of the subject's ulnar nerve with the two implanted electrodes [1]	29
Figure 2.6	Implantation surgery A) median and ulnar nerves approached from the medial aspect of the upper arm B) view under the microscope of the kevlar ansa pulling the electrode inside the nerve C) cables passing through transit holes in the skin and arranged to form a loop outside the body [30]	30
Figure 2.7	Stability and selectivity of implanted cuff electrodes A) Implanted a four-contacts spiral cuff on the radial nerve of the forearm and an eight contact FINE on the median and ulnar nerves B) Sensation locations after threshold stimulation at week 3 post-op [1]	31
Figure 2.8	Schematic diagrams of the different implants carried out (Top) and photographs of the TIME, LIFE and cuff electrodes implanted in the rat sciatic nerve (bottom) [88]	36
Figure 3.1	(a) The schematic diagram of a flexible epineural strip electrode (FLESE) and (b) a picture of the fabricated FLESE	40
Figure 3.2	Pictures of the fabricated (a) FLESE#1 and (b) FLESE#2. Yellow circles indicate suturing holes for implantation on nerves. Schematic diagrams of configuration of implantations on a nerve, respectively, (c) FLESE#1 with a concentric bipolar electrode, and (d) FLESE#2 with a hook electrode	41
Figure 3.3	Fabrication process for the FLESE	42
Figure 3.4	Illustration of packaging for the flexible neural electrode (a) Insert the electrode with spacer and (b) flip to lock after loading [91]	44
Figure 3.5	Pictures of (a) the assembled and (a) packaged FLESE	44
Figure 3.6	Schematic of the setup for the CNT coating [91]	46

Figure 3.7	SEM images (a) before and (b) after CNT coating on electrodes. (c) The magnified SEM image after the CNT coating.	46
Figure 3.8	Results from EIS for (a) the plot of interfacial impedances for with and without CNT coating and (b) the plot of phase angle.	47
Figure 3.9	(a) Schematic diagrams of implanted FLESE#1 and (a) a picture of implanted FLESE#1 (c) Results of CNAP recordings of FLESE#1 on a main sciatic nerve elicited by the concentric bipolar electrode. (d) The recording after applying xylocaine for a nerve block.	51
Figure 3.10	(a) Schematic diagrams of implanted FLESE#2 and (b) a picture of implanted FLESE#2 on rat sciatic nerves. (c) Results of CNAP recordings of FLESE#2 on a main sciatic nerve elicited by the hook electrode.	52
Figure 4.1	Schematic diagram of the experimental setup. Schematic diagram of the implanted flexible split ring electrode on the sciatic nerve for (a) stimulation and (b) recording. (c) Schematic diagram of an intra-muscular loop-hook bipolar electrode implanted in either the tibialis anterior or gastrocnemius muscles. (d) Schematic diagram of subdermal electrical stimulation of the hind limb using a needle electrode. Picture of the implanted (e) flexible split ring electrode and (f) commercial cuff electrode (Microprobe Inc., Gaithersburg, MD, USA) on the sciatic nerve in rats.	56
Figure 4.2	Schematic diagram of implanting a flexible split ring electrode on a sciatic nerve. (Inset) Picture of the fabricated split ring electrode.	57
Figure 4.3	Fabrication process of a flexible split ring electrode.	58
Figure 4.4	(a) Experimental setup for electrochemical impedance spectroscopy (EIS) and cyclic voltammetry (CV) test. The results of EIS for impedance and phase angle for Au and Pt electrodes (n=12) are shown in (b) and (c), respectively. (d) The results of CV for the Pt split ring electrodes (n=6).	60
Figure 4.5	(a) This plot shows the evoked compound muscle action potential (CMAP) in the Gastrocnemius Medialis (GM) (blue) and Tibialis Anterior (TA) muscles (red) as a function of electrode pairs from a single monophasic 20 μ s pulse with stimulation currents of 100 (light color) and 200 μ A (dark color) (n = 3). The CMAP recordings from the GM and TA muscles are shown as a function of electrode pairs in (b) SE#1-#4, (c) SE#1-#2, and (d) SE#2-#3, respectively, using a single monophasic 20 μ s pulse with currents of 200 μ A.	63
Figure 4.6	The compound neural action potential (CNAP) recordings from (a) recording electrode #2 (RE#2), (b) recording electrode #1 (RE#1), and (c) recording electrode #3 (RE#3) from the sciatic nerve evoked by subdermal electrical stimulation in the hind limb. Schematic diagram of the transverse differential bipolar configuration with three sensing electrodes and one reference electrode on the sciatic nerve. Red color highlights the evoked fascicles inside the sciatic nerve.	66
Figure 4.7	Compound neural action potential (CNAP) recordings with a pseudo-tripolar configuration from a sciatic nerve using a commercial cuff electrode (Pt, 100 μ m, inside diameter: 1.0 mm, rings spacing: 3 mm apart).	68
Figure 5.1	Schematic diagrams of experimental setup for recording and stimulation on a sciatic nerve. (a) Schematic diagram of an implanting flexible sling electrode on sciatic nerve for recording (b) Schematic diagram of an implanted hook electrode on common peroneal nerve for evoking neural signal. (c) Schematic diagram of an implanted flexible sling electrode for stimulation (d) Schematic diagram of an implanted loop-hook electrode on muscle for muscle signal recording.	71

Figure 5.2 (a) Picture of fabricated sling electrode (b) SEM image of Pt-black coated electrode. (c) Picture of implanted flexible sling electrode on a rat sciatic nerve.....	72
Figure 5.3 (a) Experimental setup for electrochemical impedance spectroscopy (EIS) and cyclic voltammetry (CV) test. The results of EIS of Au and Pt-black for (b) impedance and (c) phase angle. (d) CV plot of Pt-black coated flexible and adjustable sling electrode.....	75
Figure 5.4 Results of selective recording on the rat sciatic nerve. (a) CNAPs recordings of six sensing electrodes on the main sciatic nerve elicited from electrical stimulation of the common peroneal nerve. (b) Schematic diagram of how the electrodes were positioned on the sciatic nerve and a mixed tripole configuration for the recording (inset). (c) The latency of the peaks with standard error under a stimulation current of 1.2 mA as a function of recording electrode contacts. (d) The mean recorded amplitude with standard error of CNAPs under a stimulation current of 1.2 mA as a function of the six sensing electrode contacts.	77
Figure 5.5 The results of selective stimulation on the rat sciatic nerve. Schematic diagram of selective stimulation using the longitudinal tripolar configuration (left, inset) on the sciatic nerve through (a) Channel #1, (b) Channel #3, and (c) Channel #5. The results of normalized CMAPs from the TA and GM with selectivity (right).	79
Figure 5.6 The results of selective stimulation on rat sciatic nerves depending on different configuration. (a) Schematic diagram of the longitudinal tripolar configuration, (b) CMAP, and (c) normalized CMAP with corresponding to selectivity depending on stimulation current. (d) Schematic diagram of the transverse configuration, (e) CMAP, and (f) normalized CMAP with corresponding to selectivity depending on stimulation current.	80
Figure 5.7 Picture of sciatic nerves before and after implantation of a commercial cuff and the sling electrode, respectively (Left). The results of functional photoacoustic measurements (Right). (a) US image of the targeted blood vessel and (b) in vivo IR(570) PA B-scan image reflected the blood volume changes before implantation. (c) US image and (d) in vivo IR(570) PA B-scan image of the same position after the implantation of the cuff electrode. (e) US image and (f) in vivo IR(570) PA B-scan image before implantation (g) US image and (h) in vivo IR(570) PA B-scan image after the implantation of the sling electrode.....	82
Figure 6.1 Schematic diagram of the conceptual system using flexible neural interfaces and triboelectric nanogenerators (TENGs). (a) Schematic diagram of the conceptual system using the sling interface and a TENG in human. (b) Schematic diagram of the TENG in a compressed state and a released state. (c) The generated current by the TENG. (d) Schematic diagram of the flexible and adjustable sling interface and (e) leg contraction with compound muscle action potential (CMAP) recordings of tibialis anterior (TA) and gastrocnemius medialis (GM) muscles.	87
Figure 6.2 Fabrication procedure for triboelectric nanogenerator and flexible sling electrode (a) a PET substrate folded into zig-zag shape. (b) The folded PET substrate with copper electrodes attached. (c) The micro-patterned PDMS layers assembled on alternate copper electrodes for a pair of triboelectric layers. (d) The first layer of 6 μm polyimide on Al deposited silicon wafer. (e) The patterned first layer of polyimide. (f) The patterned metal layers of Ti (20 nm)/Au (300 nm). (g) The patterned second layer of polyimide. (h) The device is released from the substrate by electrochemical process.	89

Figure 6.3	Schematic diagram of working mechanism of triboelectric nanogenerator (a) Device layers in the original position, (b) as the device is compressed using force, triboelectric layers come in contact, (c) triboelectric layers moving apart from each other as the force is released, (d) electrostatic equilibrium is reached at the extreme position resulting into no current between electrodes, (e) triboelectric layers approaching each other as external periodic force is applied on multiple stacked device. (f) A picture of the 5-layer device.	90
Figure 6.4	Effect of electrical connections on stacked device with 5 layers. (a) Output voltage, (b) short circuit current, and (c) voltage and power characteristics for layers connected in parallel configuration; (d) Output voltage (e) short circuit current and (f) voltage and power characteristics for layers connected in series configuration.	93
Figure 6.5	(a) Peak output voltage (measured with a100 M Ω probe) for different device layers at 4 Hz; (b) Peak short circuit current for different device layers at 4 Hz; (c) Peak output voltage (measured with a100 M Ω probe) for different frequencies for 5 layered device; (d) Peak short circuit current for different frequencies for 5 layered device; (e) Variation of peak voltage and short circuit current with different confinement lengths for 5 layered device; (f) Output voltage and power with different load resistance for 5 layered device with 4 cm confinement length at 2 Hz ;(g) Variation of peak voltage and short circuit current with different confinement lengths for 15 layered device; (h) Output voltage and power with different load resistance for 15 layered device with 4 cm confinement length at 2 Hz.	95
Figure 6.6	Electrical connections of device layers in series and parallel configuration.....	98
Figure 6.7	Broadening of the voltage time domain output due to multiple peaks from stacked design. Output voltage signal for (a) 1 layer (b) 2 layers (c) 3 layers (d) 4 layers (e) 5 layers. (f) Output voltage time pulse width increases as the number of the layer increase.....	99
Figure 6.8	Charge generated by stacked TENGs as a result of the number of layers when to fully tap it by a hand.....	99
Figure 6.9	Demonstration of the energy harvester when assembled on human body. The results of (a) output voltage and (b) short circuit current generated by using clapping of hands. The results of (c) output voltage signal and (d) short circuit current generated by heel strike.	101
Figure 6.10	Picture of in vivo direct stimulation test using the sling interface and the TENG as direct stimulation source. (b) The recorded compound muscle action potentials (CMAPs) of GM (Red) and TA (blue) muscles by the battery-free sling interface. (c) Picture of in vivo direct TENG stimulation test using a pair of Pt/Ir wires on common peroneal (CP) nerve (inset). (d) Current peaks generated by the TENG and (e) the CMAPs recordings at 2 Hz. (f) Current peaks generated by the TENG and (g) the CMAPs recordings at 4 Hz.	103
Figure 7.1	Schematic diagram of different applications of a wireless flexible neural clip (FNC) interface for wireless modulation of nerves to achieve different organ or tissue output. (i) Vagus nerve stimulation (VNS), (ii) bladder nerve stimulation, and (iii) the stimulation of sciatic nerve branches for modulation of (iv) heart rate (HR), (v) bladder dysfunction, and (vi) leg muscles, respectively.....	107
Figure 7.2	Photomicrographs of small peripheral nerves in rats; (i) a vagus nerve, (ii) a pelvic nerve, and (iii) sciatic nerve branches.	108

Figure 7.3	(a) Schematic diagram of implanting a flexible neural clip (FNC) interface in a peripheral nerve. (b) Picture of fabricated FNC and configuration. ...	110
Figure 7.4	(a) Schematic diagram of opening clip head for implantation of a nerve. (b) Schematic diagram of cross-section view after the implantation.	110
Figure 7.5	The results of electrochemical characterization of iridium oxide coated electrodes for a) impedance, phase angle, and b) cyclic voltammetry.	114
Figure 7.6	Photomicrograph of a) fabricated active FNC and b) micro-PCB soldered with active components. c) After aligning the FNC on the PCB then, d) conductive epoxy was applied and cured. e) The UV LED and coil were soldered and encapsulated with Kwiksil.	116
Figure 7.7	Sciatic branch nerve stimulation to control muscles. (a) Schematic diagram and photomicrographs of sciatic nerve branches. (b) Threshold currents versus pulse widths when stimulating the common peroneal (CP) and tibial nerves.	119
Figure 7.8	(a) The recorded EMG signals and stimulation pulses of the CP and tibial nerve stimulation. (b) The recorded EMG signals and stimulation pulses of the CP nerve stimulation before lidocaine application (left panel) and after lidocaine application (right panel).	120
Figure 7.9	a) Schematic diagram of vagus nerve stimulation (VNS) for the control of heart rate (HR). b) A photomicrograph of an implanted flexible neural clip (FNC) on a vagus nerve in a rat. c) Schematic diagram of biphasic pulses for the stimulation.	122
Figure 7.10	a) Electrocardiogram (ECG) recordings before and after VNS. b) The change in HR caused by VNS (2-way ANOVA, $p < 0.05$). Circles indicate the mean value and bars represent the standard error of the mean.	123
Figure 7.11	Continuous recording of intra-bladder pressure with increasing amount of charge injected via the clip electrode. Duration of stimulation is indicated by blue stimulation markers below the pressure curve. Inset shows the pressure changes associated with the stimulation trial using the highest amplitude (1000 μ A). High frequency oscillations associated (HFO) with voiding response was observed. (b) Peak increase in intra-bladder pressure is linearly correlated with amount of stimulation amplitude used.	125
Figure 7.12	Supra-threshold stimulation of pelvic nerve produced repeatable increases in intra-bladder pressure. (a) Continuous recording of intra-bladder pressure (mmHg) during 8 trials of pelvic nerve stimulation at frequency of 10 Hz and amplitude of 650 μ A. Voiding responses were observed in all 8 trials. (b) Average change in intra-bladder pressure curve from 8 trials of stimulation is indicated by the black curve while the blue shaded region indicates standard deviation. The same clip electrode produced similar responses in different rats for acute pelvic nerve stimulation experiments. Increasing stimulation amplitudes correlated with increasing peak intra-bladder pressure changes (c) and faster time to reach peak pressure during stimulation (d) in 2 consecutive experiments using the same electrode (N =2 rats).	127
Figure 7.13	Schematic diagram of pelvic nerve stimulation for the modulation of bladder function. Evoked intra-bladder pressure changes and micturition outcome with increasing stimulation amplitudes for (b) short (400 μ m) and (c) long inter-lead distances (1600 μ m). Photomicrographs of implanted flexible neural clip (FNC) electrodes on the same nerve in two different configurations are shown in (b) and (c). Increases in bladder pressure due to pelvic nerve stimulation was observed for both implantation configurations at increasing stimulation current from (i) 25 μ A, (ii) 50	

<p>μA, (iii) $100 \mu\text{A}$, and (iv) $200 \mu\text{A}$, respectively ($n = 3$ trials). Inverted triangles denote the onset of voiding events.....</p>	128
<p>Figure 7.14 (a) Urine output as a result of different stimulation amplitudes. (b) Post stimulation pressure drops as a result of different stimulation amplitudes. (c) Time to reach peak pressure as a result of different stimulation amplitudes. At supra-threshold amplitudes, the post-stimulation pressure drop, and time to reach a peak in bladder pressure were similar and not significantly different between the two implantation configurations (2-way ANOVA, $p > 0.05$, $n = 3$ trials each).....</p>	129
<p>Figure 7.15 (a) Schematic diagram of the assembly of the active FNC. Firstly, active version of FNC was fabricated where contact pads matched with the size of mini-PCB. Secondly, wireless components including diodes and capacitors were soldered first on the PCB. Thirdly, the FNC was aligned on the PCB, then, silver paste was applied for electrical connections. Finally, a coil and UV LED were soldered and the entire FNC was encapsulated in a silicone elastomer except the active electrodes of the FNC. (b) A photomicrograph of the implanted active FNC on a pelvic nerve in a rat.</p>	131
<p>Figure 7.16 (a) A photomicrograph of implanted active flexible neural clip (FNC) interface. (b) A magnified photomicrograph of implanted FNC on a pelvic nerve. .</p>	131
<p>Figure 7.17 Results of the pelvic nerve stimulation on bladder pressure changes, pressure drop, time to reach peak, and urine output as a result of phase width (i) $150 \mu\text{s}$, (ii) $300 \mu\text{s}$, and (iii) $500 \mu\text{s}$, respectively. Actual duration was (i) $5.21 \pm 0.21 \text{ s}$, (ii) $6.12 \pm 0.58 \text{ s}$, and (iii) $5.86 \pm 1.00 \text{ s}$, respectively and the mean was $5.73 \pm 0.71 \text{ s}$. Inverted triangles denote the onset of voiding events.....</p>	133
<p>Figure 7.18 (a) Micro CT image of the implanted FNC; (inset) magnified image of the FNC. (b) Cross section view of the Micro CT image.</p>	134
<p>Figure 8.1 Schematic diagram of a self-sustainable platform for neuromodulation combining neural interfaces and triboelectric nanogenerators (TENGs).....</p>	142
<p>Figure 8.2 Schematic diagram of multiple implantation and applications of the neural interfaces.....</p>	142

LIST OF SYMBOLS

MEMS	Microelectromechanical systems
Al	Aluminium
Ti	Titanium
Au	Gold
Pt	Platinum
FPC	Flexible Printed Circuit
CNTs	Carbon Nanotubes
SEM	Scanning Electron Microscopy
EIS	Electrochemical Impedance Spectroscopy
PBS	Phosphate buffered saline
NCV	Nerve Conduction Velocity
CNAP	Compound Neural Action Potential
CMAP	Compound Muscle Action Potential
CDC	Charge Delivery Capacity
CV	Cyclic Voltammetry
CSC	Charge Storage Capacity
CIC	Charge Injection Capacity
GM	Gastrocnemius Medialis
TA	Tibialis Anterior
ENG	Electroneurograms
EMG	Electromyography
FDA	The Food and Drug Administration
ESA	Electrochemical Surface Area
GSA	Geometric Surface Area

CHAPTER 1. INTRODUCTION

1.1. Background and Motivation

A growing field of neurotechnology research involves modulating neural impulses to control neuroprostheses or the human body. For instance, the control of bionic limbs can be improved through sensory feedback provided by stimulating the sensory nerves [1-3]. Epidural electrical stimulation of specific dorsal roots of the lumbar spinal cord may help in the movement of a paralyzed leg [4]. Another emerging field of bioelectronic medicine includes therapeutic effects mediated by the control of internal organs through the modulation of electrical signalling patterns in visceral nerves [5-7]. However, due to many physiological and anatomical difficulties in accessing small nerves, the precise targeting and modulation of neural signals in the peripheral nervous system (PNS) has remained a grand challenge. Accordingly, the most critical challenge is to develop implantable bioelectronics with a neural interface that can be closely attached to target nerves for long-term use without causing damage, while reliably maintaining high-resolution recording and stimulation, targeting only the signals that elicit desired effects without altering non-target functions [5, 6].

Numerous neural interfaces for peripheral nerve applications have been previously proposed and developed, such as extra-neural (cuff and FINE) [1, 8-10], penetrating (USEA) [11-13], intra-fascicular (LIFE and TIME) [14-16], and regenerative electrodes [17-20]. The extra-neural[1] and the intra-fascicular (TIME)[2] interfaces were implanted on sensory nerves in the hands of human subjects to provide sensory feedback from prosthetic arms. However, the intra-

fascicular approach itself may be invasive leading to nerve damage as well as difficulty in implantation on very small nerves [21]. The use of extra-neural cuff electrodes typically carries a high risk of damaging the nerve if the inner walls are too close to the nerve. As a result, the Food and Drug Administration (FDA) recommends that the inner diameter be 1.8 times the diameter of the nerve [9]. As a result, the neural signals recorded by the electrode contacts along the inner walls of the cuff electrode tend to have fairly low signal-to-noise ratios (SNR) [9, 22-24]. Furthermore, as a result of the need to match the diameter of the nerves precisely, it is often necessary to prepare a number of cuffs of different sizes for each implantation. This is also limited in that the fabrication of cuff electrodes typically requires significant manual assembly of relatively bulky cuff and lead wires. This also makes high quality mass production challenging, and makes integration of the electrodes with active components for wireless transmission rather difficult. Helix electrodes have been used for vagus nerve stimulation (VNS) in humans as a new treatment modality for epilepsy and drug-resistant depression, although there are limitations in challenging surgical procedures of implantations of helical coil electrode, anchoring tether, and the lead due to the narrow surgical place [25, 26].

New extra-neural approaches with flexible materials fabricated using microfabrication technologies have recently shown promising results for peripheral nerve modulation [27-32], however, those are limited in surgical implantation on small visceral nerves due to its small size and the narrow space with movement in the viscera for bioelectronic medicine.

The microelectromechanical system (MEMS) based technology can provide integration with active components (such as amplifiers for neural recording and

stimulators for neural stimulation) as well as various cutting-edge technologies such as microfluidic, microcoil for magnetic stimulation [33] and ultrasonic backscatter for neural dust [34]. Furthermore, the integration of neural interface with wireless powering by either ultrasound[34] or electromagnetic powers[35-37] is a promising direction for future bioelectronic medicine.

1.2. Research Objectives

The main objective of this thesis is to demonstrate various designs of epineural interfaces for recording and stimulation of peripheral and visceral nerves. This project implementation is divided into more specific objectives to realize the main aim of the thesis.

First object is the development of novel neural interfaces via non-invasive approach to solve the current challenges which were described in the motivation. Second object is the development of advanced neural interfaces such as battery-free and wireless platforms. Third object is the development of neural interfaces for modulating small visceral nerves for bioelectronic medicine that is a promising and emerging field nowadays. For these objectives, various designs of epineural interfaces are demonstrated (Figure 1.1). The detailed sections are listed below:

- A. A flexible epineural strip electrode (FLESE) as a novel neural interface design for nerve recording in sciatic nerves
 - a. Carbon nanotube (CNT) coating
 - b. *In vivo* neural recording using bipolar configuration
 - c. *In vivo* neural recording using differential bipolar configuration
- B. Novel designs of neural interfaces for bidirectional selective nerve recording and stimulation in sciatic nerves
 - a. Selective recording and stimulation using a flexible split-ring electrode
 - b. Selective recording and stimulation using a flexible and adjustable sling interface

- C. Development of a battery-free neural interface combining with triboelectric nanogenerators (TENGs).
 - a. Design and in-vitro test of TENGs
 - b. Direct stimulation using the sling interface combining with the TENGs
- D. A novel design of neural clip (FNC) interface for bioelectronic medicine
 - a. Stimulation of Sciatic nerve branches
 - b. Stimulation of vagus nerves
 - c. Stimulation of pelvic nerves
 - d. Wireless pelvic nerve stimulation using active FNC

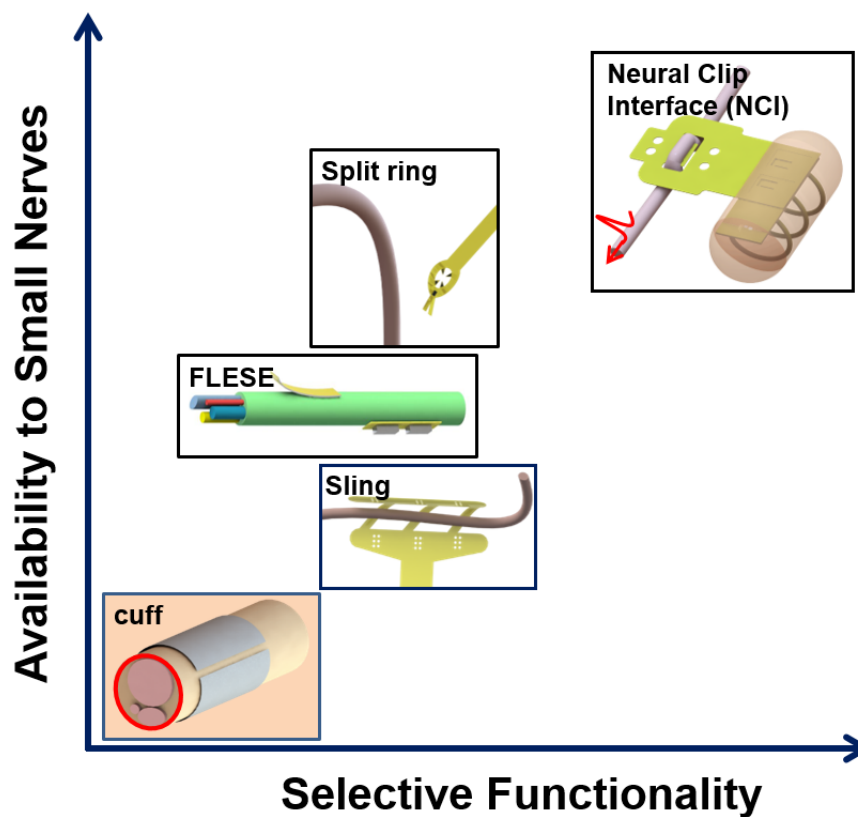


Figure 1.1 Schematic diagram of the comparison of the developed neural interfaces.

1.3. Organization of Thesis

Chapter 1 describes the background, motivations, and objectives of this thesis. Chapter 2 reviews the previous works relevant to this project and discusses neural interfaces and current applications. Chapter 3 presents flexible epineural strip electrode (FLESE) for recording of sciatic nerves in rats. Chapter 4 and Chapter 5 demonstrate selective recording and stimulation of sciatic nerves using flexible split-ring electrodes, and adjustable and flexible sling electrodes, respectively. Chapter 6 presents the development of a battery-free neural interface using the sling electrode and triboelectric nanogenerator (TENGs). Chapter 7 introduces a novel flexible neural clip (FNC) interface for the stimulation of various peripheral nerves such as sciatic nerve branches, vagus nerves, and pelvic nerves in rats. Finally, wireless stimulation of visceral pelvic nerves using active FNC is demonstrated for bioelectronic medicine applications. Chapter 8 presents conclusion and future work.

CHAPTER 2. OVERVIEW OF NEURAL INTERFACE

2.1. Neural interface

The emerging field of bioelectronics involves monitoring and modulating biological signals to control the bodily functions and to treat diseases. With the remarkable improvement of soft and stretchable devices that enables the integration of a variety of bio-sensors and wireless powering elements, e-skin and wearable technologies have shown promising prospects of advanced health care [38-44]. Recently, the target of interest is moving from the human skin to the internal organs of the body by combining these cutting-edge technologies with neuroscience [5, 6, 45]. Such implantable bioelectronics, which requires a biocompatible, miniature, soft, and wirelessly powered platform [46-49], may interface with not only the central nervous systems (CNS) for restoring or substituting neurological deficits or disabilities [50], but the peripheral nervous systems (PNS) to control neuroprostheses [1-3] or physiological functions [5-7]. For this, neural interfacing technology (NIT), which provides the basis for direct communication with neuron tissues and mapping neural signals, is an essential area to be preferentially developed among principal research areas [45]. In case of NIT in the CNS applications, glial scar-free neural recordings were achieved using ultraflexible probes in the brains of rodents [51, 52]. Furthermore, the brain-spine interface was able to support the locomotion of monkeys using a multimodal neural interface, called e-dura [4, 53].

Unlike picking up neural spikes from the brain or the spinal cord, reliably

acquiring neural signals directly from peripheral nerves has proven to be a much harder challenge. This is due to many physiological and anatomical differences of nerves [54] as follows (**Figure 2.1**):

- i) axons are surrounded by insulating myelin, then bundled into fascicles which are further surrounded by dense protective outer layers, known as the perineurium and epineurium
- ii) axons are bundled densely inside the nerve so that it is difficult to elucidate which specific pathways, or fascicles, signals are originating from
- iii) any neural signals that one may achieve to record are inherently smaller than brain or cortex
- iv) additional interfering sources such as muscles and movement artifacts, which corrupts signals

For peripheral nerve applications, finding a reliable way to record tiny neural signals that travel through peripheral nerves or for selective stimulation of these nerves has been required. Accordingly, various types of neural electrodes have been reported in the past. Flexible multi-electrode array (MEA) has enabled the implementation of penetrating interfaces with fascicular and sub-fascicular selectivity.

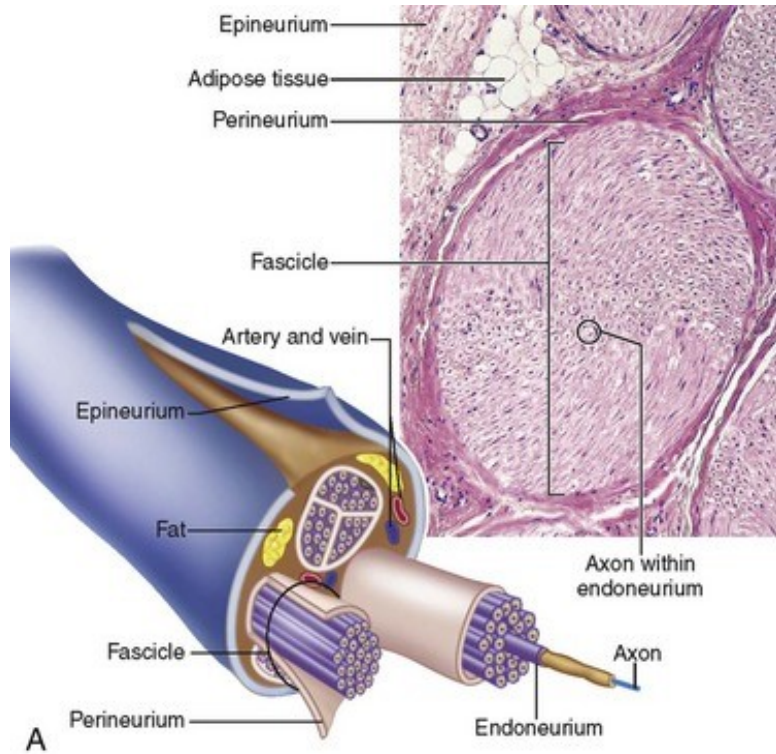


Figure 2.1 Schematic representation of nerve organization [54]

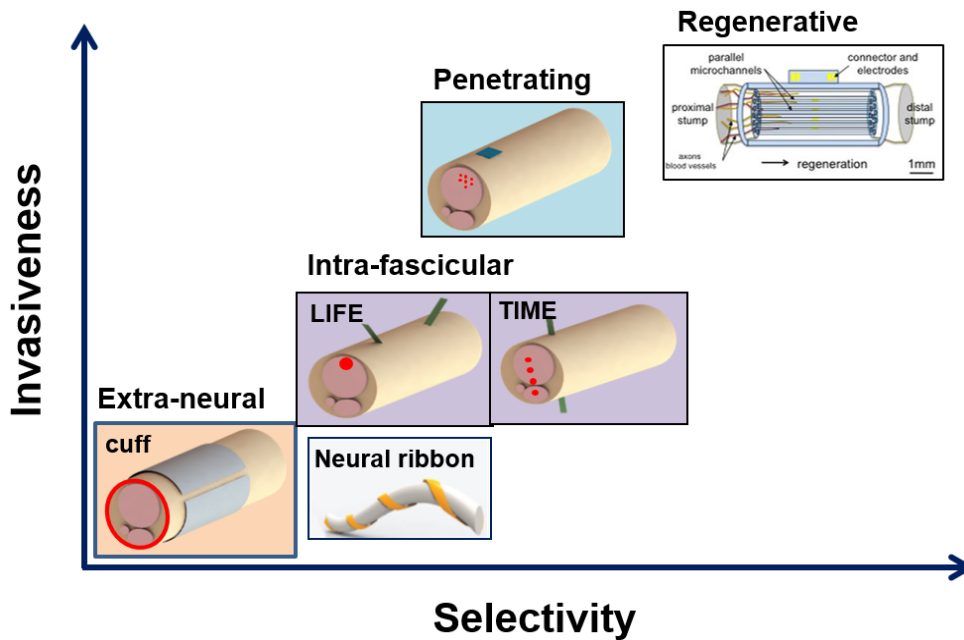


Figure 2.2 Various types of peripheral neural interfaces

Intra-fascicular interfaces are inserted transversally or longitudinally with respect to the long axis of nerves. Neural cuffs are tubular devices placed around the epineurium of a whole nerve and have electrodes on their inner surface. The conceptual drawings of these neural electrodes are shown in **Figure 2.2**, such as extra-neural (cuff and FINE) [1, 8-10], penetrating (USEA) [11-13], intra-fascicular (LIFE and TIME) [14-16], and regenerative electrodes [17-20]. These electrodes reveal the tradeoffs between high selectivity and low invasiveness. In this chapter, features and applications of several types of neural interfaces are briefly described.

2.1.1. Regenerative Interface

The regenerative electrodes have an array of holes or nerve guidance channels with electrodes to interface a high number of nerve fibers, which is implanted between the severed stumps of a peripheral nerve (**Figure 2.3a,b**) [18-20, 55]. Ideally, regenerating axons grow through the holes or the nerve guidance channels enabling the recording of action potentials and stimulation of individual axons or small fascicles. It ultimately allows for high channel and bidirectional communication between an amputated nerve and a prosthetic limb. The success of functional recovery, however, depends on the regenerating fibers accurately finding and reconnecting to its original target. Also, challenges include slow regeneration (1-3 mm per day) and progressive reduction in the capacity of schwann cells to support regrowth (**Figure 2.3c**) [17, 18]. To overcome these challenges artificial bridging structures with hollow tubes matching the nerve diameter made of collagen, biodegradable

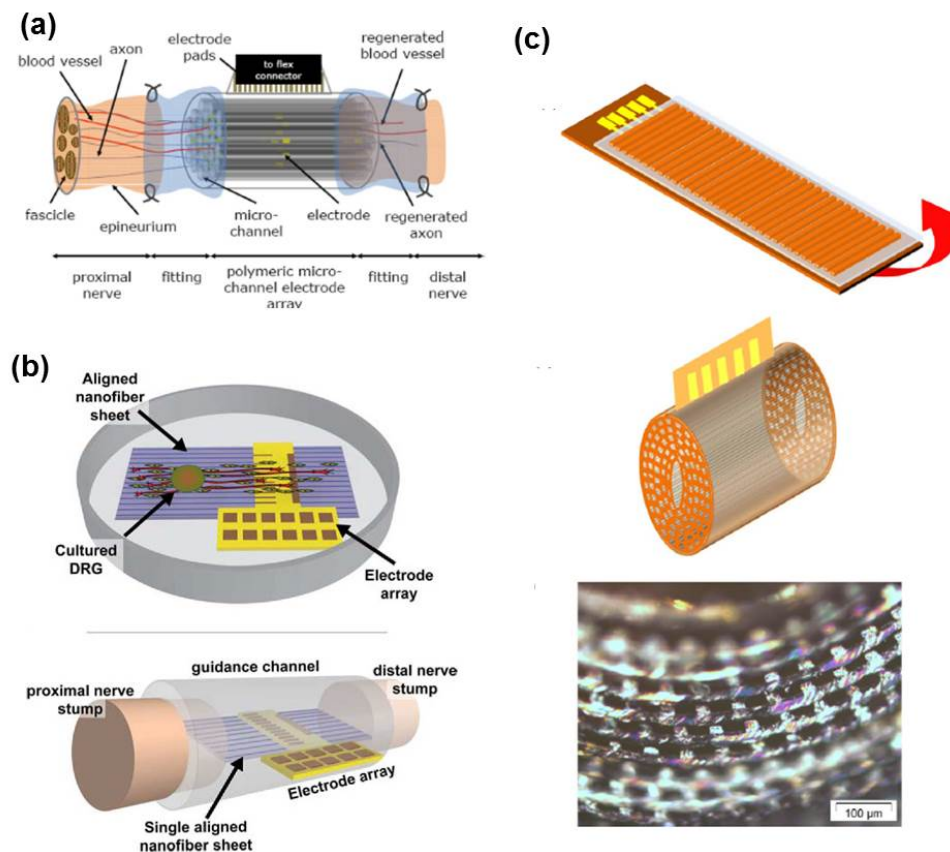


Figure 2.3 (a) Polymeric micro channel electrode array for peripheral nerve interfacing [55]. (b) Schematic of in vitro and in vivo designs using a scaffold based regenerative electrode [19]. (c) Polyimide 3D channel array with embedded micro-electrode and inserted in a silicone tube [17].

polymers, or polymeric materials have been demonstrated [17, 18, 55, 56].

To improve regeneration, research is not only focusing on increasing the speed of axonal growth preventing neuronal apoptosis and muscle atrophy, but maintaining a supportive environment in the distal nerve. Recently, to increase the speed of axonal growth, applying electrical stimulation [57], pulsed electromagnetic fields [58], and low power laser therapy [59] have been conducted in rodent models. However, due to the limitation of nerve injury of rodent models, it does not adequately recapitulate the situation in humans. Alternatively, large animals such as sheep and nonhuman primates that have the similar distance to those in human could be used as models for

peripheral nerve regeneration [20]. Since the human axons have a great distance to reach the target tissue, injury leaves the distal nerve stump denervated for a prolonged period. It leads to chronic denervation of the distal nerve stump resulting in neuronal apoptosis, breakdown of schwann cell tubes, and muscle atrophy. This reduces the expression of neurotrophic growth factors [20].

2.1.2. Penetrating Interface

Multi-electrode arrays were primarily designed for the CNS interface, however, some multi-electrode arrays have also been inserted for peripheral nerves as a penetrating interface. To minimize the number of redundant electrodes and to enhance the selectivity of fascicles within the nerve, Utah Slanted Electrode Array (USEA) has been demonstrated for neuromodulation of large structures (>4 mm) in the PNS (**Figure 2.4a,d**) [12, 60]. Also, high-Density USEA (HD-USEA) have been developed for recording and stimulation of sub-millimeter neuroanatomical structures [11]. Behavioral and cellular consequences of un-wired HD-USEA implanted in rat sciatic nerve have been conducted for one and two month periods (**Figure 2.4e,f**) [13]. However, some critical issues should be seriously considered for the USEAs. Firstly, USEAs typically have stiff electrode arrays which are enough to be penetrated in nerves. This leads to the damage of the nerve or fascicles during the implantation and movements of the object due to mechanical mismatch between the nervous tissues and the electrodes. This mechanical coupling affects both electrode-to-tissue and tissue-to-electrode [50].

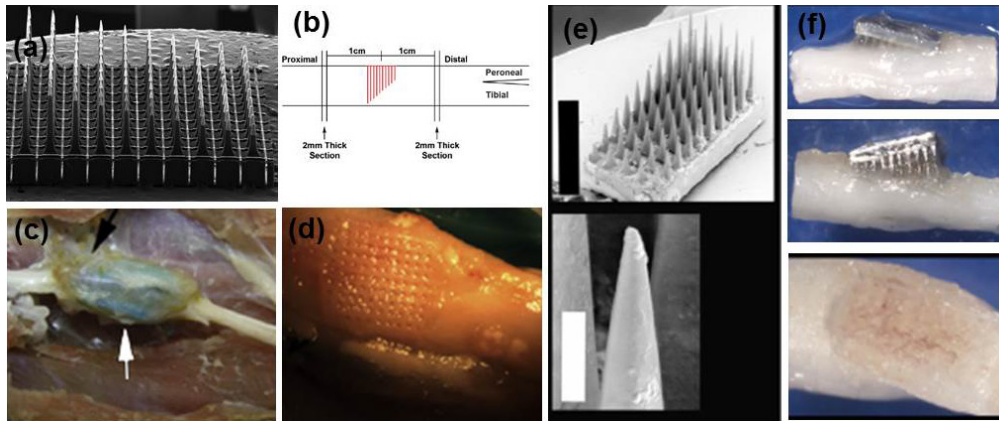


Figure 2.4 (a) Representative SEM of a USEA consisting of 10 rows of 10 electrodes each, and (b) schematic showing positioning of the array in the cat sciatic nerve and the location of nerve segments (c) Representative implantation site from the short-term group. Connective tissue build-up has occurred around the silicone and wires (arrows) (d) In the short-term group, the tissue beneath the array appears firm, clearly showing each electrode penetration profile [12]. (e) SEM image for an HD-USEA device that was implanted for eight weeks. The image on the bottom shows a close-up of one of the electrode tips with sparse organic material adhering to the surface of the device. Scale bars = 1 mm, (f) One rat had a partially implanted HD-USEA at the end of the study period and the waffle pattern after array explantation on these devices showed marked increases in fibrosis [13].

Secondly, it requires additional layer or elements to make the electrode stick on the nerve for long-term use such as silicone [12] or nerve wrap [13]. Thirdly, the large number of electrodes requires many wires and connectors, which demands additional and complicated mapping procedures.

2.1.3. *Intra-fascicular interface*

A new electrode concept of intra-fascicular interface has been proposed using flexible polyimide materials. For instance, transverse intra-fascicular multichannel electrode (TIME) has been proposed. The narrow body of flexible electrode was implanted transversely in a peripheral nerve and addressed several subgroups of nerve fibers with a single device [15, 16].

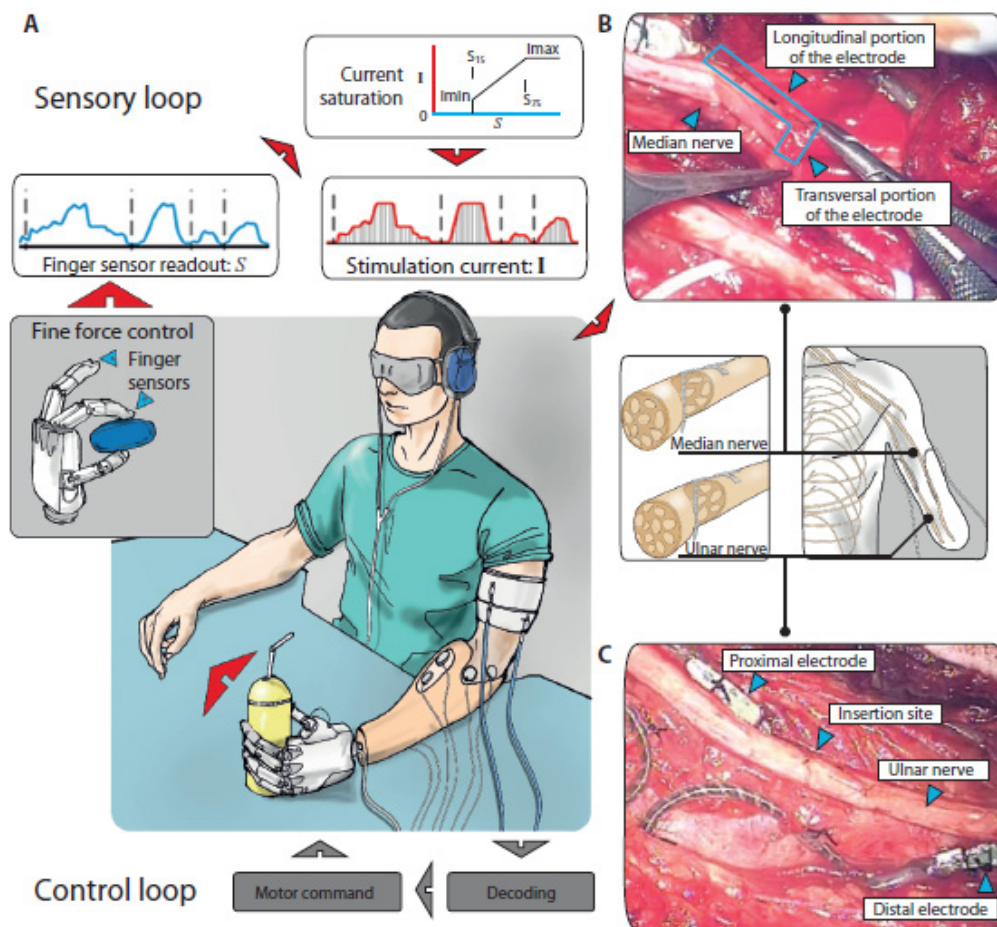


Figure 2.5 Bidirectional control of hand prosthesis and characterization of neural stimulation A) the current was delivered as a function of the prosthetic hand sensor readouts B) photograph of the surgical insertion of a TIME in the median nerve of the participant C) Depiction of the subject's ulnar nerve with the two implanted electrodes [1].

The TIME was implanted on sensory nerves in the hands of human subject to provide touch sensation from artificial hand prosthesis (**Figure 2.5**) [2].

Furthermore, longitudinal intra-fascicular electrode (LIFE) has been developed to improve selectivity, stimulus intensity, and SNR [14, 61]. The LIFE was implanted in the human median and ulnar nerves for 4 weeks showing

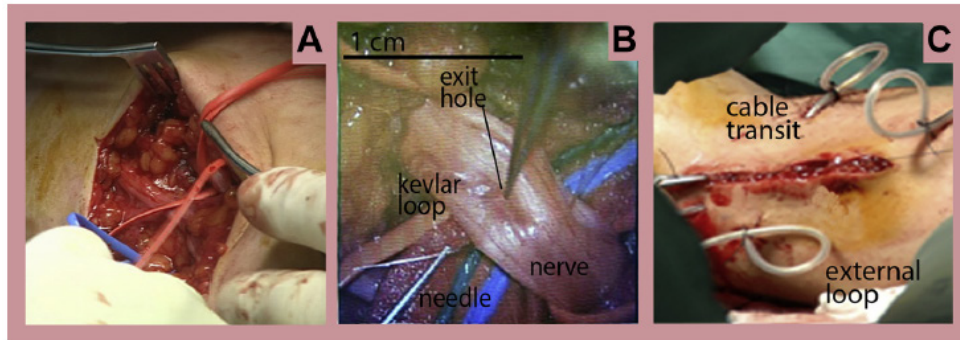


Figure 2.6 Implantation surgery A) median and ulnar nerves approached from the medial aspect of the upper arm B) view under the microscope of the kevlar ansa pulling the electrode inside the nerve C) cables passing through transit holes in the skin and arranged to form a loop outside the body [30].

the efficacy of sensory stimulation decayed after 10 days [62]. In addition, there were limitations in the absence of stabilizing structures, cables through the skin, the implant angle, and the unproven magnetic resonance imaging compatibility (Figure 2.6)[21].

Even though LIFE and TIME shows a higher level of selectivity by implantation inside nerves, the intra-fascicular approach itself can potentially cause nerve damage [21]. On the other hand, extraneural electrodes such as a spiral cuff and FINE show effective selectivity that is similar to acute trials with intra-fascicular electrodes [1]. For this reason, the non-invasive neural interfaces are preferred when used for clinical purposes [6, 63, 64]. Therefore, developing advanced epineural interfacing is still crucial for the clinical applications of neural prostheses.

2.1.4. *Extra-neural Interface*

Extra-neural electrodes have been most broadly used for clinical applications thanks to their non-invasive approach and easy implantation.

Cuff electrodes have been widely used chronically in different clinical applications owing to their easy implantation and low invasiveness [22, 23]. To overcome the limitations such as low signal-to-noise ratio (SNR) and requiring high stimulus charges due to loose-fitting, snug-fitting nerve cuffs have been investigated and approved to reduce the stimulus charge injection for stimulation as well as to obtain a high SNR for neural recording [8]. In addition, in order to increase the selectivity of cuff, innovative designs (flat interface nerve electrode, FINE) have been developed. The FINE promotes the reshaping of the nerve to adapt to the flat geometry of the interface, thus reducing the distance of the fascicles to the stimulation point [10]. The cuff and FINE were studied in recording of human median and ulnar nerves (**Figure 2.7**) [1] as well as stimulation of human tibial and common peroneal nerve to activate important muscles for neuroprosthesis [65].

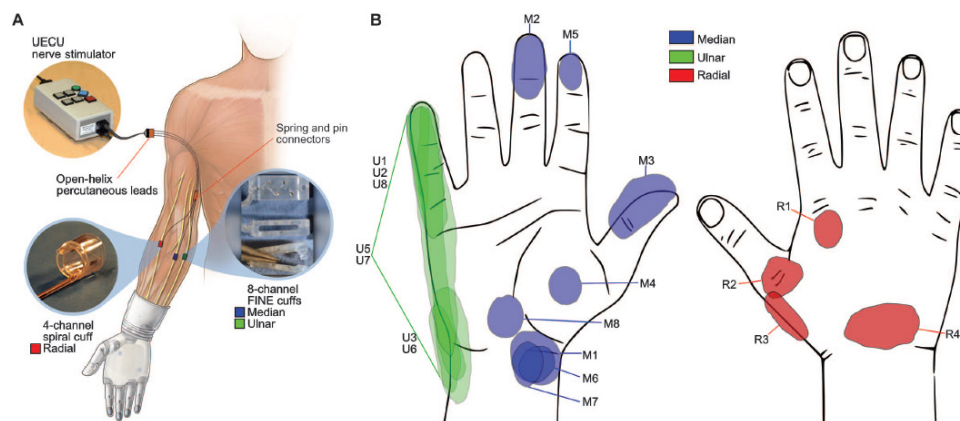


Figure 2.7 Stability and selectivity of implanted cuff electrodes A) Implanted a four-contacts spiral cuff on the radial nerve of the forearm and an eight contact FINE on the median and ulnar nerves B) Sensation locations after threshold stimulation at week 3 post-op [1].

Table 1 Various neural interfaces with feature, subject, and target nerves.

Implantation Approach	Electrode Type	Subject	Target Nerve	Ref.
Invasive	Utah Slant Electrode Array (USEA)	Cat	Sciatic nerve, Pudendal nerve	[11, 12, 66, 67]
		Rat	Sciatic nerve	[11, 13]
	Transverse intra-fascicular multichannel electrode (TIME)	Rat	Sciatic nerve	[15, 16]
		Human	Median and Ulnar nerves	[2]
	Longitudinal intra-fascicular electrode (LIFE)	Rat, Cat	Sciatic nerve	[14, 61]
Human		Median and Ulnar nerves	[21, 68]	
Non-invasive	CUFF	Rabbit, Rat, Cat	Sciatic nerve	[22, 23, 69, 70]
		Rat, Sheep	Vagus nerve	[71-74]
		Human	Radial nerve	[1]
	Flat interface nerve electrode (FINE)	Cat, Dog	Sciatic nerve	[10, 75]
		Human	Median and Ulnar nerves, Tibial and Common Peroneal nerves	[1, 65]
	New cuff	Rat	Sciatic nerve	[28, 76, 77]
	Helical Electrode	Human	Vagus nerve	[78]

Table 1 shows a variety of neural interfaces for peripheral nerves depending on electrode type, subject, and target nerves. Non-invasive approaches have been used for vagus nerve application and the helical electrode has been used for clinical vagus application.

2.2. Materials

The choice of material is critically important for neural interface design since lots of requirements should be considered. Here are basic considerations for designing neural implants [64, 79].

The first is surface biocompatibility. All implant designs have a minimal impact on the body including any immune responses, and inflammatory

response resulted from any surgical intervention. It should be prevented by proper material selection as well as by cleanness before the implantation. For the selection of biocompatible materials, basic material investigations can be identified in *in vitro cytotoxicity test* with standardized cell cultures. In addition, the international standard ISO 10993 “Biological evaluation of biomedical devices” describes test systems, procedures and evaluation schemes to classify an implant as a biocompatible or not [79].

The second is structural biocompatibility, which refers to mechanical interaction between implants and the surrounding tissue including weight, shape and flexibility (Young’s modulus). The mismatch of mechanical properties between the implanted material and target tissues causes cellular reaction that attack and encapsulate the implant [50]. For PNS applications, collateral damage by movement of the implant should be prevented. According to ISO 10993, a certain material, shape and texture have to be conducted in chronic *in vivo* experiments in animals before any device is allowed to enter a clinical trial [79].

The third is *biostability*, which summarizes different chemical aspects with respect to material stability and system integrity [79]. For chronic implantation, implants stay within the human body for decade, though the battery powered electronics have to be exchanged every 5 to 10 years [64, 79]. During the period, the substrate and insulation layers should not delaminate or degrade, and metals should not be corroded. Through *in vitro* soaking tests described well in the ISO 10993, a first approximation of the biostability of the materials is often performed at higher temperature to accelerate the diffusion processes, for instance, in physiological saline, Ringer’s solution or cell culture media, and

thereby their impact on aging and the mean time to failure.

Polymer materials have been well known as optimal materials for neural interfacing in terms of implantation, long-term stability in a hostile environment, low material stiffness (i.e. high material flexibility), and good electrical insulation of metallic conductors [64]. Several polymer materials have been used for implantable biomedical devices and neural interfaces. Here is the brief introduction of popular materials which are widely used in neural implants.

2.2.1. PDMS (Polydimethylsiloxane)

PDMS is one of biocompatible materials widely used for biomedical applications among the synthetic polymers. It provides not only excellent resistance to biodegradation and ageing, but also high biocompatibility. It is extremely stable and flexible, and has approval according to USP class VI for unrestricted use in chronic implants [79, 80]. Other significant property is the high permeability to gases and vapors which is about 10-fold compared to natural rubber [79]. However, when it is used for in vivo, some issues should be considered such as the adhesion of silicone to bulk material and void free deposition and curing of the silicone rubber, since these will significantly contribute to osmotic reactions occurring when silicone is immersed into ionized water (e.g. the body environment) [79, 81]. Peripheral nerves are quite sensitive to humidity so that PDMS could damage nerves due to the osmotic reaction or high water absorption property for chronic implantation.

2.2.2. Parylene

Parylene is the common name for polyparaxylylene (PPX), a group of linear,

noncross-linked and semicrystalline polymers, which belong to the thermoplasts [79]. Parylene layers are deposited in a vapor deposition polymerization process, using the dimer of the adequate parylene type as starting substance so that it allows a conformal coating of the target [82]. In particular, parylene C [poly(dichloro-p-xylylene)] is the most popular parylene type for the use in biomedical applications, due to the well suited combination of electrical and barrier properties [64]. Its good biocompatibility (FDA approved, USP class VI), chemical and biological inertness, good barrier properties, slippery surface and its functionality as an electrical insulator predestines parylene C for the use as substrate or encapsulation material for implanted neural prostheses [64, 82]. However, due to the properties of fragile and hard handling in thin sheets of parylene C compared with those of polyimide in comparable thickness, it is used together with PDMS to overcome those limitations.

2.2.3. Polyimide

Polyimide is one of the most promising materials for neural interfaces owing to its flexibility, biocompatibility, high stability, low water uptake and long durability [79]. For several decades, polyimide as a subtraction and insulation material has been successfully used for neural implants [79, 83, 84]. There are traditional non-photosensitive polyimides that use a photoresist mask as an etching template in one of the standard steps. Compared to non-photosensitive polyimide, photosensitive polyimides (PSPIs) have also been investigated [84-87]. Since PSPIs can be patterned directly by UV light with developer chemicals

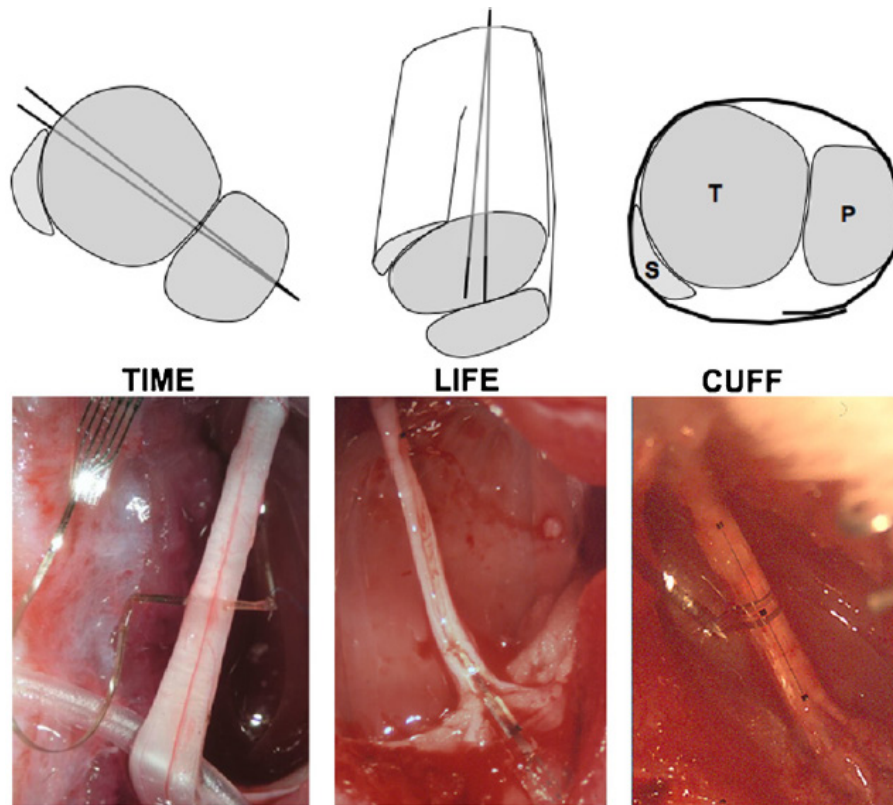


Figure 2.8 Schematic diagrams of the different implants carried out (Top) and photographs of the TIME, LIFE and cuff electrodes implanted in the rat sciatic nerve (bottom) [88].

so that it provides a highly reliable microelectrode array with fewer manufacturing steps [86].

Polyimide has huge advantage in that it enables high resolution patterning for complicated neural designs such as cuff, TIME and LIFE [88]. It is also compatible with semiconductor fabrication process. Hence, it is amenable to be integrated with IC for wireless platform.

2.3. Recent trend of neural interface

Recently, new extraneural approaches with flexible materials fabricated using microfabrication technologies have shown promising results for nerve recording and stimulation [76, 77]. This microelectromechanical system

(MEMS) based technology can also provide integration with active components (such as amplifiers for neural recording and stimulators for neural stimulation) as well as various cutting-edge technologies such as microfluidic [89], microcoil for magnetic stimulation [33] and ultrasonic backscatter for neural dust [34]. Therefore, the development of new extraneural electrodes using the flexible materials with better features is still desirable for neuroprostheses and bioelectronic medicine.

Several designs of flexible epineural interfaces were investigated to overcome current challenges in this thesis. The proposed designs basically seek non-invasive approach, which aims at reaching visceral nerve modulation for bioelectronic medicine in the future. Strip, split-ring, sling, and clip designs were suggested and demonstrated in the following chapters.

CHAPTER 3. FLEXIBLE EPINEURAL STRIP ELECTRODE (FLESE) FOR RECORDING IN SMALL NERVE

3.1. Motivation

Neural electrodes reveal the tradeoffs between high selectivity and low invasiveness. Even though LIFE and TIME show a higher level of selectivity for stimulation by implantation inside nerves, the intrafascicular approach itself can potentially cause nerve damage [21]. On the other hand, extraneural electrodes, such as a spiral cuff and FINE show effective selectivity for stimulation that is similar to acute trials with intrafascicular electrodes [1]. When it comes to recording, however, the low signal-to-noise ratio (SNR) is a major challenge of the cuff-type electrodes, since tight cuff for achieving close contact to a nerve causes eventual nerve damage [8]. In addition, a long length (at least 20 mm) of cuff is usually required for recording high-amplitude signal when tripolar configuration of recording is used [90]. There are limitations of this long-length cuff type: 1) increasing foreign body response exposing longer areas of interfaces between a device and a nerve, which results in changing the characteristic of implanted electrodes, such as changes in signal to SNR and decreases in the selectivity [70]; 2) unstable and unreliable device performance due to biomechanical issues resulting from contraction and expansion of the near muscles as a result of movements [69]; 3) difficulty of implanting in very small nerves that are close to visceral organs and dense tissue networks providing limited surgical and implantation space. Some solutions, such as parylene-based new cuff designs have been proposed for flexible and conformable contact on nerves [76, 77], there is still challenge in applying to

very small nerves (50–200 μm), such as branches of sciatic nerve, splanchnic, bladder, and vagus nerves that are currently getting attention for bioelectronic medicine. Therefore, developing new electrode design concepts is still desirable for advanced neural electrodes.

This chapter describes a flexible epineural strip electrode (FLESE) that closely sticks to a nerve without undue pressure. The FLESE has small size of strip-shaped body with three electrodes, which allows placing it longitudinally on various sizes of nerves, very much like band aid (**Figure 3.1a**). Flexible and biocompatible polyimide is used as body material (**Figure 3.1b**). In addition, the three sensing electrode metal contacts are coated with carbon nanotube (CNT) in reduce the interfacial impedance, as well as to improve the adhesive properties. Electrically elicited neural signals, elicited by different stimulation electrodes, are recorded by two different designs of FLESEs from main sciatic nerves of rats to investigate the feasibility of FLESEs.

3.2. Device Design

The FLESE attempts pressure-free neural interface to remove the risk of nerve damages caused by compression. Analogous to attaching a band aid, it has very small strip-shaped body and enables a longitudinal implant on various sizes of thin nerves. This novel design reduces significant nerve damage by just attaching the electrode to the nerve instead of wrapping or penetrating the nerve, while providing direct contact between the nerve and the metal sensors. For this functionality, the FLESE was fabricated from flexible and biocompatible polyimide. Another advantage is that the various nerve sizes have little effect

on the size of the electrode; in contrast, for a cuff electrode, the inner diameter of a nerve cuff has to be closely matched to the size of the nerve. Thus, the FLESE design allows implanting on very small nerves with 100 s of micrometer diameter. The electrode has a smooth geometry that prevents nerve trauma from sharp edges. Two different designs are investigated. Both have three sensing electrodes, where the diameter is 100 μm and spacing between the electrodes is 3 mm. To secure the electrode strip to nerves, several suture holes are located on the strip. Surgeons can use the holes to gently suture the electrode directly to the nerve bundle, through the epineurium. Initial design (**Figure 3.2a**) has 9 mm length and 1 mm width of strip. The second design (**Figure 3.2b**) has 7.5 mm length and 0.5 mm width of strip, as well as a ground round electrode on a longer body. These designs can, of course, be adapted to different nerve sizes and shapes.

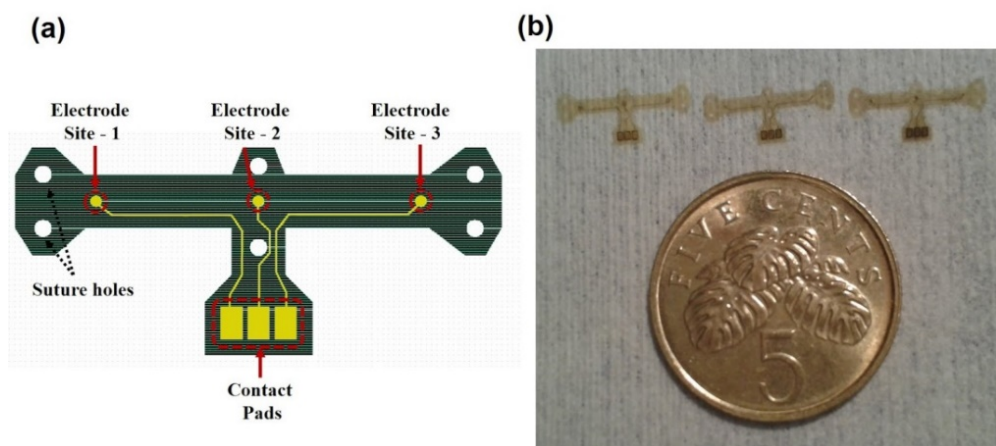


Figure 3.1 (a) The schematic diagram of a flexible epineural strip electrode (FLESE) and (b) a picture of the fabricated FLESE.

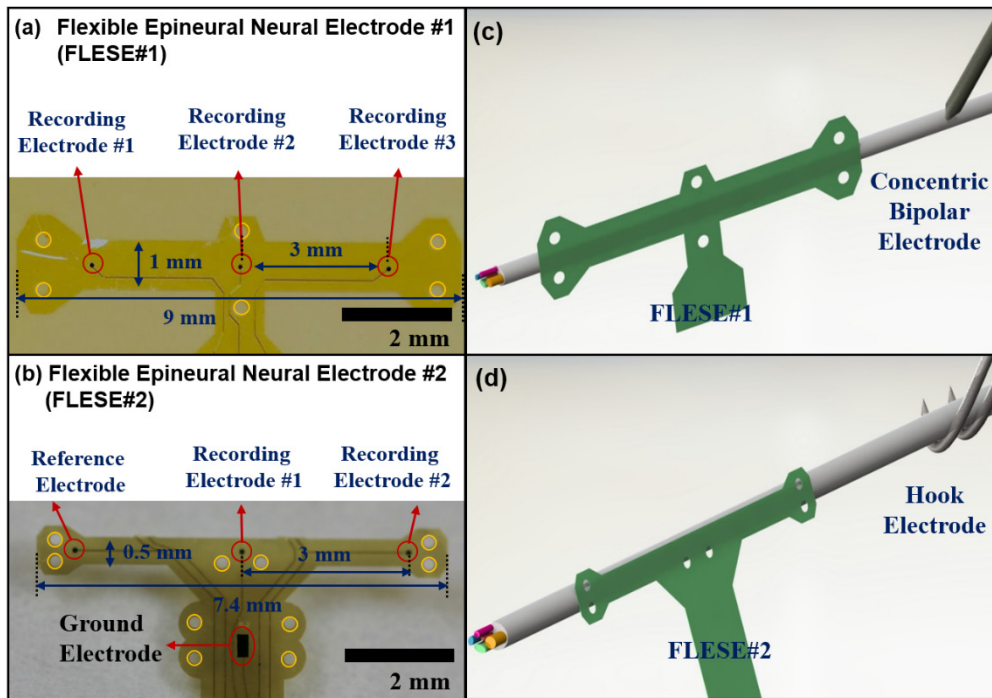


Figure 3.2 Pictures of the fabricated (a) FLESE#1 and (b) FLESE#2. Yellow circles indicate suturing holes for implantation on nerves. Schematic diagrams of configuration of implantations on a nerve, respectively, (c) FLESE#1 with a concentric bipolar electrode, and (d) FLESE#2 with a hook electrode.

3.3. Methods

3.3.1. Device Fabrication

The FLESEs are made of two layers of a non-photosensitive polyimide with gold sandwiched in between in strip-shape geometry. First, a 1 μm Aluminum (Al) sacrificial layer was deposited on a silicon substrate, then a 6 μm polyimide (PI2611, HD MicrosystemsTM, Parlin, NJ, USA) was spin coated and hard cured at 300 $^{\circ}\text{C}$ for 30 minutes at a 4 $^{\circ}\text{C}/\text{min}$ ramping rate (**Figure 3.3a**). After deposition of 200 nm Al as a hard mask, the bottom strip-shape geometry was patterned on the thin Al surface by a lithography step (**Figure 3.3b**). Afterward, the exposed polyimide was etched out by a reactive plasma etching process (O_2 gas flow 50 sccm and CF_4 gas flow 10 sccm, RF power 150 W). For finalizing

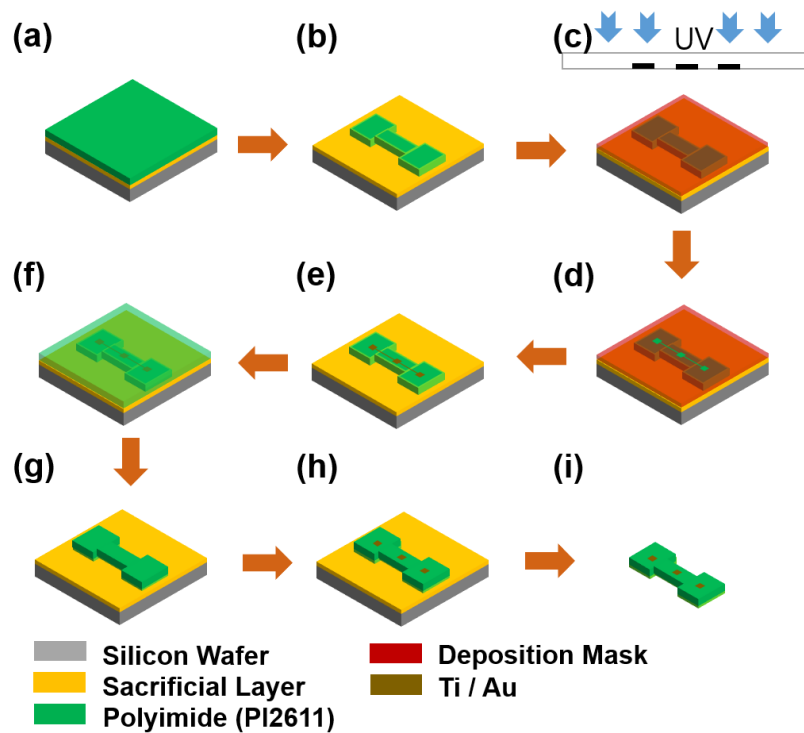


Figure 3.3 Fabrication process for the FLESE

the first layer, the rest of Al layer was removed (**Figure 3.3c**). Metal layers of Titanium (Ti) (20 nm), and gold (Au) (300 nm) for the epineural strip electrodes were subsequently deposited and patterned by metal evaporation and lift-off process (**Figure 3.3d–f**). The second layer of 6 μm polyimide was spin coated and hard cured at 350 °C for 30 minutes. The layer was also etched and patterned in the same way as the first layer for the top strip-shape geometry (**Figure 3.3g,h**).

3.3.2. Device Releasing and Packaging

The fabricated device was released from the Al-sacrificial etching using an electrochemical anodic dissolution process that not only could ensure a flat planar structure was released, but also was significantly faster than the

traditional wet etching process (**Figure 3.3i**). The Al-sacrificial layer on silicon substrate was bonded with copper wire extension encapsulating by nonconductive glue. Then, a platinum (Pt) mesh electrode as an inert electrode put together into a glass beaker of NaCl solution (2 M) with gentle magnetic stirring. Voltages were applied to the Pt electrode as cathode and the copper wire as anode. The voltage was set below 1 V to avoid O₂ formation at the anode. While applying the voltage, the Al electrode is dissolved into the electrolyte in the form of Al³⁺ or Al₂O₃ by oxidation and H₂ gases released from the Pt surface by H⁺ reduction. After around 20 minutes, the exposed portions of the Al sacrificial layer were removed, and only the covered portions of the Al sacrificial layer were left. Since the contact area between the Al sacrificial layer and the NaCl solution decreased, the current dropped, and the Al etching rate was reduced. Thus, the voltage was then increased to 20 V to speed up the release process. After the entire Al sacrificial layer was removed in 2 hours, the final device was released. Once the electrodes were released from the substrate, they were rinsed with 5% HCl acid to remove the suspended Al₂O₃ on the device surface.

The pad on the strip electrode was initially designed to match a commercial flexible printed circuit (FPC) connector (Hirose Electric Co. Ltd., Tokyo, Japan) so that pads could be inserted with a spacer into the connectors, and connected by simple clicking on them (**Figure 3.4**). It avoided damage to the thin-film electrodes from tethering forces applied during the *in vivo* experiments. The FPC connector was soldered to Omnetics cables (Omnetics Connector Corporation, MN, USA), and encapsulated with a flexible and biocompatible silicon tube. **Figure 3.5** shows the picture of the packaged FLESE.

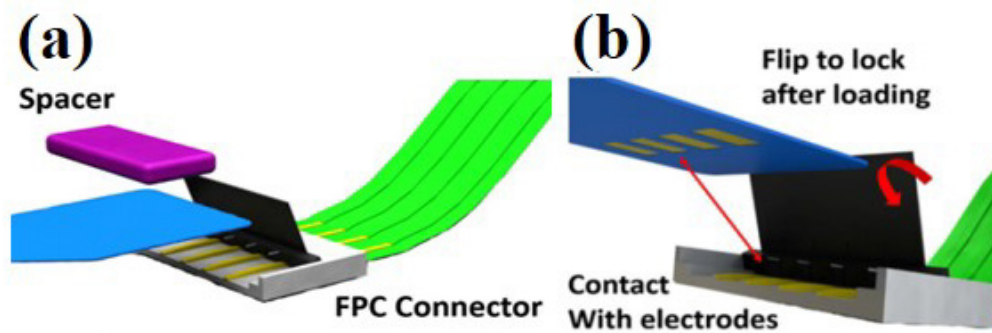


Figure 3.4 Illustration of packaging for the flexible neural electrode (a) Insert the electrode with spacer and (b) flip to lock after loading [91].

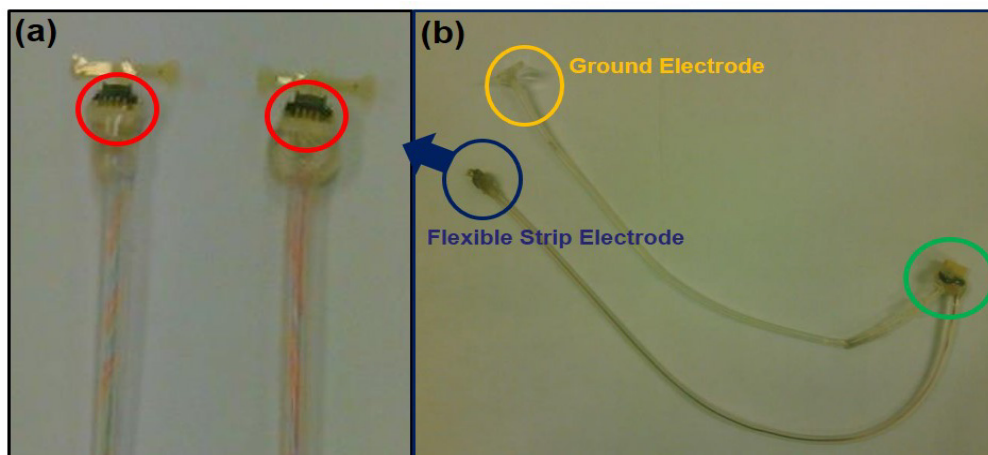


Figure 3.5 Pictures of (a) the assembled and (a) packaged FLESE.

3.3.3. Au-CNT Nanocomposites coating

Carbon nanotubes (CNTs) have drawn the great interest as an implantable electrode material since it shows the excellent mechanical property, low impedance and the superior charge storage capacity (CSC) [92-98]. Successful neuronal growth and interaction with CNTs has been demonstrated by several groups [93, 94]. In addition, CNT coated surfaces are neuro-adhesive in *in vitro* applications [94].

For the preparation of CNTs coating in this study, the MWCNTs (Cheap Tubes Inc., USA, length $\sim 0.5\text{--}2\ \mu\text{m}$, outer diameter $< 8\ \text{nm}$) were first dispersed

in an Au electrolyte bath (TSG- 250, Transene, USA) to form a $1 \text{ mg}\cdot\text{mL}^{-1}$ aqueous solution. Then, the whole solution was sonicated for 2 hours to fully suspend the CNTs in the solution. After that, the packaged FLESEs and Au wire were connected to the negative and positive terminals of the power supply, respectively. Both the electrode site and the Au wire were then inserted into the solution. The coating condition depends on applying voltage and time. Too low voltage does not allow coating CNT on the electrode while too much voltage damage the electrode. In addition, long time coating results in overcoating of CNT on the electrodes leading to being damaged during *in vivo* experiments. In this study, a monophasic voltage was controlled with varying the time. When the diameter of Au electrode is $100 \text{ }\mu\text{m}$, a monophasic voltage pulse with 1.1 V amplitude and 50% duty cycle are applied from the power source for 1 minute. Au ions in the solution, as well as CNTs which absorbed Au ions, migrated to the negative terminals. After absorbing the electrons from the probe contacts, the Au ions were subsequently deposited onto the surface of the recording contacts (**Figure 3.6**). The surface morphology of CNT-coated electrodes was characterized by scanning electron microscopy (SEM). **Figure 3.7** shows the SEM images of the electrode before and after the CNT coating. Au nanocomposites mixed with CNTs were formed on the surface demonstrating that CNT-Au nanocomposites were successfully coated on the electrode surface by the CNT coating method. This rough and highly porous surface coatings provide the increasing electrochemical surface area, and result in low interfacial impedance.

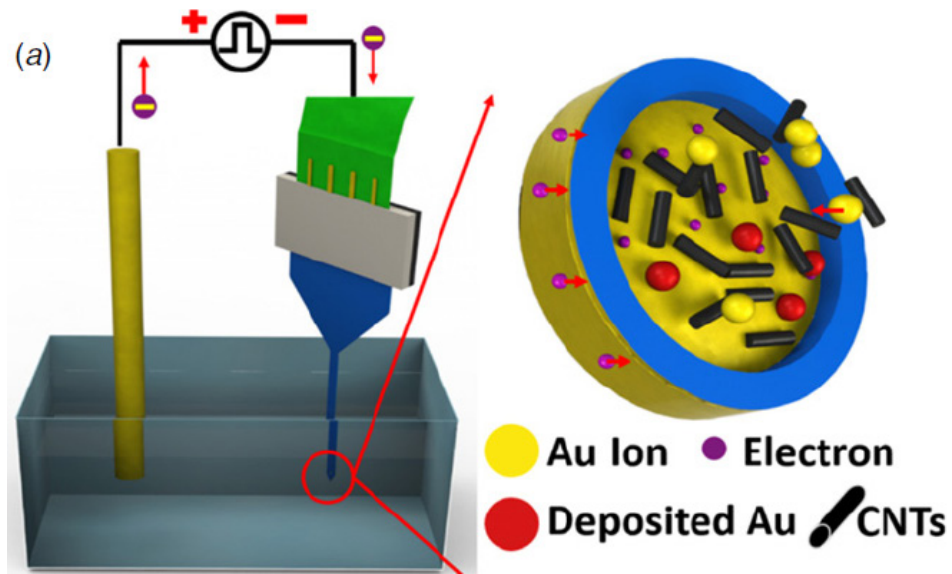


Figure 3.6 Schematic of the setup for the CNT coating [91].

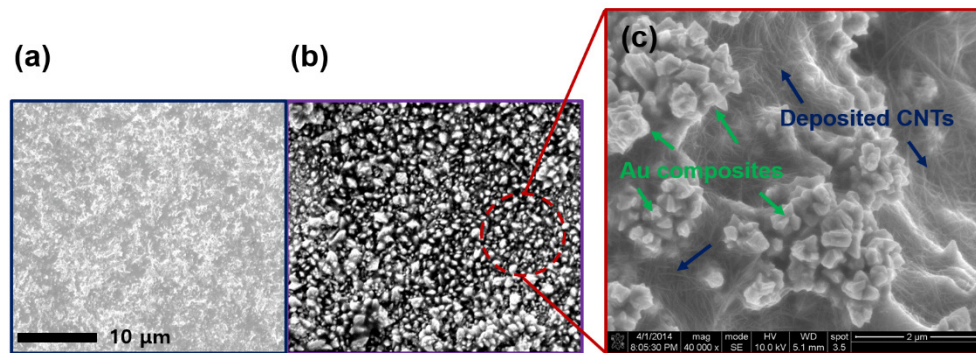


Figure 3.7 SEM images (a) before and (b) after CNT coating on electrodes. (c) The magnified SEM image after the CNT coating.

3.3.4. Electrochemical Impedance Spectroscopy (EIS) Characterization

Impedance characterization of interfacial layers is of paramount importance for the performance of neural recording. The neural signal will be corrupted by noise if the electrode impedance is not low enough [99]. To verify the change of interfacial impedances with and without Au-CNT-coated electrodes, EIS was conducted in phosphate buffered saline (PBS). The sinusoidal wave with an amplitude of 50 mV and frequency spans from 100 kHz to 0.7 Hz was applied.

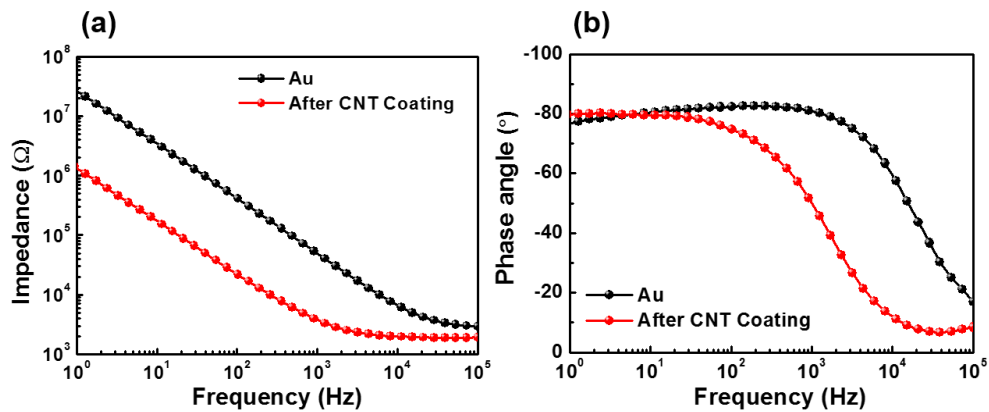


Figure 3.8 Results from EIS for (a) the plot of interfacial impedances for with and without CNT coating and (b) the plot of phase angle.

Three electrode configurations with the silver/silver chloride (Ag/AgCl) electrode and a Pt wire as reference and counter electrode, respectively, were used. The output impedance was recorded *in vitro* with an impedance analyzer (Autolab PGSTAT100N voltage potentiostat/galvanostat, Metrohm). The results of EIS are plotted in **Figure 3.8**. Impedance without CNT coating at 1 kHz was $47 \pm 7 \text{ k}\Omega$, while the impedance dropped by one order of magnitude ($3.6 \pm 0.6 \text{ k}\Omega$) after deposition of the CNT and Au composites and phase was -48° at 1 kHz. Since high impedance increases signal distortion and reduces SNR, Au electrodes without CNT coating cannot record neural signal with the high quality, while the impedance of electrodes with CNT coating is reasonably low and good for neural signal recording ($<10 \text{ k}\Omega$).

3.3.5. Rat Preparation for *in vivo* test

The experiments were performed in adult female Sprague Dawley rats (250 g) (In Vivos Pte Ltd, Singapore). The rats were acclimatized for one week prior to use in the experiment, with food and water provided *ad libitum*. The animal

care and procedures were approved by those outlined by the Agri-Food & Veterinary Authority of Singapore (AVA), the Institutional Animal Care and Use Committee (IACUC), and the ethics commission of the National University of Singapore. The methods were carried out in accordance with the 143/12 protocol. The detailed procedure is described in Appendix 2.

3.3.6. Physiological Characterization

The neural signals are evoked by electrical stimulation during acute recording tests (studies done under general anaesthesia); evoked activity is used for testing the neural signal recording as well as the calculation of nerve conduction velocity (NCV) [100, 101]. In this study, a sciatic nerve was directly stimulated, and the evoked compound nerve action potentials (CNAPs) were recorded from the sciatic nerve. The nerve was stimulated by the application of a single monophasic 20 μ s pulse, with amplitudes varying between 0.3 and 1.5 mA, using an isolated stimulator box (Digitimer Ltd., Garden City, UK). This range (6-30 nC Phase⁻¹) is acceptable according to the previous studies [65, 66]. Signals from the implanted FLESEs were acquired using a multichannel amplifier (Multichannel Systems MCS GmbH Inc, Reutlingen, Germany), at a sampling rate of 50 kHz and a gain of 2000. Data acquisition was done using the MCS system and the data acquisition software (MCRack).

3.3.7. Stimulation Electrode and Recording Configuration

A concentric bipolar electrode (Microprobe, Inc., Gaithersburg, MD, USA) as a stimulation electrode was implanted proximity to the spinal cord. Bipolar recordings were conducted using three sensing electrodes of FLESE#1 distally

placed at about 10 mm distance from the stimulus site (**Figure 3.9a**). The reference electrode was placed in the body in an electrically neutral place. Ground electrode was separately connected to the tail of the rat. A lab-made hook electrode as another stimulation electrode was implanted at the stimulus site. For differential bipolar recording, one reference electrode and two sensing electrodes from FLESE#2 were placed on the sciatic nerve.

3.3.8. Data Analysis

Electrophysiological data were analyzed using custom-written algorithms in Matlab (Mathworks, Inc. USA). The compound neural action potentials (CNAPs) and compound muscle action potentials (CMAPs) were identified after the stimulus artifact. The mean CNAPs and CMAPs were obtained from over 50 trials with intervals of 1 second between trials.

3.4. Results

3.4.1. *In Vivo Recording (FLESE#1 and Bipolar Configuration) Elicited by a Concentric Bipolar Electrode*

The FLESE#1 was successfully sutured on a sciatic nerve by microsurgical techniques (**Figure 3.9b**). **Figure 3.9c** shows the recorded CNAP from three different electrodes (E#1, E#2, and E#3) for varying stimulation currents. Each trace corresponds to the average obtained from recording over 50 CNAPs. The CNAPs were recorded following the stimulation artifact: 1) there were no CNAPs of significant amplitude recorded from the electrodes during the stimulation of 0.3 mA, 2) whereas clear and fine neural signals were recorded from the three electrodes at 1 mA, and 3) after the stimulation currents of more

than 1 mA, the amplitude of recorded signals did not increase. This experiment demonstrates that the stimulation current of around 1 mA is the threshold for stimulation of the sciatic nerve by the concentric bipolar electrode. The latency of peak of the CNAP that indicates the time from the onset of the stimulation artifact to the onset of the CNAP was 0.41, 0.42, and 0.44 ms, respectively, from the three electrodes. NCV can be calculated by the below equation [100, 101] :

$$\text{NCV} = \Delta x / \Delta t \quad (1)$$

where Δx is the distance that CNAP travels, and Δt is the time that it takes to cover this distance. The calculated NCV is 24–36 m/s. This matches well with the established NCV of the fastest fibers in rat sciatic nerves [100, 101]. The mean amplitude of CNAP from E#1 was $716.15 \pm 39.74 \mu\text{V}$, that of E#2 was $584.28 \pm 42.9 \mu\text{V}$ and that of E#3 was $272.94 \pm 50.55 \mu\text{V}$. This can be attributed to the difference in the distance between the sensing electrodes and the reference electrode. To verify whether the recorded CNAPs are corrupted by any external noises, such as EMG or the source of stimulation, xylocaine that is normally used for blocking nerve function [102] was applied to the nerve during stimulation with 1 mA current, and CNAP recordings were conducted after 10 min. The result of recorded CNAP after 10 min shows that no signal was recorded except for the stimulus artifact (**Figure 3.9d**). This demonstrates that the recorded CNAP before blocking nerve is not corrupted. However, the needle-type concentric electrode showed some issues in that it was challenges in keeping the same stimulus position during the stimulation due to the induced muscle movement.

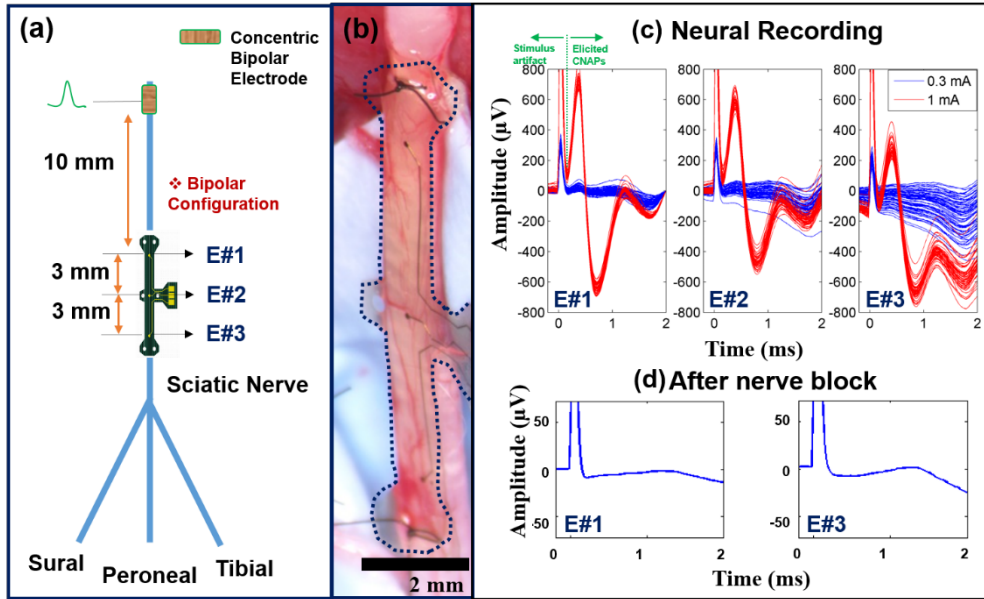


Figure 3.9 (a) Schematic diagrams of implanted FLESE#1 and (a) a picture of implanted FLESE#1 (c) Results of CNAP recordings of FLESE#1 on a main sciatic nerve elicited by the concentric bipolar electrode. (d) The recording after applying xylocaine for a nerve block.

Accordingly, repeatable pricking was required for the same stimulus position, resulting in bleeding the sciatic nerve, which eventually degraded the normal neurological condition.

3.4.2. *In Vivo* Recording (FLESE#2 and Differential Bipolar Configuration)

Elicited by a Hook Electrode

The FLESE#2 has narrower strip body that easily sticks even on the smaller branches of sciatic nerves (the diameters of 0.2–0.3 mm) compared with the FLESE#1. Also, it has longer tail body to the connector so that it allows for a stable implantation by reducing the tethering force. Also, ground electrode is on the tail body so that an additional or separate ground electrodes is not necessary, which again would be desirable for long-term implantation. The FLESE#2s were readily put on the main sciatic nerve and very small branch nerves (**Figure**

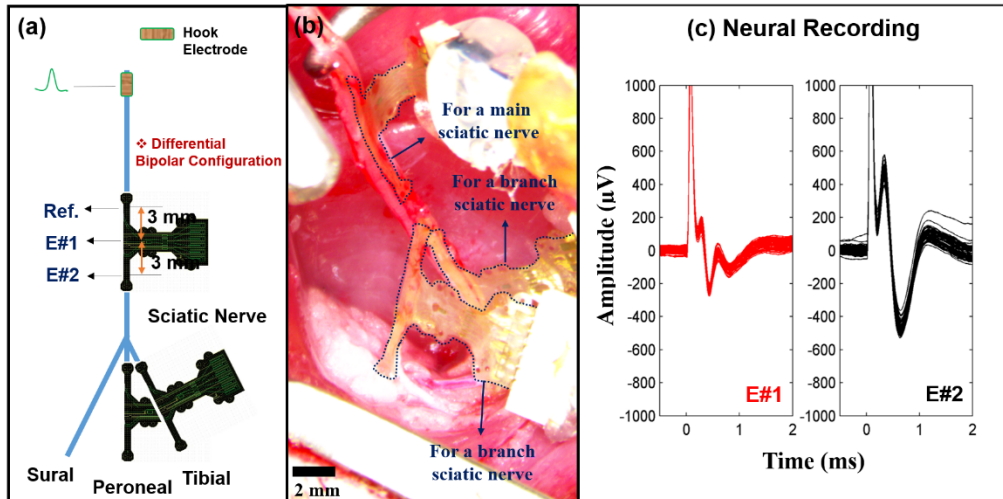


Figure 3.10 (a) Schematic diagrams of implanted FLESE#2 and (b) a picture of implanted FLESE#2 on rat sciatic nerves. (c) Results of CNAP recordings of FLESE#2 on a main sciatic nerve elicited by the hook electrode.

3.10a,b). Furthermore, they showed good adhesive properties to stick to the nerves without any suturing during the acute recording procedure. This might be due to the narrow width of the strip body, which reduces noncontact areas, promoting a stronger interface between the strip body and the nerve, as well as CNT's adhesive properties. Differential bipolar configuration was used for CNAP recording. It is a more effective way for recording in that the activity that is distant from both electrodes appears as common mode to the two recording electrodes, and is rejected, while activity in the immediate vicinity of the two electrodes appear in differential manner and is amplified [90]. Unlike the bipolar configuration which requires an additional reference electrode put inside the body, it does not suffer from long-term implantation issue. One sensing electrode on the FLESE#2 was set as a reference electrode and the other two sensing electrodes were set as recording electrodes (**Figure 3.10a**). Also, the hook electrode was used as the stimulation electrode for more reliable and repeatable stimulation. The stimulation protocol was as described earlier.

Threshold for stimulation current was found to be around 1 mA, and clear and fine CNAPs were recorded. **Figure 3.10c** shows the result of recorded CNAP ($n = 60$) from the two recording electrodes on the FLESE#2 in a rat main sciatic nerve elicited by the hook electrode with stimulus current of 1 mA. The mean amplitude of CNAP from E#1 was $235.7 \pm 20.1 \mu\text{V}$ and that from E#2 was $466.1 \pm 34.6 \mu\text{V}$. The difference of amplitude is most likely due to the nature of conduction or organization of axonal fiber/fascicles or placement. The shorter distance between reference and E#1 compensates CNAP resulting in low amplitudes [90]. In the main sciatic nerve, distance gap of 3 mm between the recording electrode #1 and #2 resulted in a $230 \mu\text{V}$ difference. For noise analysis, the mean amplitude of the noise from the electrodes was $12.60 \pm 0.84 \mu\text{V}$, which were identified before and after the CNAP.

3.5. Discussion

The FLESEs were proposed and investigated as new concepts for recording from small nerves. Here is the summary of the chapter and key findings.

- This novel design provides pressure-free interface on nerve, which would solve the changes such as pressure applied on a nerve and biomechanical issues during chronic implantation.
- The Au-CNTs-coated electrodes was used for peripheral nerve recording for the first time, which showed good interfacial impedance as well as good adhesive properties on a nerve.
- Clear and fine CNAPs were recorded through bipolar and differential bipolar configuration using this FLESE via epineural approaches thanks to unique design and good interfacial properties

of the Au-CNT coated electrode.

- The FLESE#2 not only showed good adhesive properties for implantation without suturing during acute recording experiment, but the longer tail body was also beneficial for reducing the tethering force that would be encountered during implantation.
- The recorded CNAPs demonstrates that 3 mm distance between reference and recording electrodes for differential bipolar configuration is enough to record clear CNAPs, although the amplitude is lower than with a 6 mm distance. It means that total length of strip body can be further reduced maintaining the maximum recording ability.

Overall experimental results demonstrate that FLESEs shows positive possibilities for sciatic nerve recordings in terms of pressure-free implantation on sciatic nerve and branches as well as fine CNAPs recordings using bipolar and differential bipolar configurations via epineural approaches. It could play an important role in small nerve recording in near future.

Towards next step of clinical applications, multichannel neural electrodes placed around the nerve will also be required for bidirectional neural interface.

CHAPTER 4. FLEXIBLE SPLIT RING ELECTRODE FOR SELECTIVE STIMULATION AND NEURAL RECORDING

4.1. Motivation

Recording and stimulating of peripheral nerves is an importance feature for bidirectional communication with neuroprosthetic systems. Furthermore, enabling quick and easy implantation at any desired position on peripheral nerves will be a powerful advantage for a neural interface used in physiological studies and neuromodulation applications.

This chapter demonstrates a novel split ring electrode for selective stimulation and neural signal recording on rat sciatic nerves to demonstrate possibility of bidirectional neural interface. Active electrodes of the split-ring interface enable easy and reliable implantation around the nerve so that selective stimulation of the sciatic nerve can be confirmed by different corresponding muscle activation patterns (**Figure 4.1a**). In addition, neural recordings using a transverse differential bipolar configuration is also conducted (**Figure 4.1b**). Commercial cuff electrode is also implanted on the sciatic nerve for affirming the recording setup and is used as benchmark for the flexible split ring electrode.

4.2. Device Design

The split ring electrode design attempts to reduce the risk of nerve compression by using flexible polyimide tips, so that it allows good electrical contact with epineurium of the nerves instead of penetrating or wrapping it,

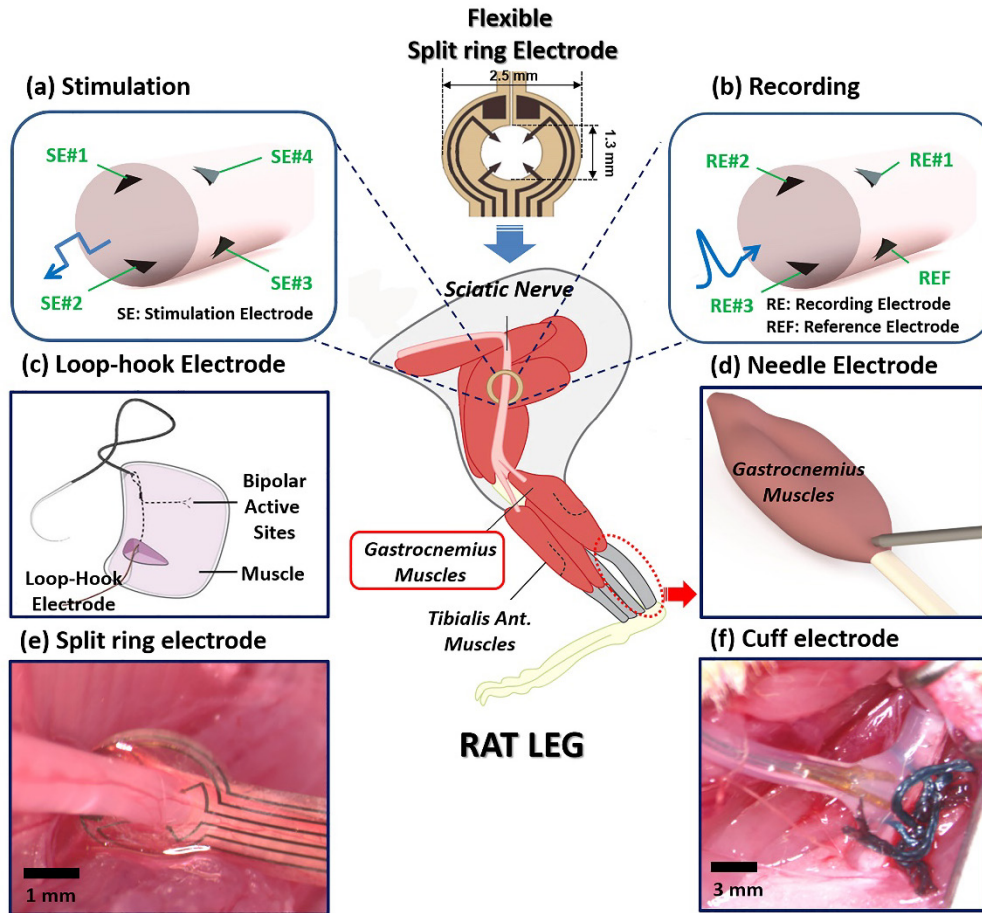


Figure 4.1 Schematic diagram of the experimental setup. Schematic diagram of the implanted flexible split ring electrode on the sciatic nerve for (a) stimulation and (b) recording. (c) Schematic diagram of an intra-muscular loop-hook bipolar electrode implanted in either the tibialis anterior or gastrocnemius muscles. (d) Schematic diagram of subdermal electrical stimulation of the hind limb using a needle electrode. Picture of the implanted (e) flexible split ring electrode and (f) commercial cuff electrode (Microprobe Inc., Gaithersburg, MD, USA) on the sciatic nerve in rats.

which may potentially cause nerve damages. The split ring electrodes consist of an open ringed structure of 1.3 mm inner diameter and tips of 500 μm inner diameter, while the outer diameter is 2.5 mm, so it can fit to a nerve diameter of 0.9–1.3 mm. Four triangular bendable 8,500 μm^2 equidistant sensing electrodes protrude from this ring (**Figure 4.2**, inset). The split ring enables easy

implantation by slotting nerves into the ring after opening the split part (Figure 4.2).

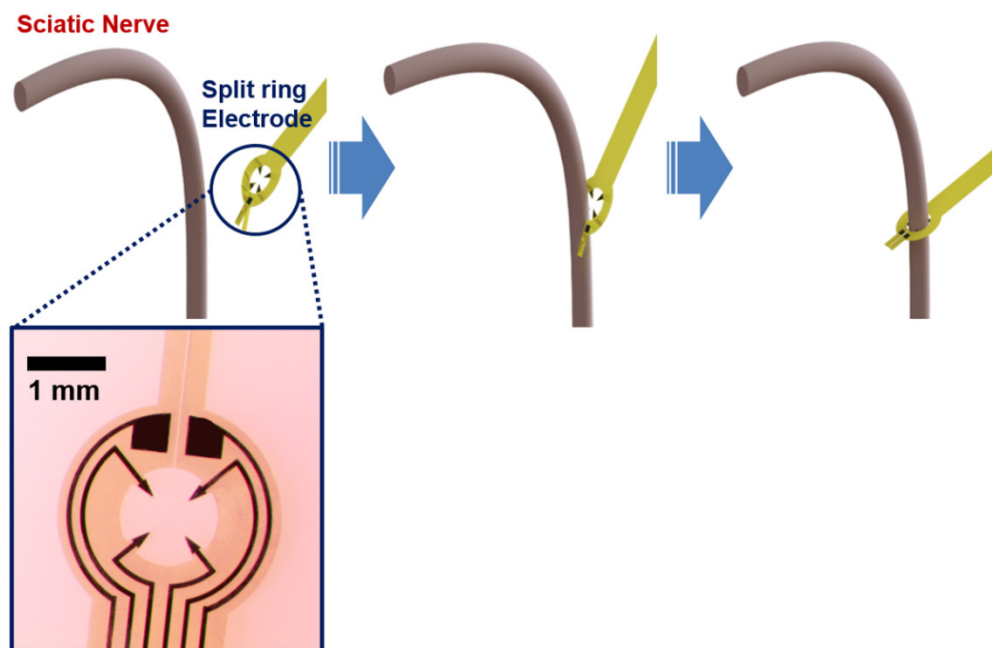


Figure 4.2 Schematic diagram of implanting a flexible split ring electrode on a sciatic nerve. (Inset) Picture of the fabricated split ring electrode.

4.3. Methods

4.3.1. Device Fabrication

The flexible split ring electrode consisted of two layers of biocompatible polyimides with Au/Pt electrodes sandwiched in a split ring-shaped geometry. All fabrication process is the same as the one for the FLESE except for the deposition of metal layers of Ti (20 nm)/Au (300 nm)/Pt (200 nm). **Figure 4.3** shows the fabrication process for the split-ring electrode.

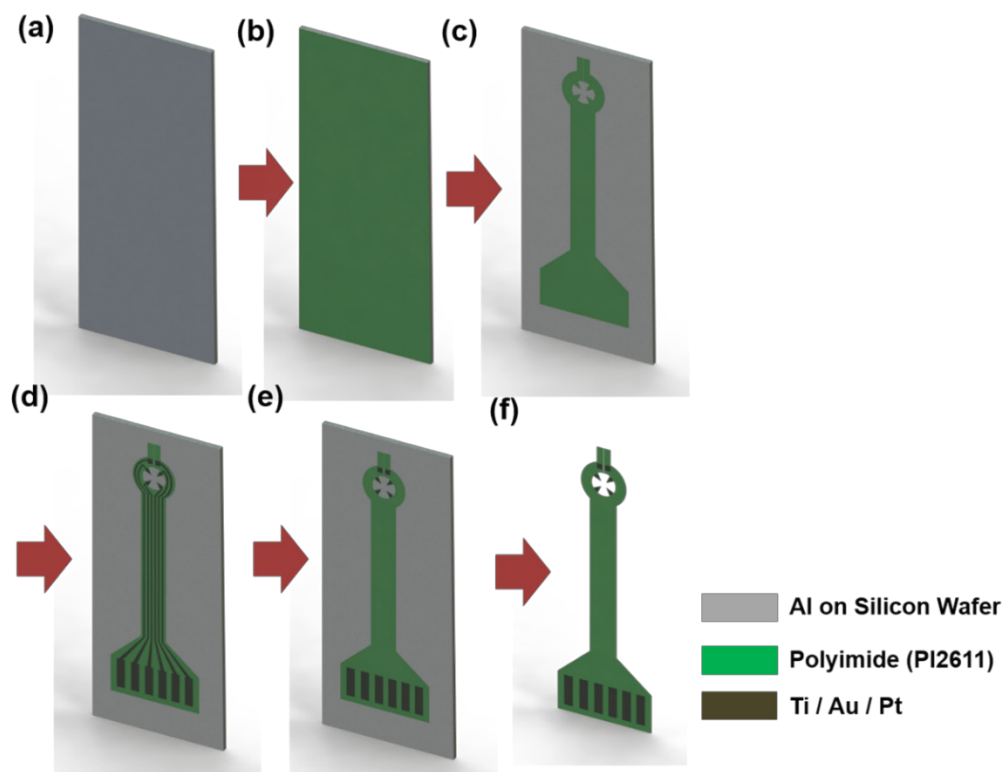


Figure 4.3 Fabrication process of a flexible split ring electrode.

4.3.2. Electrochemical Impedance Spectroscopy (EIS) Characterization

Characterization of an electrochemical interface is not only importance for neural recording but also for stimulation. Electrodes with lower impedance are better suited for both stimulating and recording electrodes [99, 103]. Also, if charge delivery capacity (CDC) is poor, high current amplitudes will be required for the activation of the nerves, which may also cause nerve damage or delamination of the electrode surface [104]. The electrochemical characterization of the split ring electrode was conducted to evaluate the device. A conventional three-electrode setup was used. The Pt split ring electrode was used as a working electrode (WE) while a silver/silver chloride (Ag/AgCl) and a Pt wire gauze electrodes were

used as the reference (REF) and counter electrode (CE), respectively, in phosphate buffered saline (PBS) (**Figure 4.4**). Impedance measurement was performed in a frequency range of 0.5 Hz – 30 kHz with a sinusoidal wave with amplitude of 10 mV. The output impedance was recorded with an impedance analyzer (Zennium E, ZAHNER-elektrik Inc, Germany). Water window from -0.6 V to 0.8V, which is normal range for Pt, was chosen with sweep rate of 50 mV/s for the cyclic voltammetry (CV) test. The charge delivery capacity (CDC) was calculated using the following equation (2) [76, 105],

$$CDC = \frac{1}{v} \int_{V_c}^{V_a} |i| dE \quad (2)$$

where E is the electrode's potential versus Ag/AgCl (V), i is the measured current density (mA/cm²), v is the scan rate (V/s), V_a and V_c are the anodic and cathodic potential limits (-0.6 V to 0.8 V), respectively.

The mean impedance of one sensing Pt electrode was 6.25 kΩ at 1 kHz, which was 7 times lower than Au electrodes (**Figure 4.4b**). Also, it shows a small capacitive phase angle at low frequencies, which indicates capacitive impedance (**Figure 4.4c**). The mean charge delivery capacity was 3.13 mC/cm². Also, the mean cathodic charge storage capacity (CSCc) was 2.4 mC/cm² indicated by the cathodic area of the CV plot (**Figure 4.4d**). These values are comparable to materials used previously in the literature for neural stimulation [76, 105]. The results demonstrate that the Pt split ring electrode can be used for *in vivo* recording and stimulation experiments.

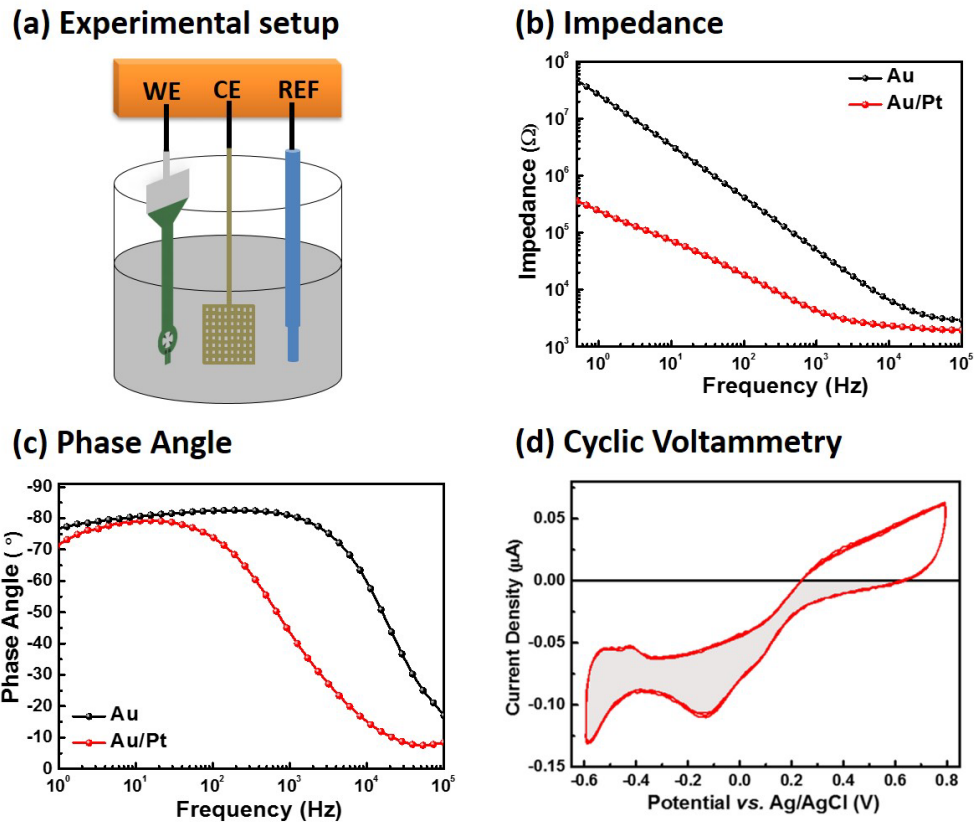


Figure 4.4 (a) Experimental setup for electrochemical impedance spectroscopy (EIS) and cyclic voltammetry (CV) test. The results of EIS for impedance and phase angle for Au and Pt electrodes ($n=12$) are shown in (b) and (c), respectively. (d) The results of CV for the Pt split ring electrodes ($n=6$).

4.3.3. Physiological Characterization

The procedure and rat preparation was the same as the one for the FLESE. The neural stimulation consisted of a single monophasic 20 μs pulse, with amplitudes of 50, 100, and 200 μA , were produced using the isolated stimulator box. This stimulation protocol was alternatively applied using each of the six possible combination pairs from the four contacts of the stimulation electrode (SE #1-2, SE #2-3, SE #3-4, SE #1-4, SE #1-3 and SE #2-4) around the sciatic nerve (**Figure 4.5a**). Over 50 trials were applied per stimulation session at a frequency of 1 Hz. In addition, the muscle recordings by the bipolar loop-hook

electrodes were acquired using a multichannel amplifier (Multichannel Systems MCS GmbH Inc, Reutlingen, Germany) with data acquisition software (MCRack), at a sampling rate of 50 kHz and a gain of 75. The signals were band-pass filtered between 300 Hz and 3 kHz. Individual recordings from the same muscle electrode were subtracted during offline processing. Peak-to-peak noise amplitude was measured to be $2.66 \pm 0.21 \mu\text{V}$. Also, a stainless steel needle inserted in the base of the tail was used as ground.

For the nerve recordings, CNAPs were evoked by subdermal electrical stimulation of the hind limb using a needle type stimulation electrode. This method was used for safe and repeatable activation of sensory receptors. The hind limb was stimulated by the application of a single monophasic 200 μs pulse, with amplitudes varying between 1 to 3 mA, using the isolated stimulator box. To verify the recording setup on sciatic nerves, a commercial cuff electrode (Microprobe Inc., Gaithersburg, MD, USA) (Pt, 100 μm , inside diameter: 1.0 mm, rings spacing: 3 mm apart) was also used under the same recording setup. The multichannel amplifier and the data acquisition software were also used for the neural signal recordings, at a sampling rate of 50 kHz and a gain of 100. The mean values of CNAPs were obtained from over 60 trials at a frequency of 1 Hz per recording session.

4.3.4. *Data Analysis*

Electrophysiological data were analyzed using custom-made algorithms in Matlab and Igor Pro (Wavemetrics, Inc. USA). The CNAPs and CMAPs were identified after the stimulation artifact, then, peak-to-peak amplitude were

estimated. Statistical comparisons were performed with SPSS software (IBM Corp., USA). An independent Student *t*-test was used for comparisons between the conditions. Analysis of variance was used to determine statistical significance. Significance was accepted at 5% ($p < 0.05$). Values are shown as mean \pm S.E.M. (standard deviation of mean).

4.4. Results

4.4.1. Selective stimulation of a sciatic nerve

Selective stimulation of the sciatic nerve was conducted while recording compound muscle action potentials (CMAPs) of the Gastrocnemius Medialis (GM) and Tibialis Anterior (TA) muscles to characterize the relationship between muscle activation and contact location. At lower stimulation current amplitudes (less than 100 μ A), none of the paired contacts could elicit detectable CMAPs. As the current amplitude increased, the muscle activation patterns corresponding to each of the contact pairs appeared. CMAPs were evoked (along with the flexion or extension of the leg) using electrode pairs Stimulating Electrode (SE) #1-#4, SE#1-#2, and SE#2-#3 starting from stimulation currents of 200 μ A (**Figure 4.5a**). The electrode pair SE#1-#4 activated the GM muscle, but activation of the TA muscle was negligible (**Figure 4.5b**). This indicated that the fascicles inside the sciatic nerve, which controlled the GM muscle, were closer to the positions of electrodes SE#1-#4. For the electrode pair SE#1-#2, the amplitude of CMAPs from the TA muscle was 2.5 times higher than those from the GM muscle (**Figure 4.5c**). This activated both muscles. The electrode pair SE#2-#3 activated the TA muscle 3

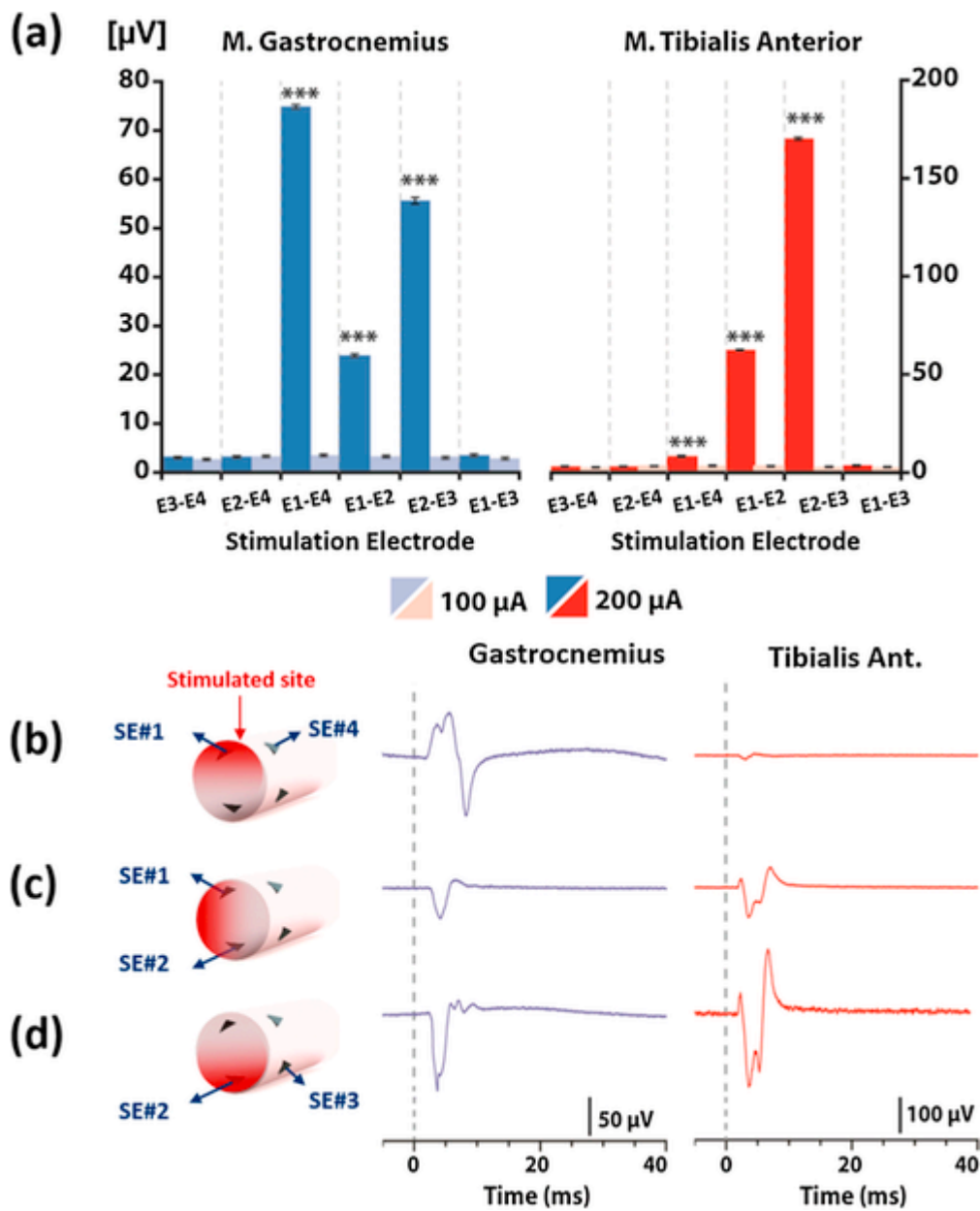


Figure 4.5 (a) This plot shows the evoked compound muscle action potential (CMAP) in the Gastrocnemius Medialis (GM) (blue) and Tibialis Anterior (TA) muscles (red) as a function of electrode pairs from a single monophasic 20 μs pulse with stimulation currents of 100 (light color) and 200 μA (dark color) ($n = 3$). The CMAP recordings from the GM and TA muscles are shown as a function of electrode pairs in (b) SE#1-#4, (c) SE#1-#2, and (d) SE#2-#3, respectively, using a single monophasic 20 μs pulse with currents of 200 μA .

times more strongly than the GM muscle, suggesting preferential activation of suggested that the activation of fascicles under the electrode pair SE#1-#2 the nerve fibers innervating the TA muscle compared to the GM muscle (**Figure 4.5d**). The rest of the electrode pairs were not able to stimulate the muscles effectively until much higher levels of currents of approximately 1 mA. With stimulation amplitudes greater than 1 mA, all electrode pairs elicited muscle contractions, but the muscle activation pattern of each electrode pair became indistinguishable. The results showed that different motor fascicles were activated by different electrode pairs, thereby demonstrating selective stimulation of the sciatic nerve to activate GM and TA muscles by the flexible split ring electrode at low stimulation currents (200 μ A). This low level of stimulation corresponded to 4 nC/Phase, which is an acceptable range for human applications [2].

4.4.2. Neural recording with transverse differential bipolar configuration

To investigate the quality of the neural recordings from the split ring electrode, the transverse differential bipolar configuration was used in *in vivo* experiments in this study. The compound neural action potentials (CNAPs) evoked by the subdermal electrical stimulation of the hind limb in rats (**Figure 4.1d**) were recorded by three sensing electrodes and one reference electrode, which were transversally positioned on the nerve (**Figure 4.6**). This transverse differential bipolar configuration provided several advantages; 1) it enabled the direct comparison of recording amplitudes among the sensing electrodes, 2) the implantation required a much smaller lateral space compared

to the conventional cuff electrodes, and 3) reduced the need for complicated signal processing procedures and calculations for evaluating selectivity. The subdermal stimulation primarily excited sensory receptors, evoking the activation of relevant fascicles inside the sciatic nerve. The clear CNAPs from the three sensing electrodes were recorded using stimulation currents of 2 mA, which is shown in **Figure 4.6**. As shown in Table 1, the mean amplitudes of the CNAPs were 33.7, 91.5, and 36.1 μV for Recording Electrode (RE) #1, #2, and #3, respectively. The mean latencies of the peak were 0.2 ms for all cases. The NCV was calculated to be 35 m/s, which is also consistent with values reported in the literature [100, 101]. The mean noise level from the three sensing electrodes was measured as 7.4 μV , showing a SNR of 13 (SNR is based on absolute peak value/95th percentile noise value) on RE#2 (**Figure 4.6a**). Even though direct comparisons of the SNR with other studies are difficult due to the different experimental conditions (e.g. the size and material of the recording electrode, where the electrode was implanted, and the type of CNAPs), this SNR value is again quite consistent with those reported in the literature [31]. The recorded amplitudes on RE#2 were the highest among all the electrodes, possibly indicating that the fascicles activated by the subdermal stimulation were closest to RE#2. The recorded amplitudes on RE#3 were slightly higher than those on RE#1, but the difference was negligible, indicating that the fascicles close to RE#1 or RE#3 were also slightly activated by the subdermal stimulation, but they were negligible compared with the fascicles close to RE#2 (**Figure 4.6b,c**). This indicates that using the transverse differential bipolar configuration, the flexible split ring electrode was able to

distinguish subtle differences in the activation of the nerve fibers in the sciatic nerve.

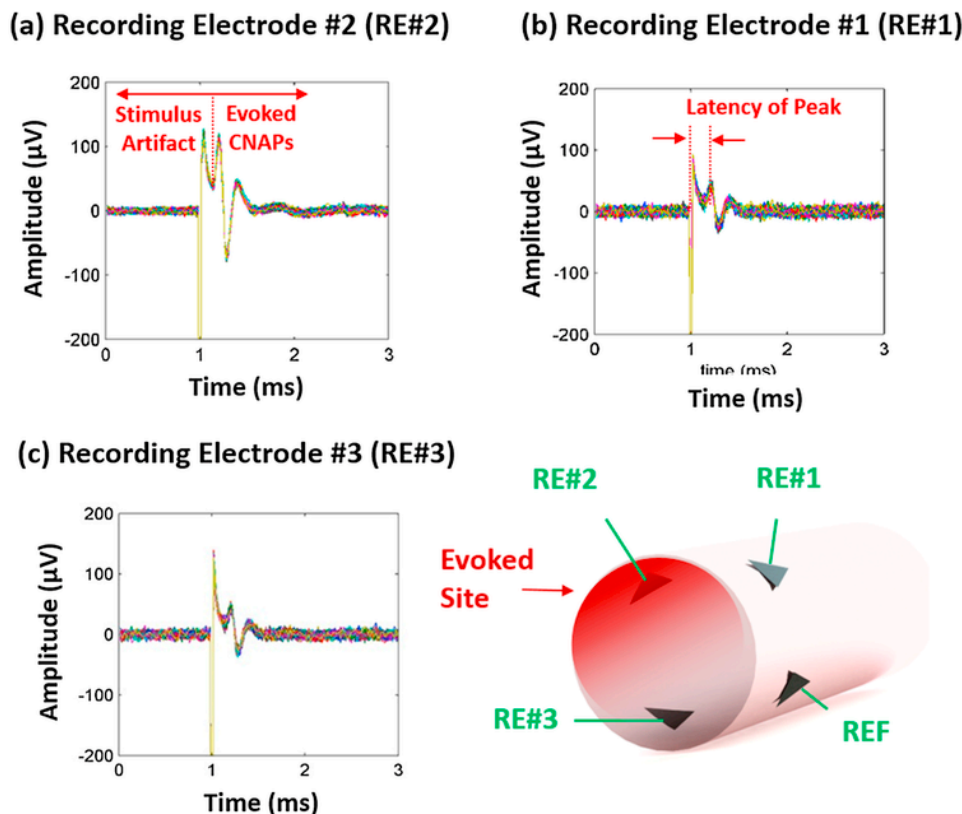


Figure 4.6 The compound neural action potential (CNAP) recordings from (a) recording electrode #2 (RE#2), (b) recording electrode #1 (RE#1), and (c) recording electrode #3 (RE#3) from the sciatic nerve evoked by subdermal electrical stimulation in the hind limb. Schematic diagram of the transverse differential bipolar configuration with three sensing electrodes and one reference electrode on the sciatic nerve. Red color highlights the evoked fascicles inside the sciatic nerve.

Table 2 The recorded compound neural action potentials (CNAPs).

	<i>RE#1</i>		<i>RE#2</i>		<i>RE#3</i>	
	Amplitude [μV]	Latency [ms]	Amplitude [μV]	Latency [ms]	Amplitude [μV]	Latency [ms]
<i>1st Peak</i>	42.23	0.2	112	0.2	43.92	0.2
<i>2nd Peak</i>	-25.25	0.28	-70.89	0.28	-28.2	0.28
<i>3rd Peak</i>	16.33	0.4	43.09	1.4	16.17	0.4
<i>Mean Amplitude</i>	33.74		91.45		36.06	

4.4.3. *Acute recordings using commercial Pt cuff electrode*

To verify the recording setup and the condition of the sciatic nerve, as well as to compare with the recording result from the split ring electrode, a commercial cuff electrode was also tested under the same recording setup after the previous recording experiment (**Figure 4.1f**). The evoked CNAPs were recorded with a stimulation current of 1.5 mA, and were saturated with a stimulation current of 2.5 mA (**Figure 4.7**). The mean amplitude was 67.2 μ V, and mean noise level was 13.2 μ V, showing a SNR of 5.3 when stimulated with a current of 2 mA. The SNR was 2 times lower than that by the split ring electrode, which might be due to slightly larger size of the cuff compared to the diameter of the sciatic nerve. The split ring electrode, on the other hand, was able to make close contact with the nerve across a range of dimensions. Also, the larger space required for the cuff electrode resulted in higher latencies than those recorded by the split ring electrode since the cuff electrode had to be implanted on the proximal segment of the sciatic nerve due to its length. In comparison, the split ring electrode was implanted on the end of the sciatic nerve closer to the muscles, and as a result, recorded lower latencies than those from the cuff electrode. This reduced latency may be advantageous if a quick reaction to a stimulus is needed, for example, when a pain receptor is activated by a pin prick. In addition, the flexibility of the split ring electrode allows us to implant the electrode at any desired position on a nerve. These results based on a commercial cuff electrode validated the recordings using the split ring electrode, but also highlighted the many advantages that the split ring electrode can potentially offer in neuromodulation

Neural Signal Recordings (Cuff electrode)

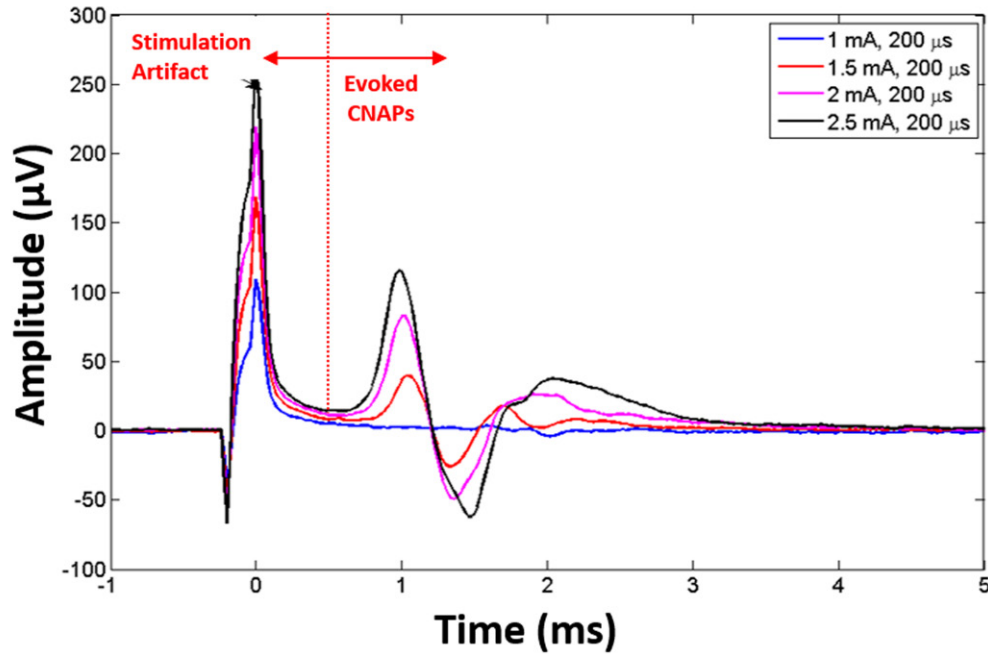


Figure 4.7 Compound neural action potential (CNAP) recordings with a pseudo-tripolar configuration from a sciatic nerve using a commercial cuff electrode (Pt, 100 μm , inside diameter: 1.0 mm, rings spacing: 3 mm apart).

and the control of advanced neural prosthetics.

4.5 Discussion

In this chapter, we demonstrated a split ring electrode for selective stimulation and recording. Here is the summary and key features.

- Due to its unique design, split ring electrodes can be used for quick and easy implantation at any desired position on peripheral nerves, which is a powerful advantage for a neural interface used in physiological studies and neuromodulation applications.
- The results of the selective stimulation demonstrated that the GM and

TA muscles were selectively activated by different pairs of active electrodes on a split ring electrode using a transverse bipolar configuration and stimulation currents of 200 μ A.

- The results of the neural recordings demonstrated that small differences in evoked CNAPs could be distinguished using a transverse differential bipolar configuration.
- The SNR of the CNAPs recorded by the split ring electrode was higher than those from commercial cuff electrodes.
- The results of the selective stimulation and recording demonstrated that the split ring electrode could be used to figure out the position of desired fascicles inside peripheral nerves
- Specific stimulation targeted at only the nerve fibers that elicit desired effects without altering non-target functions.

In summary, our results demonstrated that this electrode design shows promising possibilities for recording and stimulating nerves, and may be suited for neuroprosthetics and bioelectronic medicine in the future. For the next step, the larger number of active electrodes for precise modulation of peripheral nerves will be also required for bidirectional neural interface.

CHAPTER 5. FLEXIBLE AND ADJUSTABLE SLING ELECTRODE WITH SELECTIVE NERVE RECORDING AND STIMULATION

5.1. Motivation

Even though the split ring electrode shows the promising results of recording and stimulation, an adjustable feature with good electrical contact as well as several configurations of neural interfaces for effective recording and stimulation are still required.

In this chapter, we demonstrate a flexible and adjustable neural interface for selective nerve recording and stimulation with good electrical contact but minimal pressure on rat sciatic nerves (**Figure 5.1**). Electrochemical characterization of Pt-black coated interfaces for recording and stimulation was conducted. For *in vivo* studies, the common peroneal (CP) nerve, which is one branch of the rat sciatic nerve, was electrically/partially evoked neural signals for selective recordings on the sciatic nerve (**Figure 5.1b**). Selective stimulation using a longitudinal tripolar configuration was also conducted while monitoring muscle signals, and was compared with stimulation using a transverse configuration in order to determine the most effective stimulation configuration using this interface design (**Figure 5.1c,d**). In addition, we measured blood flow in the sciatic nerve using functional photoacoustic imaging [106] to compare the pressure applied on the nerves by our neural interface and that applied by commercial cuff electrodes.

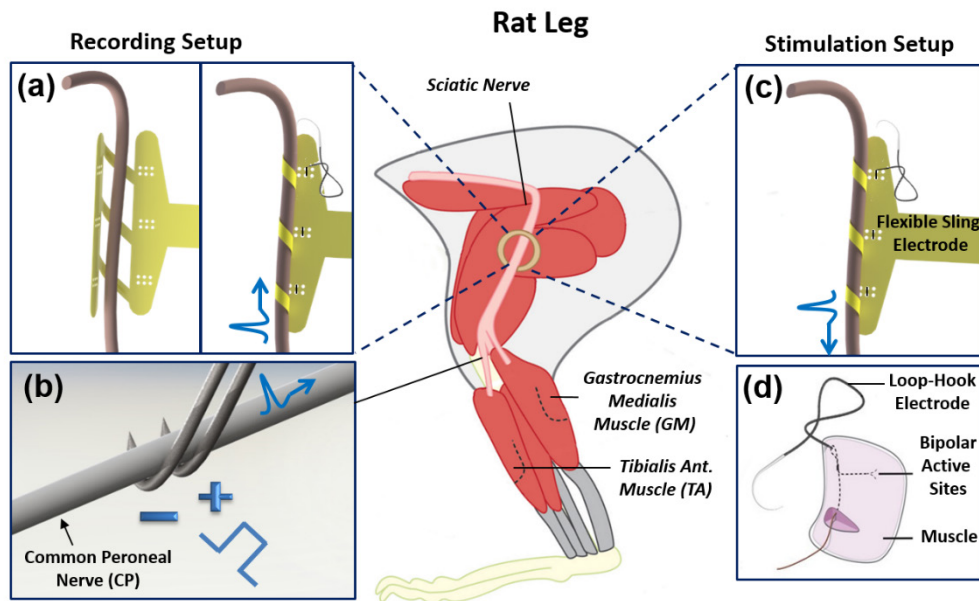


Figure 5.1 Schematic diagrams of experimental setup for recording and stimulation on a sciatic nerve. (a) Schematic diagram of an implanting flexible sling electrode on sciatic nerve for recording (b) Schematic diagram of an implanted hook electrode on common peroneal nerve for evoking neural signal. (c) Schematic diagram of an implanted flexible sling electrode for stimulation (d) Schematic diagram of an implanted loop-hook electrode on muscle for muscle signal recording.

5.2. Device Design

The flexible and adjustable sling electrodes are proposed to not only reduce the pressure applied on a nerve, but include several configurations for selective recording and stimulation. Furthermore, the design includes simple adjustable feature for nerves with slightly different sizes. It has six active electrodes (each 100 μm diameter) on a central bridge and two ring electrodes that surround the nerve on two neighboring bridges (**Figure 5.2a**). The three bridges are angled so that it allows the active electrodes to be helically implanted around a nerve while keeping a distance of 3 mm between the rings and the active electrodes (yellow arrows in **Figure 5.2a**). This also enables the electrode to reduce the pressure applied on the nerve surface while making good contact. For recording

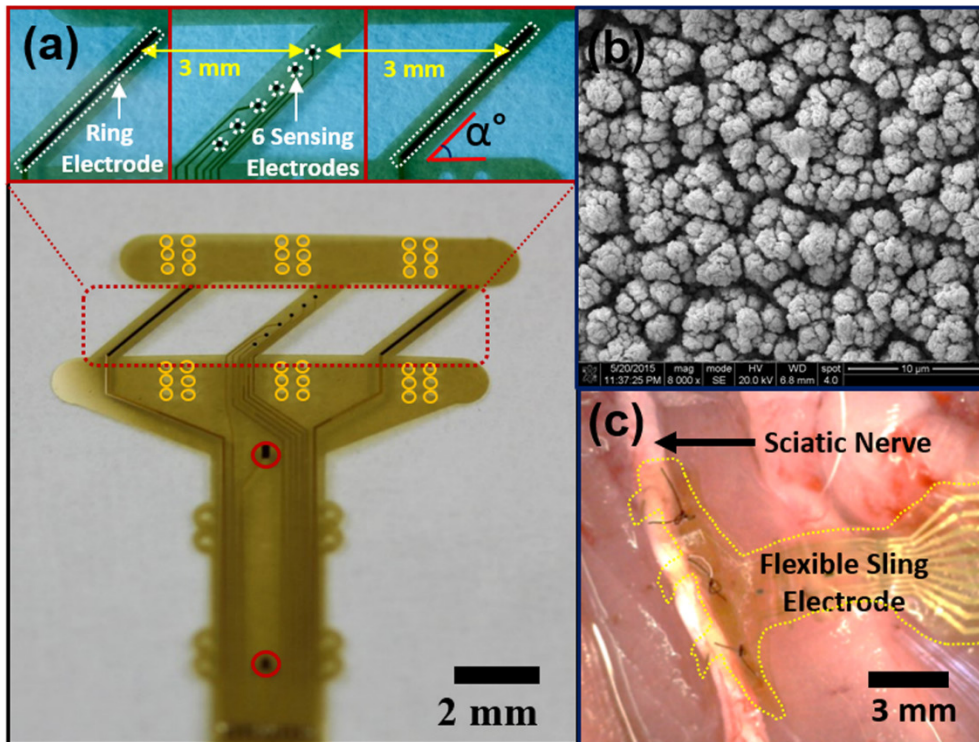


Figure 5.2 (a) Picture of fabricated sling electrode (b) SEM image of Pt-black coated electrode. (c) Picture of implanted flexible sling electrode on a rat sciatic nerve.

electroneurograms (ENG), it has been suggested that a tripolar configuration has advantages in enhancing SNR by rejecting most of the electromyography (EMG) signals from nearby muscles, as well as distant electrical noise sources, especially for extra-neural electrodes like cuff electrodes [90]. In particular, a mixed tripole, where two rings acting as reference electrodes are shorted together, performed better than other configurations in terms of high SNR [107]. In addition, this design allows us to set transverse or longitudinal tripolar configurations for selective stimulation.

Figure 5.1a shows how the sling electrodes were implanted on the sciatic nerve, in a manner analogous to hanging a nerve in a sling. In addition, several suturing holes on the body of the electrode (yellow circles in **Figure 5.2a**)

enable surgeons to suture the appropriate holes together with surgical thread to fit various sizes of nerves (diameter: 0.7~1.2 mm). Thus, it can easily be used on nerves with slightly different sizes. In contrast, for cuff-type electrodes, the inner diameter of a nerve cuff has to be closely matched to the size of the nerve, so different cuff electrodes have to be prepared for nerves with slightly different sizes.

5.3. Electrochemical Interface

5.3.1. Pt-black coated neural interfaces

The neural interfaces were fabricated using microelectromechanical system (MEMS) technology. It consisted of two layers of flexible polyimide with gold sandwiched in between in a sling-shape geometry. The fabrication procedure is the same as the one for the FLESE in Chapter 3. To enhance the performance of the electrochemical interface, the fabricated electrodes were subsequently coated with platinum (Pt) black, which has been commonly used for neural recording and stimulation [108, 109]. After the fabrication and assembly of the electrode, Pt-black was coated on the Au active electrodes by an electrochemical process. The electrolyte consisted of H_2PtCl_6 (5 g) (hexachloroplatinum-(IV)-acid hexahydrate) in deionized water (357 ml) and $\text{Pb}(\text{NO}_3)_2$ (71.4 mg) at room temperature. A 0.9 V DC voltage was applied to the sensing electrodes as cathode, and a gauze Pt electrode as anode for 1 minute. **Figure 5.2b** shows an image of the Pt-black coated neural interfaces measured by a SEM. The prepared Pt-coated electrodes were then implanted on sciatic nerves in rats for the *in vivo* test (**Figure 5.2c**).

5.3.2. Electrochemical characterization

The characterization of the electrochemical interface is of paramount importance for neural recording and stimulation. Electrodes with lower impedances are better suited for both stimulating and recording electrodes. Neural signals will be overwhelmed by electrical noise if the interfacial impedance is too high [99]. In addition, high electrode impedances will require high voltages to inject desired current amplitudes, which results in undesirable electrochemical reactions, possibly damaging both the electrode and the tissue. If the charge delivery capacity (CDC) is poor, high current amplitudes will be required for the activation of the nerve, which may also cause nerve damage or delamination of the electrode surface [103]. As shown in **Figure 5.2b**, this rough and porous surface has high electrochemical surface area (ESA) or real surface area, which enhances surface chemical reactions due to a higher Helmholtz capacitance than that of geometric surface area (GSA). This increases charge injection capacity (CIC) by dropping the electrode-electrolyte capacitance voltage, avoiding occurrence of unwanted redox reactions [103]. The electrochemical characterization of the Pt-black coated electrodes was conducted using the conventional three-electrode configuration (**Figure 5.3a**). The measurement procedure is the same as those described in earlier chapters.

The mean impedance of the Pt-black electrode was 2.3 k Ω at 1 kHz, which was 12 times lower than Au electrodes (**Figure 5.3b**). The phase angle of the Pt electrodes at 1 kHz was -4.9° (**Figure 5.3c**). This impedance is reasonably low, and thus suitable for neural recording. Also, it shows a small capacitive phase angle at low frequencies, which indicates capacitive impedance. The mean charge storage capacity (CSC) was 26.9 mC cm⁻². Also, the mean cathodic

charge storage capacity (CSCc) was 16.3 mC cm^{-2} , indicated by the cathodic area of the CV plot (**Figure 5.3d**). These values are comparable to materials used previously in the literature for neural stimulation [108, 109]. The calculations are also the same in previous sections. As shown in **Figure 5.3d**, the CV plot shows typical peaks for Pt-black, which indicates electrochemical reactions occurring at the electrode-electrolyte interface [76, 99, 103]. These results demonstrate that the Pt-black coated electrodes can be used for *in vivo* recording and stimulation experiments.

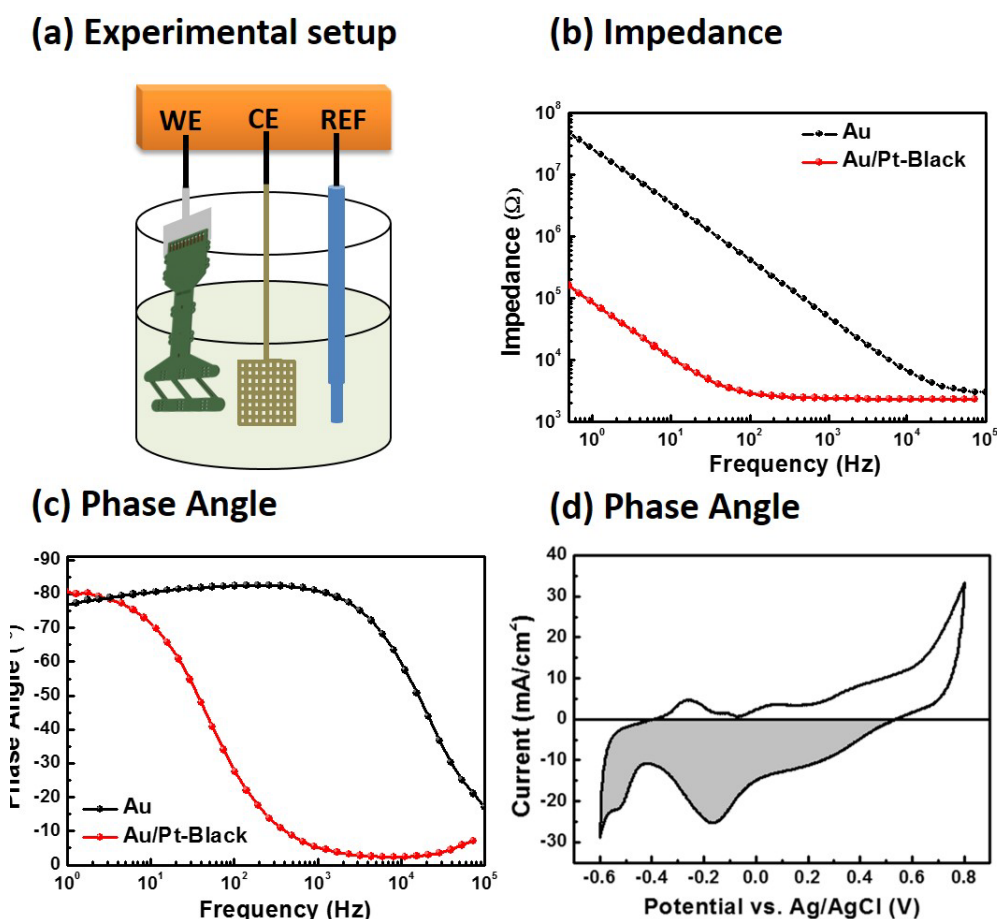


Figure 5.3 (a) Experimental setup for electrochemical impedance spectroscopy (EIS) and cyclic voltammetry (CV) test. The results of EIS of Au and Pt-black for (b) impedance and (c) phase angle. (d) CV plot of Pt-black coated flexible and adjustable sling electrode.

5.4. In vivo experiment

5.4.1. Neural recording of evoked CNAPs on sciatic nerves

For selective recording experiments, CNAPs from the main sciatic nerve were partially evoked by stimulating the CP nerve branch of the sciatic nerve. The evoked CNAPs were, then, individually recorded through the six active contacts (**Figure 5.4**). The first peak-to-peak voltage (V_{pp}) of the neural signals right after the stimulus artifact was measured, and the latency of the peak (i.e. the time from the onset of the stimulus artifact to the first peak of the CNAP) was also measured (**Figure 5.4a, inset**). The mixed-tripole configuration was used where the two rings that were acting as reference electrodes were shorted together, and the six electrode contacts in the middle individually worked as sensing electrodes (**Figure 5.4b, inset**). **Figure 5.4c** shows the mean and standard error ($n=50$) of the latency of the peaks from each of the six electrodes when stimulated with a current amplitude of 1.2 mA. The latency of the peak of the CNAP is important since it provides an estimate of the NCV. The mean latency for E#1 was 0.26 ms, while that for E#6 was 0.3 ms. This indicates that the six sensing electrodes made good contact with the nerve since the contacts were positioned helically around the main trunk where E#1 was closer to the stimulation site while E#6 was further away from the stimulation site. Since the distance between two electrodes (E#1 and #6) was 1.3 mm, NCV was 32.5 m s^{-1} , as calculated by equation (3) below [101, 110, 111],

$$NCV = \frac{\Delta x_2 - \Delta x_1}{\Delta t_2 - \Delta t_1} \quad (3)$$

, where Δx_1 and Δx_2 are distances from the stimulation site (or recording site), respectively, and Δt_1 and Δt_2 are the CNAP latencies measured at x_1 and x_2 , respectively. This ‘difference method’ is typically used for NCV calculation [101, 110, 111]. Also, the NCV matches well with the established NCV of the fastest fibers in rat sciatic nerve from literature [100, 101]. **Figure 5.4d** illustrates the mean and standard error (n=50) of the recorded amplitudes on different electrode contacts under stimulation currents of 1.2 mA. The recorded

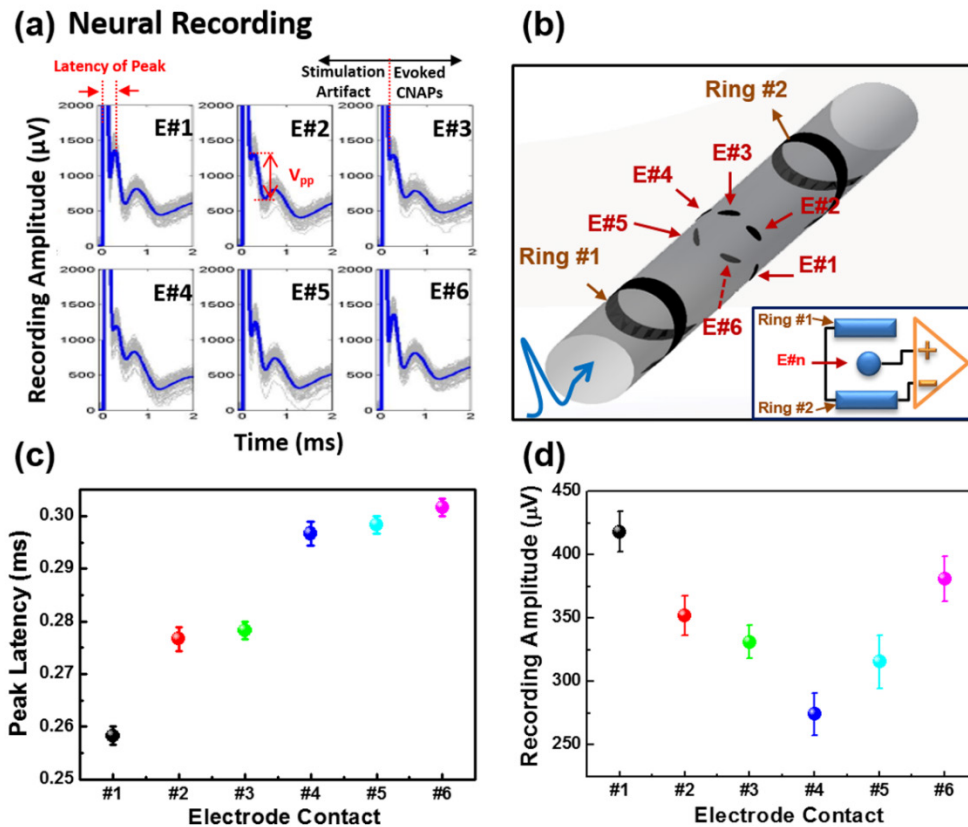


Figure 5.4 Results of selective recording on the rat sciatic nerve. (a) CNAPs recordings of six sensing electrodes on the main sciatic nerve elicited from electrical stimulation of the common peroneal nerve. (b) Schematic diagram of how the electrodes were positioned on the sciatic nerve and a mixed tripole configuration for the recording (inset). (c) The latency of the peaks with standard error under a stimulation current of 1.2 mA as a function of recording electrode contacts. (d) The mean recorded amplitude with standard error of CNAPs under a stimulation current of 1.2 mA as a function of the six sensing electrode contacts.

amplitudes on E#1 were the largest, while those of E#4 were the lowest. The results indicate that the location of the CP nerve inside the sciatic nerve was closer to E#1 than E#4. The maximum difference between E#1 and E#4 was 48% when stimulated with 0.4 mA. The difference decreased with increasing current amplitudes until 32% with 1.2 mA. The difference did not change beyond that. This may be due to the fact that the larger stimulation current amplitudes fully activated all the nerve fibers in the CP nerve. Our results demonstrated that all six recording electrodes positioned around the nerve were able to record CNAPs successfully.

5.4.2. Selective Stimulation on sciatic nerve

To investigate the ability of the sling electrodes to perform selective stimulation, we positioned the sling electrode around the sciatic nerve while recording CMAPs from the GM and TA muscles. The peak-to-peak amplitudes of the CMAPs were measured and normalized to the highest amplitude. The normalized CMAPs recorded from the GM and TA muscles were then plotted against the stimulation intensity, respectively. The difference between the normalized CMAPs recorded from GM and TA muscles (also known as selectivity) was also plotted against the stimulus intensity. As shown in **Figure 5.5a**, the difference in the activation of TA-GM on E#1 was 20.5% at 2.6 mA, indicating that the TA muscle was stimulated more than the GM muscle under this condition. The difference on E#3 was negligible, meaning that the GM and TM muscles were activated together across the different stimulation intensities (**Figure 5.5b**). The difference on E#5 was -14.3 to -16.9 % when stimulated with current amplitudes in the range of 2.2 to 2.4 mA, demonstrating that the

GM muscle was stimulated more than the TA muscles under this condition (**Figure 5.5c**). The results demonstrate that the TA muscle can be activated more strongly through E#1 than E#3 or #E5. This matches up with the recording results discussed earlier in that stimulation of the CP nerve (which controls the TA muscle [65]) resulted in the largest amplitudes on E#1. Thus, it is not surprising that stimulation on E#1 resulted in larger activation of the TA muscle.

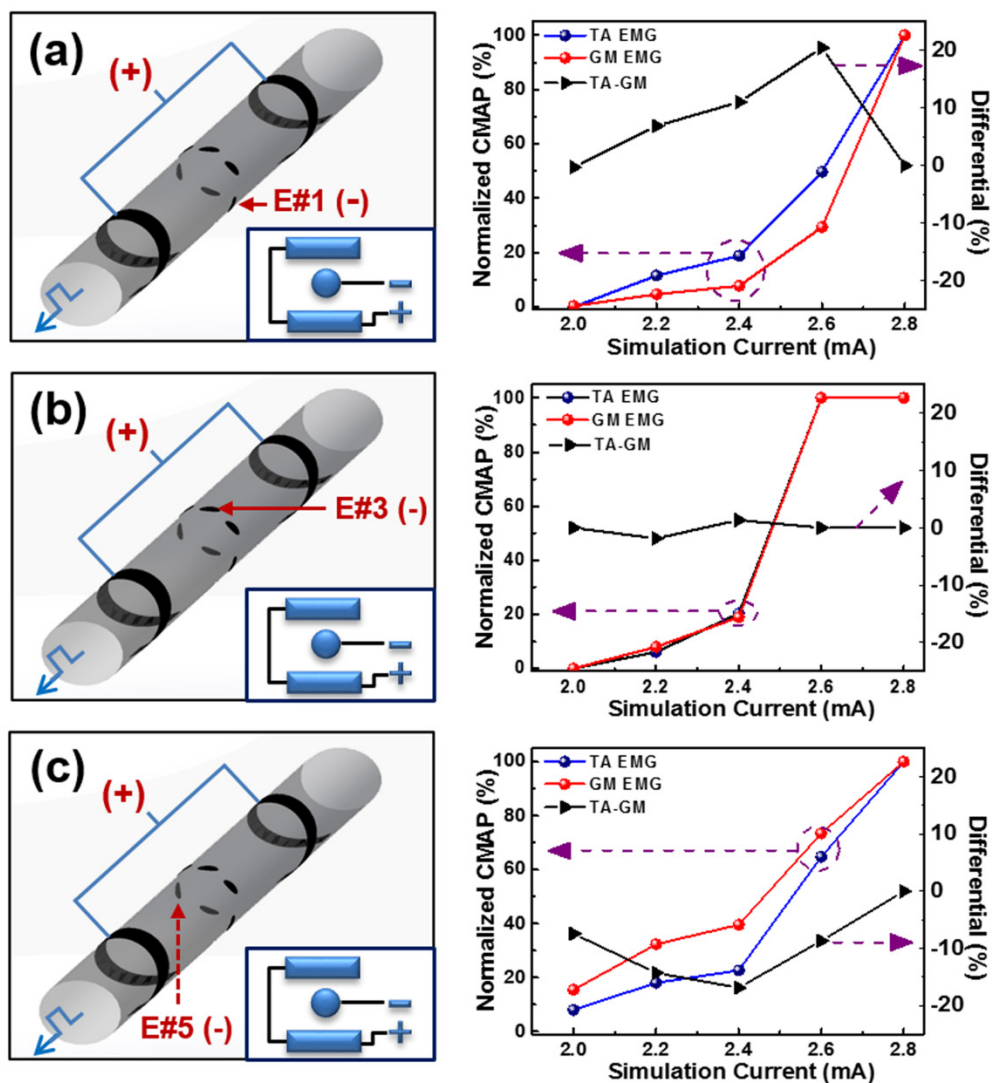


Figure 5.5 The results of selective stimulation on the rat sciatic nerve. Schematic diagram of selective stimulation using the longitudinal tripolar configuration (left, inset) on the sciatic nerve through (a) Channel #1, (b) Channel #3, and (c) Channel #5. The results of normalized CMAPs from the TA and GM with selectivity (right).

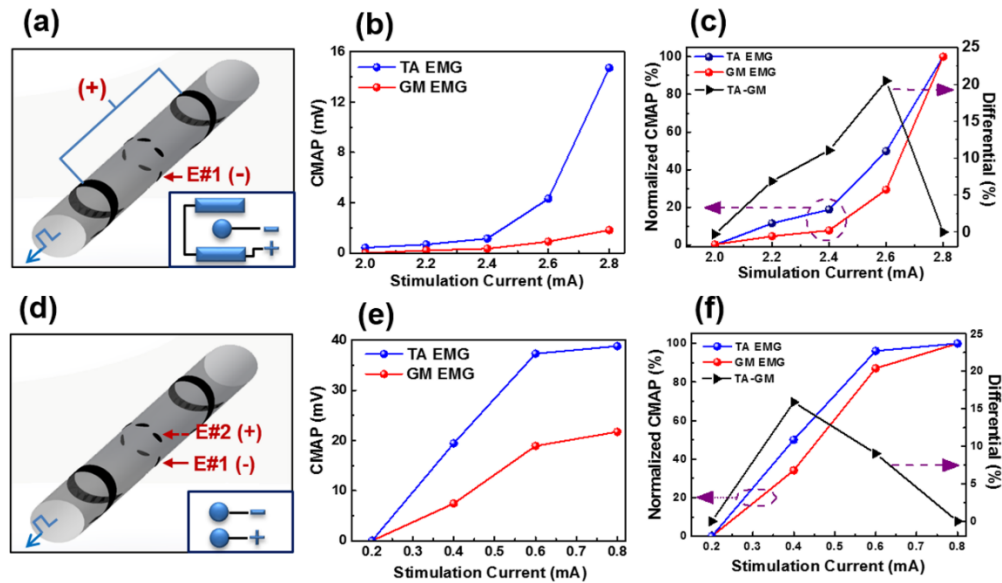


Figure 5.6 The results of selective stimulation on rat sciatic nerves depending on different configuration. (a) Schematic diagram of the longitudinal tripolar configuration, (b) CMAP, and (c) normalized CMAP with corresponding to selectivity depending on stimulation current. (d) Schematic diagram of the transverse configuration, (e) CMAP, and (f) normalized CMAP with corresponding to selectivity depending on stimulation current.

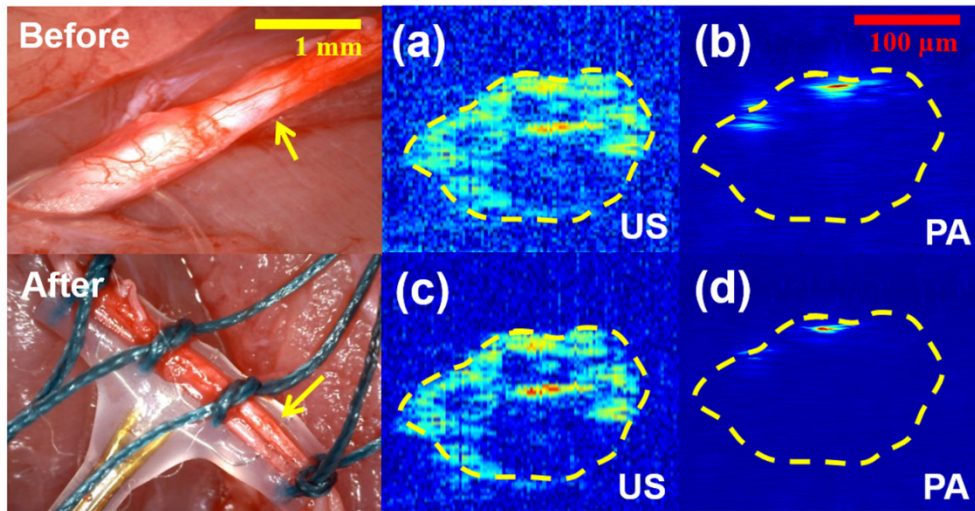
We also explored stimulation using the transverse configuration in order to compare with the longitudinal tripolar configuration for the sling electrodes. E#1 and E#2 were selected for the transverse stimulation since E#1 showed the highest selectivity (**Figure 5.6a,d**). The CMAPs measured from the GM and TA muscles are plotted against stimulation current amplitudes in **Figure 5.6b,e**. In addition, the normalized CMAPs from the GM and TA muscles, as well as the difference between the normalized CMAPs, are plotted against the stimulation current amplitudes in **Figure 5.6c,f**. One significant difference between the two configurations was the stimulation current required to activate the muscles. As shown in **Figure 5.6b,e**, the longitudinal tripolar configuration activated the muscles from 2.4 mA, while the transverse stimulation activated the muscles from 0.4 mA. Higher current amplitudes normally carry the risk of nerve

damage and delamination of electrodes. In addition, the transverse stimulation activated higher amplitudes of CMAPs than the longitudinal stimulation, which suggests that it may be able to generate more effective stimulation of the muscles. A previous study using multipolar cuff electrodes also showed similar results [112].

5.4.3. Hemodynamic measurement by functional photoacoustic microscopy (fPAM)

To verify whether the sling electrodes affect the hemodynamics of the sciatic nerve, we used functional photoacoustic microscopy (fPAM) to image the blood flow through the blood vessels on the nerve surface before and after implantation of the sling electrodes. We also imaged the blood flow after the implantation of a commercial cuff electrode (Microprobe Inc., Gaithersburg, MD, USA) (inner diameter: 0.75 mm). A custom-designed 50 MHz dark-field confocal fPAM system was used with an axial resolution of 32 μm and a lateral resolution of 61 μm (Acoustic Sensor Co., Ltd., Taiwan). For photoacoustic (PA) wave excitation, 570 nm (λ_{570}) visible wavelength laser pulses were employed to monitor the relative functional hemodynamic response changes [106, 113, 114]. The designed transducer had a -6 dB fractional bandwidth of 57.5%, a focal length of 9 mm, and a 6 mm active element. The incident laser energy density on the nerve surface was less than 6 mJ cm^{-2} , which is within the ANSI safety limit of 20 mJ cm^{-2} . The achievable penetration depth of the current fPAM setup was estimated to be 3 mm, with around 18 dB SNR [106]. It was defined as the ratio of the peak signal value to the root-mean-square value of

Cuff Electrode



Flexible Sling Electrode

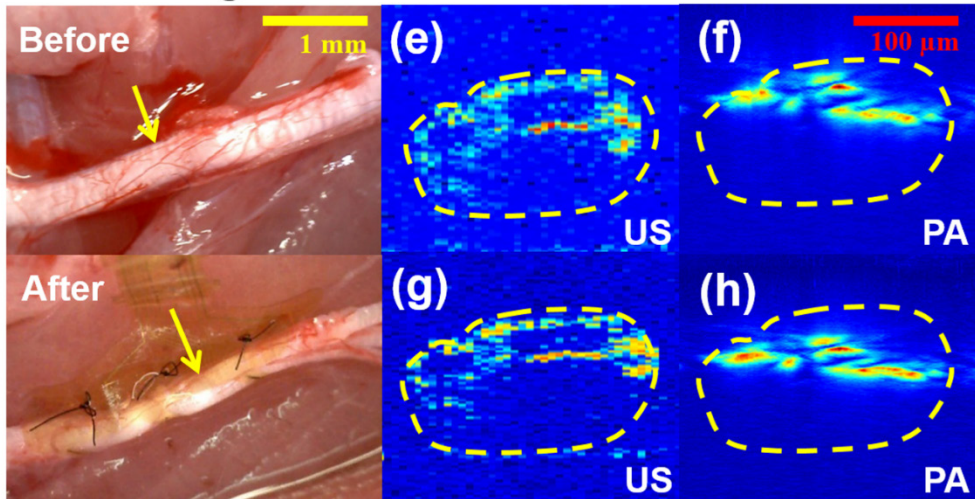


Figure 5.7 Picture of sciatic nerves before and after implantation of a commercial cuff and the sling electrode, respectively (Left). The results of functional photoacoustic measurements (Right). (a) US image of the targeted blood vessel and (b) in vivo IR(570) PA B-scan image reflected the blood volume changes before implantation. (c) US image and (d) in vivo IR(570) PA B-scan image of the same position after the implantation of the cuff electrode. (e) US image and (f) in vivo IR(570) PA B-scan image before implantation (g) US image and (h) in vivo IR(570) PA B-scan image after the implantation of the sling electrode.

the noise. No signal averaging was performed to capture real-time hemodynamic responses for functional imaging analysis.

These results are shown in **Figure 5.7**. The yellow arrows in the left panels

indicate the blood vessel cross-section direction of the photoacoustic (PA) B-scan images. Laser pulses at a visible wavelength of 570 nm (λ_{570}) was employed for PA wave excitation. These wavelengths were used because the detected PA signals at λ_{570} were dominated by changes in cerebral blood volume (CBV) and this reveals crucial information about the nerve hemodynamics [106]. The blood vessels were also identified in the PA B-scan image at λ_{570} , and all PA images and values were normalized to the maximum change in the $I_{R(570)}$ image. There was a significant reduction in the CBV (i.e., R_{CBV}) following cuff implantation (**Figure 5.7a-d**). However, there were no significant changes in the CBV values before and after sling implantation (**Figure 5.7e-h**). This indicates that the sling electrodes did not cause any changes in the blood flow in the nerve, while cuff electrodes can significantly exert changes in nerve hemodynamics.

5.5. Discussion

In this chapter, a flexible and adjustable sling interface was proposed and investigated for selective sciatic nerve recording and stimulation. Here is the summary and key features.

- The neural interface enabled helical implantation of active electrodes around a nerve with minimal pressure on the nerve, but still maintained good electrical contact with the nerve.
- The results of the selective recording demonstrated that compound neural action potentials (CNAPs) were clearly recorded from six sensing electrode contacts positioned around the nerve, with

different amplitudes and latencies. It indicated the location of the CP nerve inside the sciatic nerve, and provided a reasonable nerve conduction velocity (NCV) of the sciatic nerve.

- The results of the selective stimulation demonstrated that different muscle activation patterns of Gastrocnemius Medialis (GM) and Tibialis Anterior (TA) muscles were achieved using a longitudinal stimulation.
- In comparison, transverse stimulation evoked higher amplitudes in the compound muscle action potentials (CMAPs) than the longitudinal stimulation, which suggested that transverse stimulation may be able to provide more effective stimulation of the muscles.
- The results of blood flow measurements demonstrated that the pressure applied on the nerve by the neural interface was less than that applied by commercial cuff electrodes.

All results suggested that this design may be able to perform differential recording and selective stimulation with less long-term nerve damage, which could be effective in neuromodulation applications in the future.

CHAPTER 6. BATTERY-FREE NEURAL INTERFACE USING FLEXIBLE SLING ELECTRODE AND TRIBOELECTRIC NANOGENERATOR (TENG)

6.1. Motivation

Implantable bioelectronics have recently emerged as a powerful way to monitor biological signals and treat diseases such as pacemakers, deep brain stimulators, and neuromodulators [5, 6, 25]. The enormous progress attributed to the development of flexible/stretchable electronics, which enables the integration of various kinds of bio-sensors, actuators and energy storage elements, has opened up a new research field [43, 115-118]. Meanwhile, e-skin technology which can be used to craft soft and stretchable implantable/wearable medical devices, can also provide a better interface to the human organs, blood vessels and neural branches. By using these flexible implantable bioelectronics to achieve more sensitive and accurate bio-signal recording and stimulation, we have new ways of enabling bioelectronic medicine [39, 41, 42]. One of the critical challenges for long-term use of such devices is a reliable power source with reasonable output power. Some feasible solutions have been investigated including external energy sources, which are out of body and provides energy to the devices via wired [3] and wireless [36, 37, 119] communication, and implantable batteries that normally require recharging or replacement [120, 121]. The concept of scavenging human body energy into useful electrical power by various mechanisms has been explored as an alternative way to support operation of such bioelectronic implants. For example, thermal energy from the body heat by thermoelectric device [122-

126], mechanical energy from arterial dilation and contraction by piezoelectric device [127-130], and muscle contraction by electromagnetic device [131] have been reported. Among the devices of mechanical energy harvesting, triboelectric nanogenerators (TENGs) have recently been proposed as a promising technology [132-143]. The TENGs work on the principle of contact electrification [144-146] between two materials coupled with electrostatic induction providing advantages of lower cost, a wider range of material choice (flexible and biocompatible materials) [147-149], easy fabrication, and high output power by stacking of multiple layers [150, 151] as compared to other energy generators. Recently, some *in vivo* demonstrations of energy harvesting from heart beat [152-154] and muscle contraction [155] showed the possibility of using the TENGs as an implantable power source. Moreover, biodegradable TENGs were studied totally eliminating the concern of post-surgery for the extraction of the device [156]. Without looking into physiological basis and relationship between various muscle bundles and a sciatic nerve, X. S. Zhang et al. demonstrated strokes of a separated frog leg attached with a microneedle electrode array (MEA) on the sciatic nerve which was powered by a TENG [157]. Although the MEA used in this work is relatively invasive to nerve, and the design is not good for long-term use and selective stimulation for activation of different muscles in a control manner, it opens an attractive research direction of TENGs for direct stimulation of a peripheral nerve.

In this chapter, we investigated stacked TENGs as a potential source for neural stimulation. To achieve charges high enough for nerve stimulation, we characterized various parameters of the stacked TENGs, such as electrical connections, the number of stacked layers, and the confinement length.

Furthermore, we demonstrated direct stimulation of a sciatic nerve in rats using this novel battery-free neural interface combined the TENGs with the sling interface while monitoring muscle signals.

6.2. System Design

Figure 6.1 shows the schematic diagram of conceptual system using TENGs and neural interfaces for neuromodulation. The TENGs, driven by muscle movement from human body (**Figure 6.1a**), generate electrical energy and transfer the energy to a CP nerve or a sciatic nerve by neural interfaces (**Figure 6.1b-d**) to activate the TA muscle (**Figure 6.1e**).

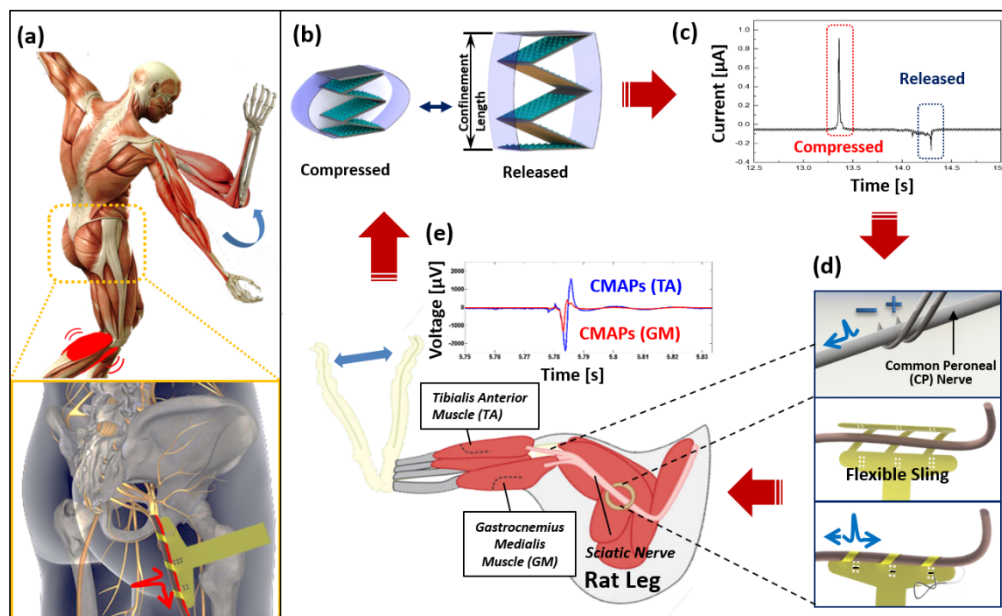


Figure 6.1 Schematic diagram of the conceptual system using flexible neural interfaces and triboelectric nanogenerators (TENGs). (a) Schematic diagram of the conceptual system using the sling interface and a TENG in human. (b) Schematic diagram of the TENG in a compressed state and a released state. (c) The generated current by the TENG. (d) Schematic diagram of the flexible and adjustable sling interface and (e) leg contraction with compound muscle action potential (CMAP) recordings of tibialis anterior (TA) and gastrocnemius medialis (GM) muscles.

Direct stimulation of low frequency, generated by the muscle movement, may benefit simple and natural activation of targeted muscles more than stimulation by the other external sources that require additional components (coils and circuits etc.) and complicated procedures.

6.3. Device Configuration and Working Mechanism

We deploy TENGs with multilayer stacked design to provide high current in experiments. For the fabrication of the device, inverted micropyramid patterns were prepared by anisotropic etching of silicon pits using KOH onto a silicon substrate. These micropyramid patterns were transferred onto PDMS films using molding process. These PDMS micropyramid structures improve the contact area between two layers and act as the first triboelectric layer for the charge generation process. For the mechanical support, a PET sheet is folded into zigzag shaped structure as shown in **Figure 6.2a**. This structure can provide both the space for assembly of the multilayer stacked TENG and the recovery force when the press is released. The stored elastic energy helps in reverting back to the original position to realize the contact separation mechanism between multiple stacked layers. After folding the PET into the zigzag shape, the Cu films are attached on two pairs of contact layers (**Figure 6.2b**). The PDMS layers with micro-pyramid patterns are assembled on the bottom Cu electrode for each pair of the layer (**Figure 6.2b**). After assembling the copper films, the patterned PDMS films are attached on top of each copper film, facing upwards (**Figure 6.2c**). To optimize confinement height, PET films with different lengths are applied to encompass the stacked TENG devices. The

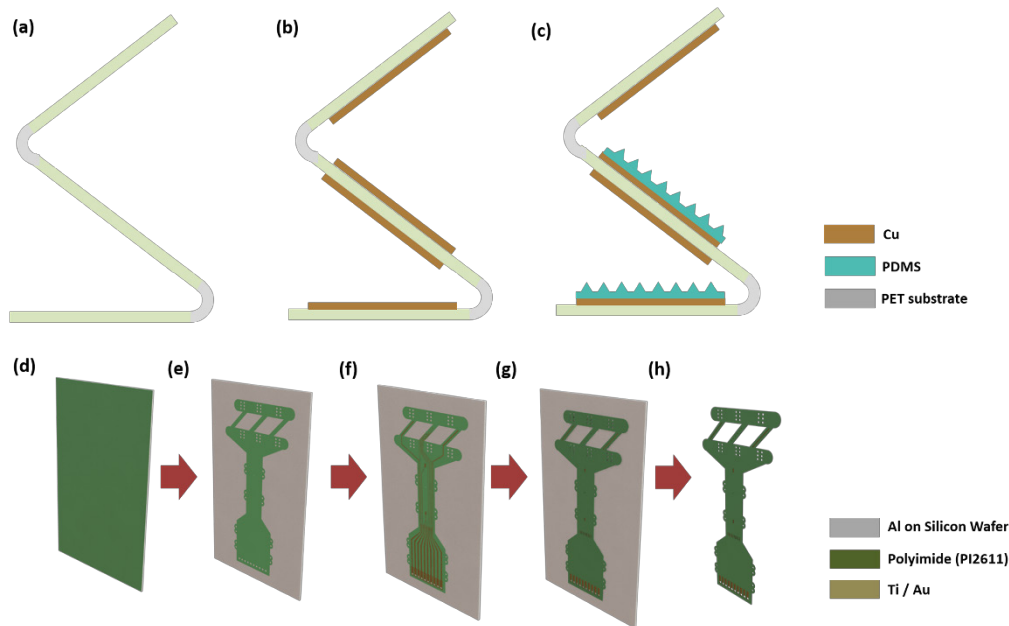


Figure 6.2 Fabrication procedure for triboelectric nanogenerator and flexible sling electrode (a) a PET substrate folded into zig-zag shape. (b) The folded PET substrate with copper electrodes attached. (c) The micro-patterned PDMS layers assembled on alternate copper electrodes for a pair of triboelectric layers. (d) The first layer of 6 μm polyimide on Al deposited silicon wafer. (e) The patterned first layer of polyimide. (f) The patterned metal layers of Ti (20 nm)/Au (300 nm). (g) The patterned second layer of polyimide. (h) The device is released from the substrate by electrochemical process.

fabrication process of the sling electrode has been described in the Chapter 5.

The working mechanism of the TENG is depicted in **Figure 6.3**. When the device is pressed, all layers contact with each other leading to triboelectric surface charge generation on the patterned PDMS and the top copper films (**Figure 6.3b**). After the force is removed, the potential increment at the top electrode with respect to the bottom electrode leads to current flow from the top electrode to the bottom electrode while releasing the device (**Figure 6.3c**). When the device is completely released, all the triboelectric layers reach in electrostatic equilibrium (**Figure 6.3d**). The reduction of the potential at the two electrodes drives the current flows in the opposite direction when the stacked

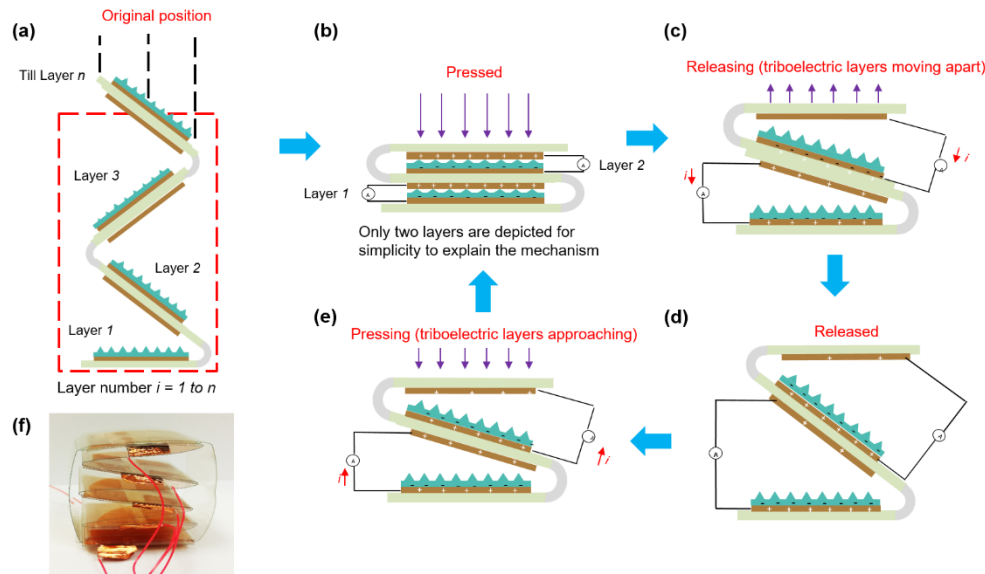


Figure 6.3 Schematic diagram of working mechanism of triboelectric nanogenerator (a) Device layers in the original position, (b) as the device is compressed using force, triboelectric layers come in contact, (c) triboelectric layers moving apart from each other as the force is released, (d) electrostatic equilibrium is reached at the extreme position resulting into no current between electrodes, (e) triboelectric layers approaching each other as external periodic force is applied on multiple stacked device. (f) A picture of the 5-layer device.

device is pressed again (**Figure 6.3e**). After the second contact, one cycle of the power generation is completed and another cycle continues. **Figure 6.3** shows a picture of the 5-layer device. The dimension of each TENG layer is 31 mm by 25 mm.

6.4. In vitro characterization of triboelectric nanogenerators (TENGs)

To study the effect of the stacked multiple layers on overall device performance, various parameters, such as electrical connections, the number of stacked layers, the frequency of applied force and the confinement length, were studied. Thereafter, we demonstrated biomechanical energy harvesting using human hand and heel strike for practical applications.

An oscilloscope (DSOX3034A, Agilent Technologies) with a probe (100 M Ω) was used to measure voltages of the device. For current measurements, low noise current preamplifier (SR570, Stanford Research Systems) was connected to the oscilloscope to measure the current in the form of voltage signal. The power characteristic measurement of the stacked TENGs was conducted by connecting load resistances in series across the device and measured the voltage across the resistor. The measured voltage was then used to calculate the power dissipation in the load resistor.

To demonstrate the configuration of electrical connection among the layers, we compared the output voltage and current of 5 stacked-layers connected in parallel and series, respectively. A probe with 100 M Ω load resistance was used for the voltage measurement. The voltage output is shown in **Figure 6.4a** and **Figure 6.4d** for the parallel and the series configurations, respectively. The voltage (connected the probe of 100 M Ω load resistance) of the parallel configuration was 68 V, which is slightly lower than that of the series configuration which was 76 V. The estimated open circuit voltage for series connection is 192.2V and for parallel connection is 76.8V. The connection in series can provide much higher open circuit voltage than that of connection in parallel. However, the short circuit currents of the parallel configuration was 1.9 μ A which is much higher than that of the series configuration, 0.8 μ A, as shown in **Figure 6.4b** and **Figure 6.4e**. This result indicates that the parallel electrical connection is suitable for improving higher current output whereas the device connected in series in same polarity leads to increase in peak output voltage. It is noticeable that the voltage signals of the series configuration are asymmetric showing that the positive peaks are much higher than the negatives peaks. This

phenomenon is induced by inner impedance change of the series configuration during the separation process of the layers. The positive peaks are generated when the device is fully compressed while the negative peaks are generated when all the triboelectric pairs separate from each other. During this separation process, the total inner impedance immediately becomes very large once the first pair separates, which is very close to open circuit. Then, the resistance of the probe become much smaller than the inner impedance and only a small portion of the voltage can be measured. That is why the negative peaks will be much smaller than the positive peaks. Whereas, for the parallel configuration, the total inner impedance of the device will not significantly increase until all the triboelectric pairs separate from each other. Thus the charge transfer process will not be affected greatly.

Thereafter, the voltage and power characteristics were measured depending on different values of load resistances. **Figure 6.4c** and **Figure 6.4f** show the power and voltage characteristics of the 5 layer stacked device. The peak power of the layers connected in the parallel was 51.8 μW at the load resistance of 15 $\text{M}\Omega$ (the 100 $\text{M}\Omega$ probe connect in parallel with measured load resistance of 13 $\text{M}\Omega$). For the layers connected in the series configuration, the maximum power was 59.8 μW at the load resistance of 239 $\text{M}\Omega$ (the 100 $\text{M}\Omega$ probe connect in parallel measured load resistance of 70.5 $\text{M}\Omega$). Even though the maximum powers of the two configurations show the similar level, the decrement of the maximum power in series configuration is significant when the load resistance value is reduced. It demonstrates that the parallel configuration is suitable for neural stimulation since the impedance between a sensing electrode of neural interfaces and a sciatic nerve is typically degree of $\text{k}\Omega$. We used the parallel

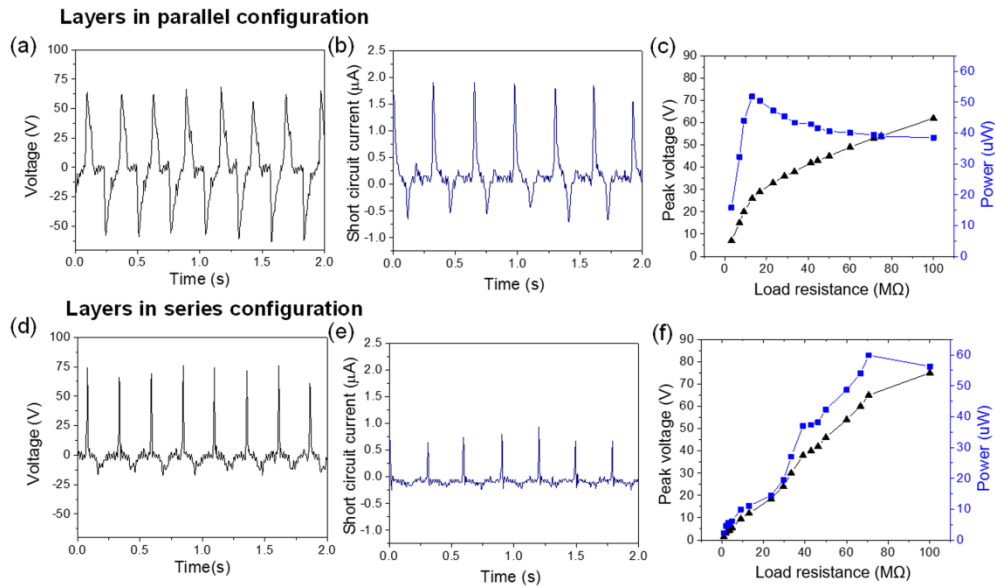


Figure 6.4 Effect of electrical connections on stacked device with 5 layers. (a) Output voltage, (b) short circuit current, and (c) voltage and power characteristics for layers connected in parallel configuration; (d) Output voltage (e) short circuit current and (f) voltage and power characteristics for layers connected in series configuration.

configuration for the rest of characterizations.

We demonstrated the effect of the number of layer, frequency, and confinement length to optimize the performance of the device. Firstly, we increased the number of stacked layers at a fixed frequency of 4 Hz and a fixed confinement of 4 cm to demonstrate corresponding change in the output voltage and short circuit current. The peak output voltage remains almost constant (**Figure 6.5a**) whereas the short circuit current increases linearly from 0.3 μA to 1.7 μA as the number of the layers increase from 1 to 5 (**Figure 6.5b**), respectively. Then the 5 layered multi-stacked device was tested at different frequency of the applied force at a confinement distance of 4 cm as shown in **Figure 6.5c** and **Figure 6.5d**. Both the voltage and the current increase proportionally to the frequency, which can be explained by the increased impact force as the frequency of applied force increases [158]. As for the equal level of

force, the surface charge generated is the same, the decrease in time interval between repeated impacts leads to higher output voltage and current. Since a larger separation distance results in higher triboelectric output, only characterizing the relation between the confinement length and triboelectric output is not very meaningful. Here we made a comparison between devices with 5 stacked layer and 15 stacked layer in the same condition to know how to achieve higher output with a fixed volume. The output voltage and current of 5 stacked layer and 15 stacked layer devices are shown in **Figure 6.5e** and **g**, respectively. It was observed that for smaller values of confinement lengths, both the peak output voltage and short circuit current increased but started saturating after a confinement length value of 3 cm for 5-layer device and 4 cm for 15-layer device, respectively. Compared with the 15-layer device, the 5-layer device had a slightly higher output voltage but a much lower current. The higher voltage of the 5-layer device can be attributed to the larger spacer assigned to each triboelectric pair when the total confinement length is the same for both the 5-layer device and the 15-layer device. Because the total output voltage is mainly determined by the output of an individual layer that is affected by the separation length. Then, we fixed the confinement length of 4 mm and force frequency of 2 Hz for both device and characterized the maximum output power and inner impedance. As can be seen in **Figure 6.5f** and **Figure 6.5h**, because of the parallel configuration, compared with the 5-layer device, the 15-layer device can provide a higher output power and much lower inner impedance while the output voltage at 100 M Ω load remains constant, which tallies with the theoretical model.

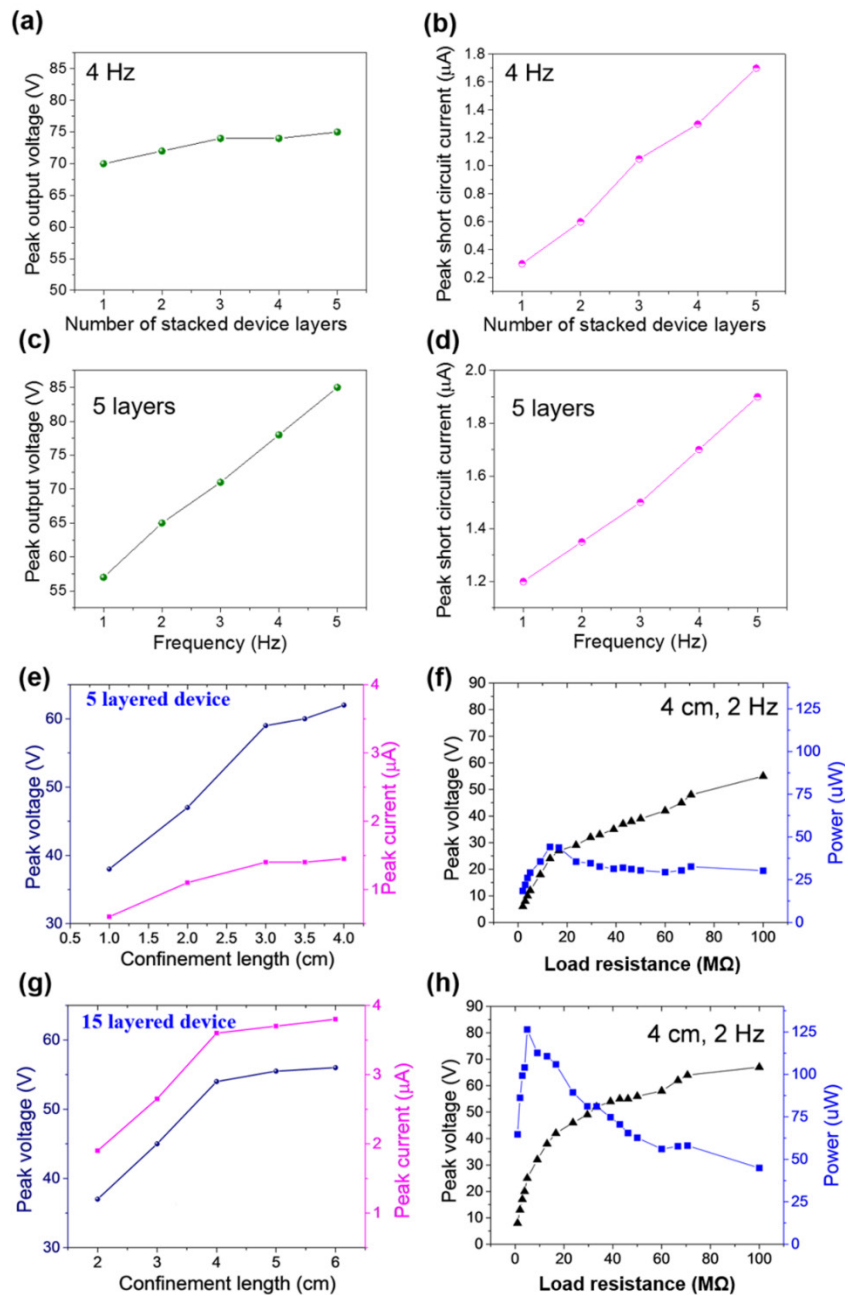


Figure 6.5 (a) Peak output voltage (measured with a100 MΩ probe) for different device layers at 4 Hz; (b) Peak short circuit current for different device layers at 4 Hz; (c) Peak output voltage (measured with a100 MΩ probe) for different frequencies for 5 layered device; (d) Peak short circuit current for different frequencies for 5 layered device; (e) Variation of peak voltage and short circuit current with different confinement lengths for 5 layered device; (f) Output voltage and power with different load resistance for 5 layered device with 4 cm confinement length at 2 Hz ;(g) Variation of peak voltage and short circuit current with different confinement lengths for 15 layered device; (h) Output voltage and power with different load resistance for 15 layered device with 4 cm confinement length at 2 Hz.

For theoretical analysis of series and parallel configuration, there are n layers stacked together in zigzag manner to improve the overall power output of the device. These n layers can be electrically connected in series or parallel configuration to maximize the power output in the load connected to the multiple stacked nanogenerator. Single device layer can be approximately modeled using a voltage source V_{OC} corresponding to the open circuit voltage generated by the device layer connected in series with an impedance Z due to internal device capacitance single device layer [159]. **Figure 6.6** shows the circuit diagram of n device layers connected in series with all the voltage sources in same polarity. The equivalent impedance of all the devices connected in series configuration can be given as nZ . The equivalent circuit for the device layers connected in series is depicted in **Figure 6.6** with nZ as the equivalent impedance connected with a voltage source of nV_{OC} in series. Z_L is the load impedance connected to the stacked device with layers connected in series. Using Kirchoff's circuit laws the current i_S in the circuit can be given by Eq. (4).

$$i_S = \frac{nV_{OC}}{nZ + Z_L} \quad (4)$$

Using the expression for i_S , the power dissipated in the load impedance is given by Eq. (5). The power dissipated in the load impedance is the useful power which is utilized from the generated energy by multilayer stacked TENG.

$$\text{Power dissipated in } Z_L = i_S^2 Z_L = \frac{V_{OC}^2}{\left(\frac{Z_L}{n} + Z\right)^2} Z_L \quad (5)$$

Similarly, the schematic diagram for the parallel configuration for the stacked device layers is shown in **Figure 6.6**. The equivalent circuit for this arrangement can then be given by using effective impedance Z/n connected with a voltage source V_{OC} . Z_L is the load impedance connected to the multilayer stacked TENG. The current in the equivalent circuit for parallel configuration can be given using the following expression:

$$i_P = \frac{V_{OC}}{Z_L + \frac{Z}{n}} \quad (6)$$

The power dissipated in the load impedance Z_L can be calculated using Eq. 7 similar to the case of series configuration.

$$\text{Power dissipated in } Z_L = i_P^2 Z_L = \frac{V_{OC}^2}{\left(Z_L + \frac{Z}{n}\right)^2} Z_L \quad (7)$$

According to the maximum power transfer theorem, at the point of impedance matching (load resistance value of nZ and Z/n for series and parallel connection, respectively), the power output generated by both series and parallel configuration is the same and equal to $nV_{OC}^2/(4Z)$. But for practical applications, typically the load impedance Z_L is significantly lower than the

internal impedance Z of a single device layer. This is due to the high values of internal impedance for triboelectric devices. Taking this fact into account, if we look closely at Eq. (5) and (7), it is clear that parallel configuration tends to improve the overall power output of the device for low value of load impedances due to better impedance matching. It is to be noted that for this discussion, we have assumed that all the device layers generated voltage output synchronously without any delay which might not be completely true in practical situations for multilayer TENG. The individual triboelectric device layers may not come in contact with each other at the same time resulting in some time difference between the peak output of the device layers.

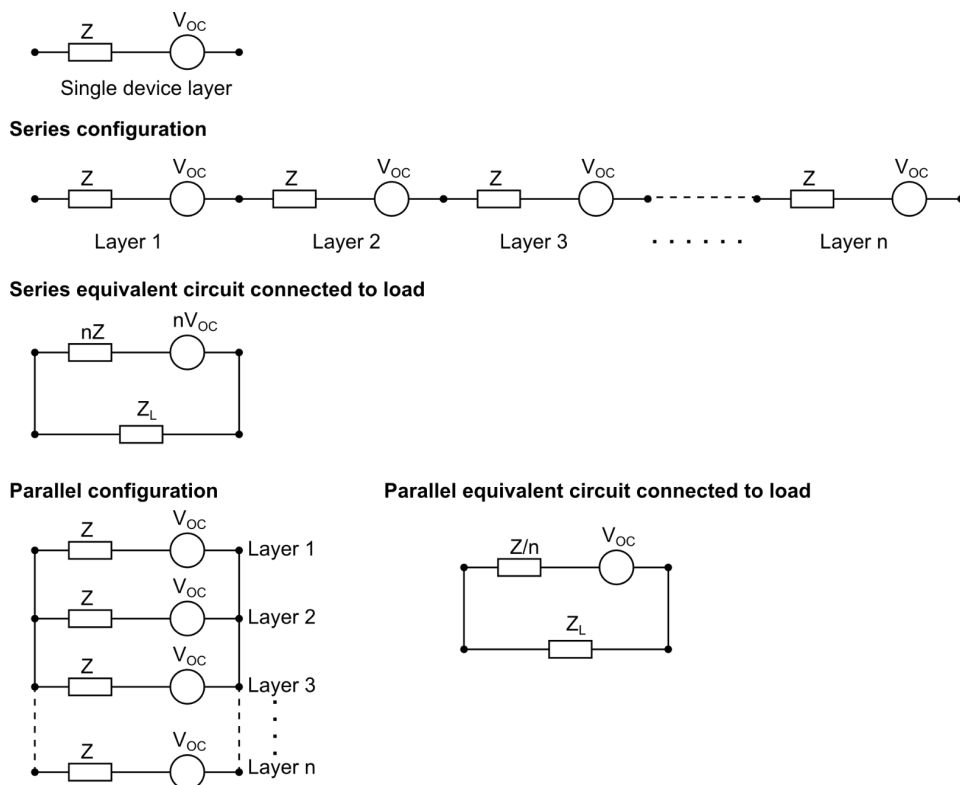


Figure 6.6 Electrical connections of device layers in series and parallel configuration

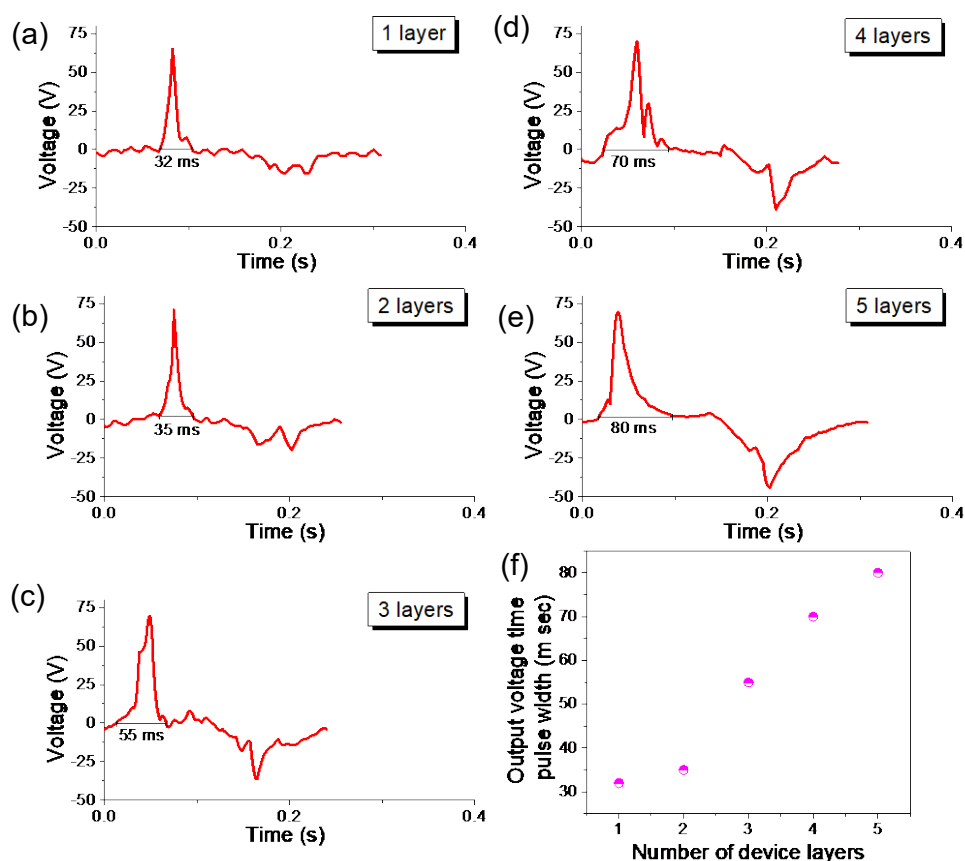


Figure 6.7 Broadening of the voltage time domain output due to multiple peaks from stacked design. Output voltage signal for (a) 1 layer (b) 2 layers (c) 3 layers (d) 4 layers (e) 5 layers. (f) Output voltage time pulse width increases as the number of the layer increase.

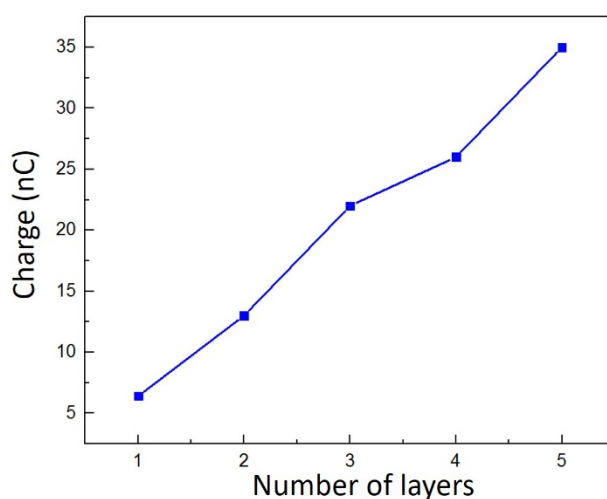


Figure 6.8 Charge generated by stacked TENGs as a result of the number of layers when to fully tap it by a hand.

One of the important issues for the multi-layered stacked devices is the synchronization of output generated from the different device layer. As the device is zigzag shaped, the device layers do not necessarily generate the output in synchronization with other device layers. But there is a degree of asynchronization between the device layers, the output voltage for every layer peaks at a different time which leads to broadening of time domain output voltage pulses. The time domain pulses are plotted in **Figure 6.7** for different number of device layers. The voltage output pulse width increases continuously with the number of layers stacked together. Although the peak voltage does not improve in the parallel configuration with increased number of stacked device layers, the pulse width increases from 32 ms for single layered device to 80 ms for the 5 layered device. The increase in pulse width can be partly attributed to the asynchronization between the output of different device layers. The increase in pulse width leads to higher average power for increased number of layer for stacked devices. Figure 6.8 shows calculated charges generated by the number of stacked layers. For the stimulation of nerve, charge, which is the product of current amplitude and pulse width, is important. Even though the TENG generates A few μA current, pulse width is around 30 - 80 ms. Therefore, the total charge is around 35 nC, which is a reasonable threshold charge for stimulating a nerve based on previous study [65].

To demonstrate practical applications of multiple layer stacked triboelectric nanogenerator, we tested the 5 layer stacked device using hand clapping and heel strike. For the experiments, we assembled a commercial accelerometer (ADXL325, Analog Devices, Inc., MA, USA) on the back of the palm during hand clapping and on the upper side of foot during heel strike. The output

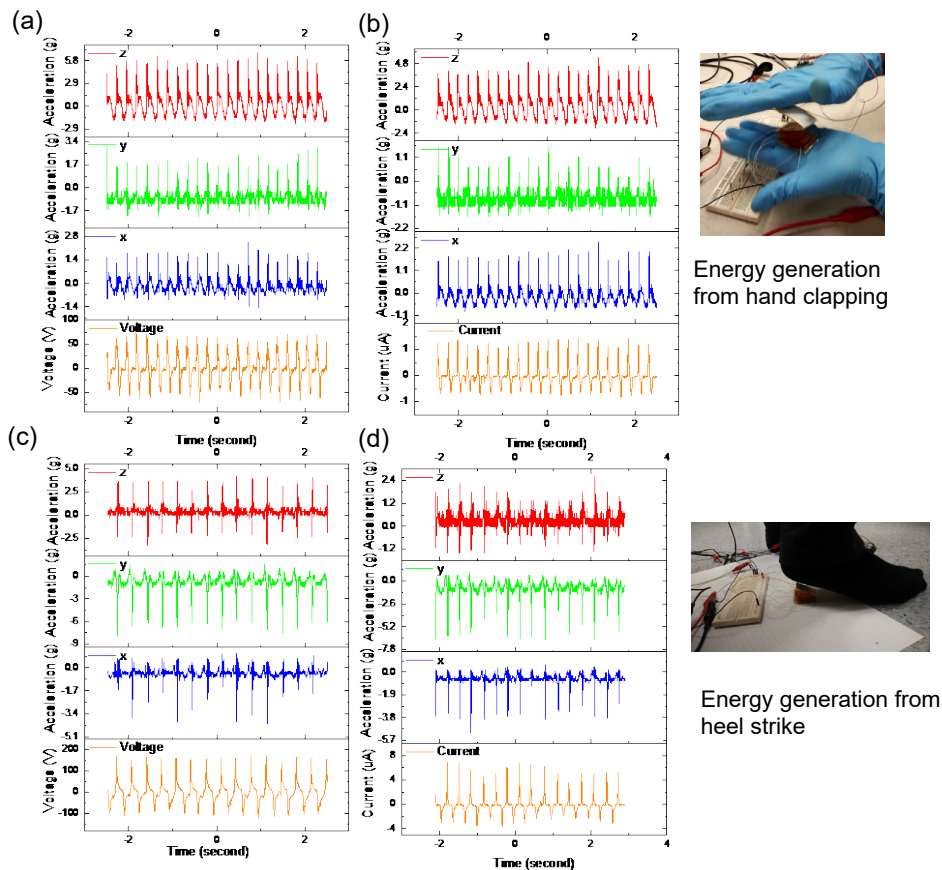


Figure 6.9 Demonstration of the energy harvester when assembled on human body. The results of (a) output voltage and (b) short circuit current generated by using clapping of hands. The results of (c) output voltage signal and (d) short circuit current generated by heel strike.

voltage and short circuit current results are plotted in **Figure 6.9a** and **Figure 6.9b** when the 5 layer stacked device is used to harvest energy from hand clapping. In **Figure 6.9**, real time acceleration data is also plotted in addition to the voltage and current output as the device is used to convert mechanical energy into electrical energy using triboelectric mechanism. Using hand clapping, a peak output voltage and current of 70 V and 1.4 µA was generated, respectively. Further, heel strike was used to harvest the mechanical energy using multilayer stacked TENG. The force of heel strike is around 600 N which is close to the weight of a normal people. This output is reasonable reported by

previous studies [150, 151]. The peak output voltage and current were measured to be 160 V and 6.7 μ A, respectively as the 5 layered stacked devices generated electrical from heel strike. The force provided by the heel strike is higher compared to the hand due to higher mass associated with the heel strike which results into significantly higher output using heel strike.

6.5. In vivo test of triboelectric nanogenerators and neural interface

To demonstrate a battery-free neural interface, we conducted selective stimulation to activate the TA muscle using the sling interface connected with the TENG. The sling interface was implanted on the sciatic nerve and two active electrodes were selected for the transverse configuration which enabled to activate the TA muscle more than the GM muscle. The TENG was then connected to the two electrodes of the sling interface (**Figure 6.10a**). The TENG was fully tapped by a hand to activate the TA muscle. In **Figure 6.10b**, the recorded CMAPs of GM (red) and TA (blue) muscles show that the TA muscle was activated more effectively than the GA muscle. We observed the twitch of the muscle, however, the muscle contraction was not strong enough for the ankle dorsiflexion. This may be due to fact that the charge was higher than the threshold of the muscle activation, but was not enough for the complete contraction of the TA muscle.

To fully demonstrate modulation of the TA muscle, we connected the TENG to a pair of Pt/Ir wires, i.e., stimulation electrode, and implanted on the CP nerve (**Figure 6.10c**). The TENG was tapped by a hand with different frequencies while the CMAPs of GM and TA muscles were recorded.

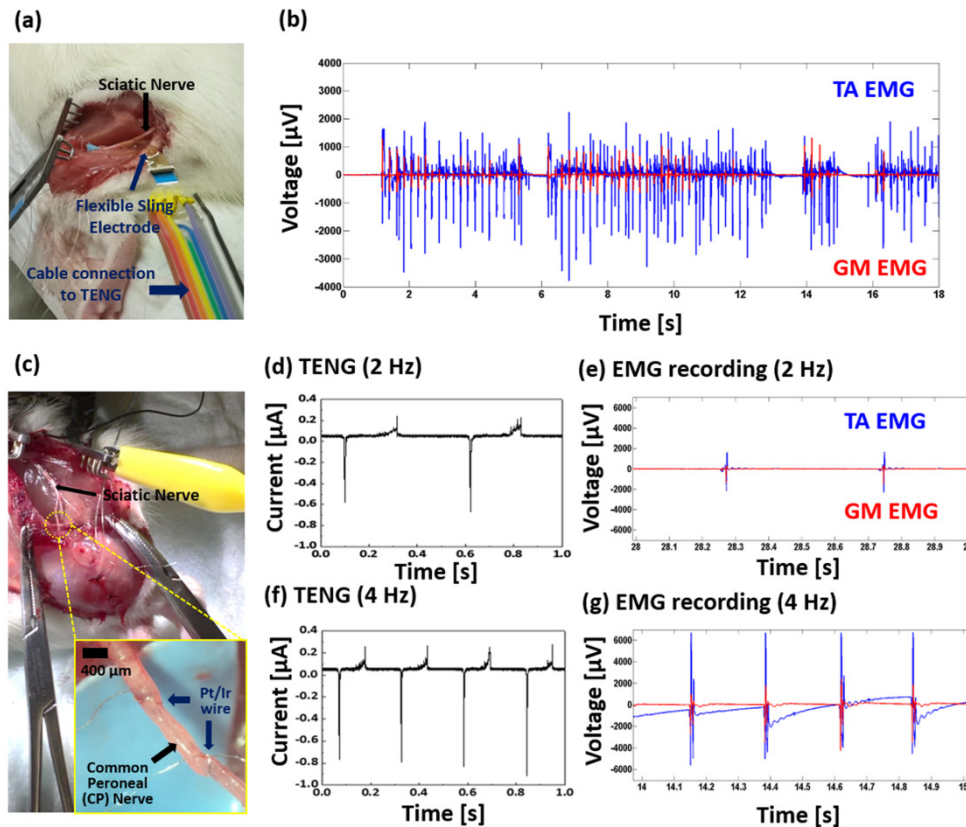


Figure 6.10 Picture of in vivo direct stimulation test using the sling interface and the TENG as direct stimulation source. (b) The recorded compound muscle action potentials (CMAPs) of GM (Red) and TA (blue) muscles by the battery-free sling interface. (c) Picture of in vivo direct TENG stimulation test using a pair of Pt/Ir wires on common peroneal (CP) nerve (inset). (d) Current peaks generated by the TENG and (e) the CMAPs recordings at 2 Hz. (f) Current peaks generated by the TENG and (g) the CMAPs recordings at 4 Hz.

As expected, the TA muscle was activated more than the GA muscle while stimulating the CP nerve. It is not surprising that a CP nerve innervates TA muscle more than GM as we discussed above. We observed the muscle twitch and contraction and it became strong when we tapped with higher frequency on the device. The activation via the CP nerve was more effective than the activation via the sciatic nerve by the sling electrode. This is because that approaching small nerves enhances the specific of evoking muscle signals [160].

We tracked the recorded CMAPs depending on frequencies to verify our

observation. **Figure 6.10d** shows current peaks generated by the TENG and **Figure 6.10e** shows the EMG recording at 2 Hz. The amplitude of CMAPs from the TA muscle was 1932.6 μV and that from the GM muscles of 834.5 μV . **Figure 6. 10f** and g show current peaks generated by the TENG and the EMG recording, respectively, at 4 Hz. The amplitude of CMAPs from the TA muscle was 6164 μV and that from the GM muscles of was 1720.3 μV . This is because, by using the hand tapping approach, the actual impact force on the TENG increases as the tapping frequency due to the nature of human hand behavior. The increased impact force associated with higher tapping frequency leads to higher output voltage. Thereby the muscles are activated more in this case. It demonstrates that the TENG is able to generate enough charge to control a TA muscle through a direct common peroneal nerve stimulation.

6.6. Discussion

We demonstrated battery-free neural interface as an advanced version of neural interface using the flexible sling electrode and triboelectric nanogenerators (TENGs). Stacked TENGs were optimized and demonstrated as a neural stimulator converting human body energy into feasible electrical power. The parallel configuration generated higher current and the generated pulse width increased as the number of stack layers increased. In addition, high frequency and high power input generate high output power. Finally, the optimized TENGs generated the charge around 35 nC by tapping fingers, which is enough for stimulating nerves [160].

To achieve direction stimulation using a battery-free neutral electrode, the

sling interface was implanted on a sciatic nerve, and two active electrodes were selectively connected to the optimized TENG based on the previous experiment for selective activation of the TA muscle. By tapping finger to the device, TA muscles were selectively activated more than GM muscles. Furthermore, we demonstrated stimulation of the CP nerve using the TENGs combined with a pair of Pt/Ir wires to control a TA muscle. The degree of activation of the muscle was controlled by the operation of the device.

For the first time, we achieved direct stimulation of a sciatic nerve and a branch nerve in alive animals using the TENGs connected with neural interfaces. Although this chapter showed the demonstration using a prototype of TENGs and the sling interface, other neural electrodes designs including the FLESE and split ring electrode can be combined with advanced TENGs using wearable platform or biocompatible encapsulation [46]. These advanced battery-free neural interfaces either wearable or implantable platforms would be used for clinical applications in the future.

CHAPTER 7. NOVEL FLEXIBLE CLIP (FNC) INTERFACE FOR NEUROMODULATION OF SMALL PERIPHERAL NERVES TOWARD BIOELECTRONIC MEDICINE

7.1. Motivation

Modulation of nerve signals using implantable bioelectronics has recently been recognized as a potentially powerful way to modulate body conditions or treat pathological conditions. More recently, it has been proposed that electrical impulses sent via visceral nerves may be used to regulate dysfunctional organs so as to restore physiological homeostasis [5-7]. For this, neural interfacing technology (NIT), which provides the basis for direct communication with neuron tissues and mapping neural signals, is an essential area to be preferentially developed among principal research areas in bioelectronic medicine [45]. Even though new extraneural approaches with flexible materials have recently shown promising results for peripheral nerve modulation [27-32], those are limited in surgical implantation on small visceral nerves due to its small size and the narrow space with movement in the viscera.

To achieve NIT for bioelectronic medicine, new paradigm-shift approach must be adapted and miniaturized enough to interrogate visceral nerves wirelessly and securely [45]. Here are grand challenges due to many physiological and anatomical difficulties in accessing deep nerves associated with the autonomic nervous system. These challenges include i) for the autonomic nervous system, complex innervation of the organs or muscles, rendering precise control of specific functions challenging; ii) quick and

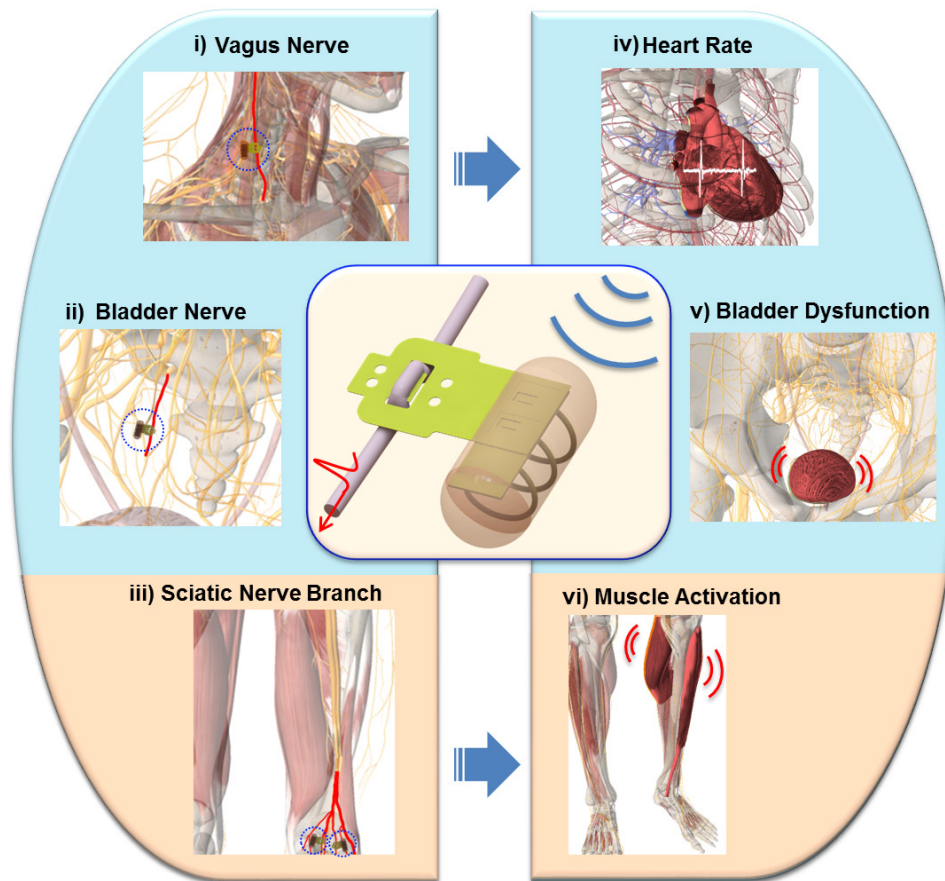


Figure 7.1 Schematic diagram of different applications of a wireless flexible neural clip (FNC) interface for wireless modulation of nerves to achieve different organ or tissue output. (i) Vagus nerve stimulation (VNS), (ii) bladder nerve stimulation, and (iii) the stimulation of sciatic nerve branches for modulation of (iv) heart rate (HR), (v) bladder dysfunction, and (vi) leg muscles, respectively.

mechanically secure implantation which is an important consideration in the presence of physiological motion such as respiratory and cardiovascular movements; and iii) considerable compliance and flexibility from the neural interfaces since nerves are highly compliant and associated with moving organs. Additionally, the integration of NIT with wireless powering by either ultrasound[34] or electromagnetic powers[35-37] is a promising direction for future bioelectronic medicine.

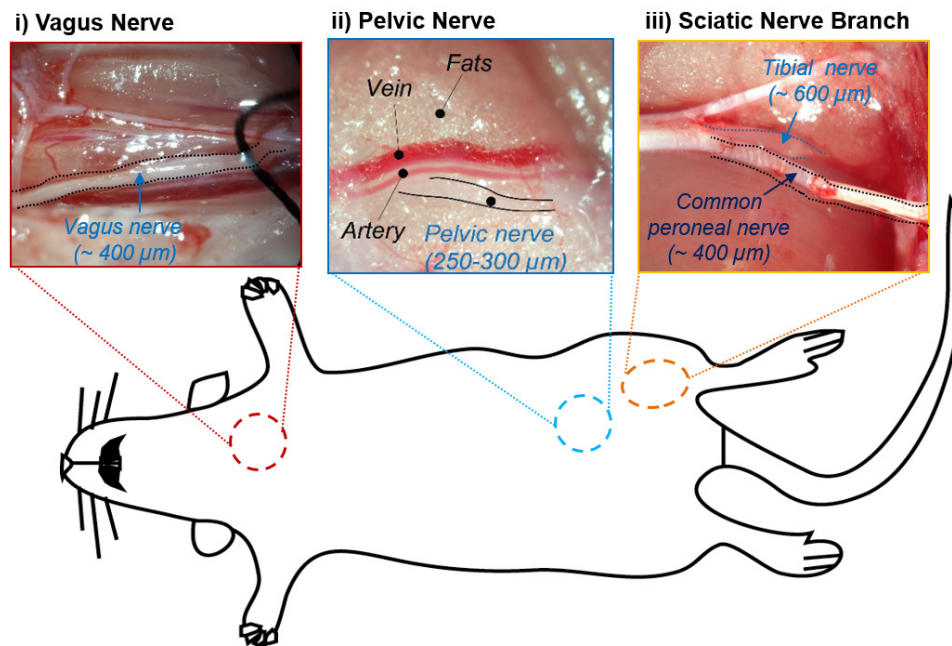


Figure 7.2 Photomicrographs of small peripheral nerves in rats; (i) a vagus nerve, (ii) a pelvic nerve, and (iii) sciatic nerve branches.

Here, we demonstrate a novel flexible neural clip (FNC) interface that enables reliable and easy implantation on different peripheral nerves to modulate different functions (**Figure 7.1**). We used the FNC to stimulate sciatic nerve branches, vagus nerves, and pelvic nerves to evaluate the feasibility of the design in modulating the function of each of these nerves (**Figure 7.2**). Furthermore, wireless pelvic nerve stimulation was performed using an integrated wireless FNC to demonstrate it as a new platform for implantable bioelectronics.

7.2. Interface Design

Novel clip design allows easy and reliable implantation on a small nerve in a manner analogous to clipping a paper clip. The FNC can be implanted onto a

peripheral nerve easily by inserting the nerve between the clip-strip and clip-springs after slightly bending the clip-springs (**Figure 7.3a**). This implantation has great benefit when it is implanted in small nerves located inside body in narrow and deep spaces accompanying continuous movement such as respiration and heartbeat. Furthermore, the FNC provides not only conformal contact with the nerve, but also gentle pressure on the nerve to keep the clip interface in place. The FNC is created based on the design of a paper clip that provides easy and secure implantation. The flexible and biocompatible polyimide serves as a scaffold of the FNC for the functions. The key element of FNC interface is the dimension of clip (length, width, and thickness of clip-springs, clip-strip, and clip-cavities) considering Young's modulus of the polyimide of 2.3G Pa [30]. The thickness of the device is largely tradeoff between flexibility and rigidity of the polyimide. To reliably perform clipping and conformal contact to a nerve, the total thickness of 16 μm was experimentally selected. Based on mechanical stress test of clip opening, the acceptable angle (α) between the clip-strip and the clip-spring was around 33~34° for reliable and repetitive opening function. The clip-strip width was taken the radius of nerves into account keeping the angle (Figure 7.4a). As shown in Figure 7.4b, one direction of gentle pressure is applied to three parts of the nerve. There is no compressive pressure thanks to this unique structure so that it allows gentle pressure to a nerve enough to clip the nerve while still making good contact.

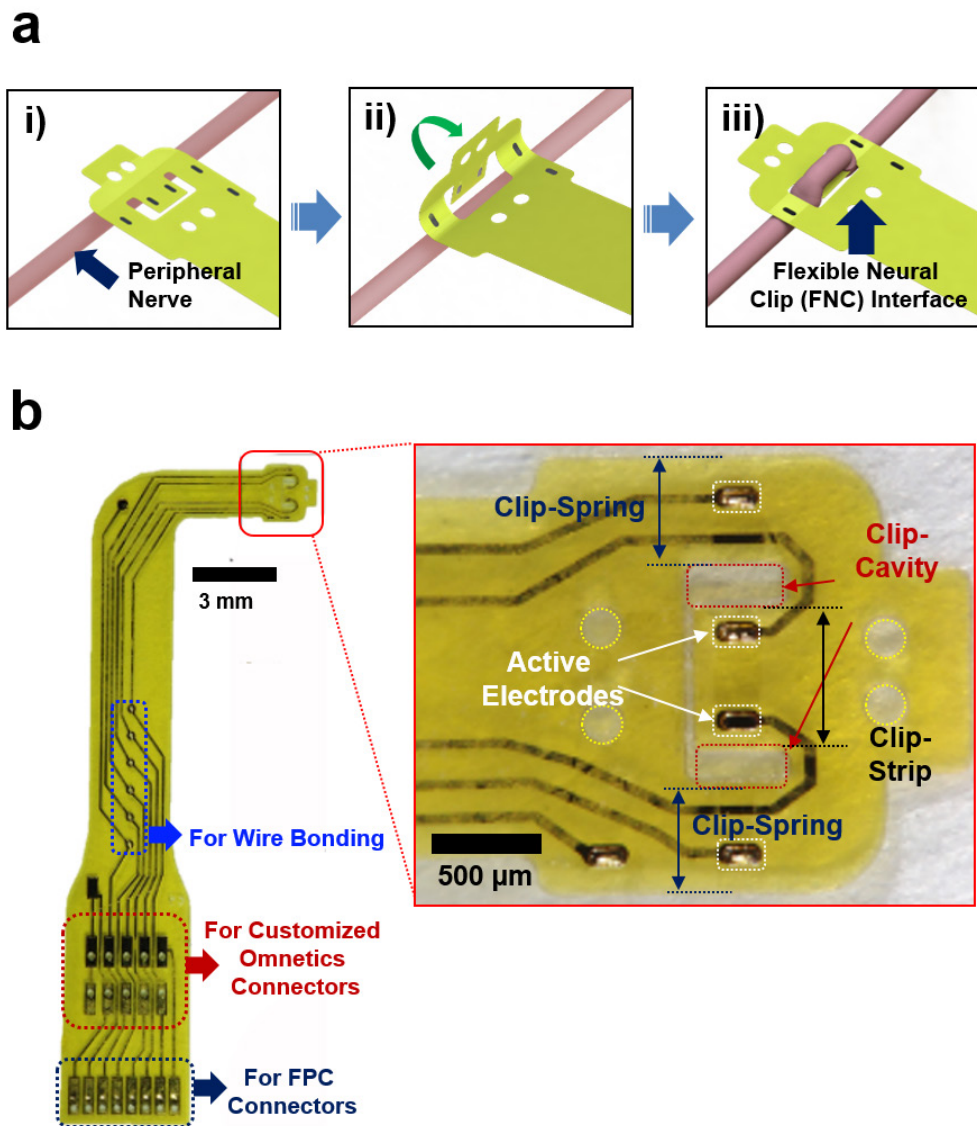


Figure 7.3 (a) Schematic diagram of implanting a flexible neural clip (FNC) interface in a peripheral nerve. (b) Picture of fabricated FNC and configuration.

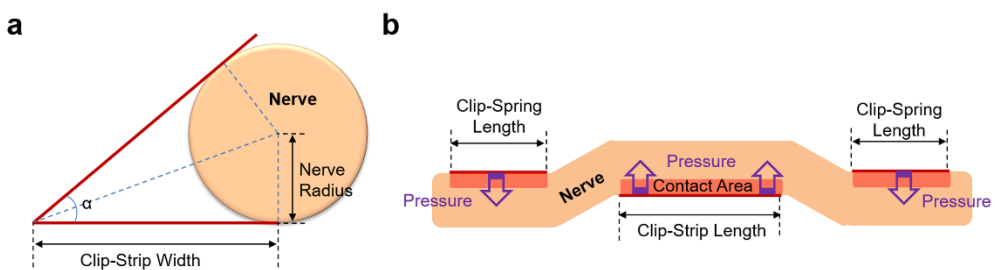


Figure 7.4 (a) Schematic diagram of opening clip head for implantation of a nerve. (b) Schematic diagram of cross-section view after the implantation.

The size of the clip-cavity for CP nerves and vagus nerves (diameter: $\sim 400 \mu\text{m}$) is $700 \mu\text{m} \times 500 \mu\text{m}$ and the clip strip is $650 \mu\text{m} \times 900 \mu\text{m}$. The width of clip-spring is the same as the length of cavity ($700 \mu\text{m}$) to maintain the spring elasticity of the polyimide. Two active electrodes (each $17672 \mu\text{m}^2$) are located on the center of the clip-strip with the distance of $350 \mu\text{m}$ for reliable position and stimulation of the implanted nerve. This FNC is able to cover bigger (diameter: $\sim 600 \mu\text{m}$) or smaller sizes (diameter: $\sim 300 \mu\text{m}$) of nerves thank to the functionality of the clip design during acute *in vivo* test. We also demonstrate a miniature FNC interface for pelvic nerves (diameter: $200\sim 250 \mu\text{m}$). The size of the clip-cavity is $470 \mu\text{m} \times 200 \mu\text{m}$ and the clip strip is $420 \mu\text{m} \times 650 \mu\text{m}$. The width of clip-spring is also the same as the length of cavity ($470 \mu\text{m}$). Each size of two active electrodes is $13024 \mu\text{m}^2$ and the distance between of the electrodes is $400 \mu\text{m}$. This design allows reliable implantation and stimulation of pelvic nerves in rats. Biocompatible and flexible polyimide material is used for the body of the interface.

7.3. Methods

7.3.1. Device fabrication

The flexible neural clip (FNC) interface consisted of a polyimide-Au-polyimide sandwiched structure. The fabrication process follows standard photolithographic and clean room procedures. Firstly, a $1 \mu\text{m}$ thick aluminum (Al) layer was evaporated onto the silicon substrate by physical vapor deposition. It acted as a sacrificial layer to release the final device from the substrate. Then a $8 \mu\text{m}$ base layer of photosensitive polyimide (Durimide 7505, Fujifilm, Japan) was spun onto the Al coated substrate. After exposure under

ultraviolet (UV) light, the base layer was post-baked and developed. The base polyimide layer was cured at 200 °C in N₂ for 0.5 hour. After applying the AZ onto the polyimide base layer, this layer was exposed and the electrode traces were patterned. A layer of 20 nm chrome (Cr) was deposited to improve the adhesion of the next conduction layer by sputtering. After a 250 nm gold layer was deposited, the conductive metal layer was patterned by a lift-off process in acetone. Another 8 μm top layer of polyimide was spun onto the processed metal layer, and patterned to expose the sensing contacts and connection pads. Then, we adopted an anodic metal dissolution approach to release the whole device that not only ensured a flat planar structure was released, but also was significantly faster than the traditional wet etching process. After the entire Al sacrificial layer was removed after 2 hours, the final device was released. The pads of the electrodes connected to FPC connectors (Hirose Electric Co. Ltd.) in a similar manner to a previous study for electrical connection [29]. To enhance electrical stimulation, exposed Au electrodes were then electroplated with iridium oxide. The detailed fabrication is described in Appendix 1.

7.3.2. Iridium oxide coating

Electrochemical interface is of paramount importance for stimulation. High electrode impedances will require high voltages to inject desired current amplitudes, which results in undesirable electrochemical reactions, possibly damaging both the electrode and the tissue. If the charge delivery capacity is poor, high current amplitudes will be required for the activation of the nerve, which may also cause nerve damage or delamination of the electrode surface [103].

Iridium oxide is widely used due to its good stability and large charge storage capacity (CSC) for neural recording and stimulation. Among three typical fabrication methods; sputtering iridium oxide film (SIROF), activated oxide film (AIROF), and electrodeposited iridium oxide film (EIROF), EIROF shows the largest CSC and lowest impedance [161]. Adherent electrodeposited films are most easily obtained on Au substrate compared with other noble metals such as Pt and PtIr.[162] To enhance electrochemical characteristics of stimulation, the released electrodes were coated with EIROF.

The electroplating solution was prepared in the following way, which was a modification of a recipe from the literature [161-163]: 300 mg of iridium chloride was dissolved in 200 ml of DI water, and stirred for 15 minutes. Then, 1000 mg of oxalic acid powder was added to the solution, and stirred for 10 minutes. Potassium carbonate was slowly added to the solution to adjust the pH to 10.5. The prepared solution was kept at room temperature for 2 days. When it turned into a violet color, it was stored in a dark bottle at 4 °C in the fridge. To electroplate the electrode sites with iridium oxide, a three-electrode configuration with a silver/silver chloride (Ag/AgCl) electrode, and mesh Pt electrodes for the reference and counter electrodes, was used for initial coating. A triangular voltage pattern of 0.55 V was applied 50 times by a potentiostat (Zennium E, ZAHNER-elektrik Inc, Germany). Thereafter, the electrode pads were connected to the negative terminal of an external voltage source, and the positive terminal of the external voltage source was connected to a platinum mesh electrode immersed in the solution together. Pulsed voltage, with peak-to-peak magnitude of 0.55 V and offset voltage of 0.275 V at 1 Hz was applied for 20 minutes to electroplate the iridium oxide.

7.3.3. Electrochemical characterization

To characterize electrochemical performance of the coated electrodes, electrochemical impedance spectroscopy (EIS) for measuring impedance, as well as cyclic voltammetry (CV) for measuring charge storage capacity (CSC), were carried out using a three-electrode setup in phosphate buffered saline (PBS). A three-electrode configuration with a silver/silver chloride (Ag/AgCl) electrode, and mesh Pt electrodes for the reference and counter electrodes, was used for both measurements. The output impedance was recorded with an impedance analyzer (Zennium E, ZAHNER-elektrik Inc, Germany).

The coated IrO₂ on Au sensing electrodes showed a good impedance value ($1.9 \pm 0.09 \text{ k}\Omega$ at 1 kHz, $n=10$) (**Figure 7.5a**), and a cathodic charge storage capacity ($56.4 \pm 2.42 \text{ mC/cm}^2$, $n=10$) (**Figure 7.5b**) for the stimulation [105, 161, 162]. These values are comparable or even better to materials used previously in the literature for neural stimulation [105, 161, 162]. These results demonstrate that the IrO₂ coated electrodes can be used for *in vivo* stimulation experiments.

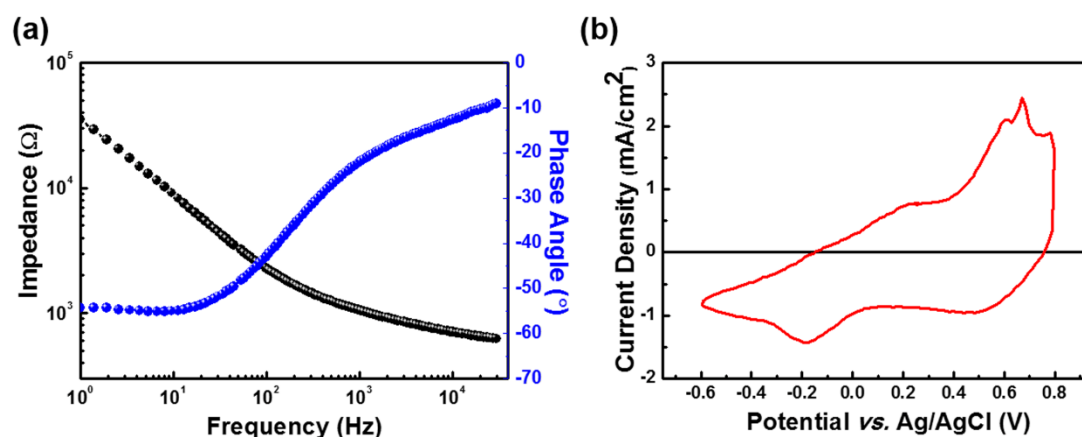


Figure 7.5 The results of electrochemical characterization of iridium oxide coated electrodes for a) impedance, phase angle, and b) cyclic voltammetry.

7.3.4. Physiological Characterization of bladder functions

Bladder pressure and urine output were also measured and detected during the stimulation to quantify the functional output. The FNC, which was connected to a stimulator (AM systems 2100) via a FPC connector, was positioned over the nerve using micromanipulators, and ‘opened’ manually using tweezers for the iridium-oxide coated leads to interface with the nerve at either short or long inter-active lead distances. Stimulation parameters were biphasic rectangular waveforms, with a frequency of 10 Hz, 150 μ s phase width, duration of 5 seconds, and amplitudes ranging from 25 to 200 μ A. Intra-bladder pressure was measured via a saline-filled catheter (Instech Laboratories Inc), inserted into the bladder that was connected to a pressure sensor (Transpac® IV). An infusion pump for refilling the bladder was used when necessary. A pair of wires (part of a voltage divider circuit) was placed outside the urethral meatus to detect voiding or urine outflow. A data acquisition board (PicoScope® 4424) was used to acquire amplified pressure signals, sync pulses from the stimulator, and voltage changes from the urine detection wires at a sampling frequency of 20 KHz. All acquired data were then analyzed using custom MATLAB programs. Pressure data were low-pass filtered at 30 Hz, and a 5 second period prior to each electrical stimulation was taken as baseline to calculate changes in pressure.

7.3.5. Wireless Flexible Neural Clip.

This wireless FNC (70 mg) consisted of a receiving coil, a rectifier, and an LED. For the preparation of wireless FNC, active version of FNC was fabricated

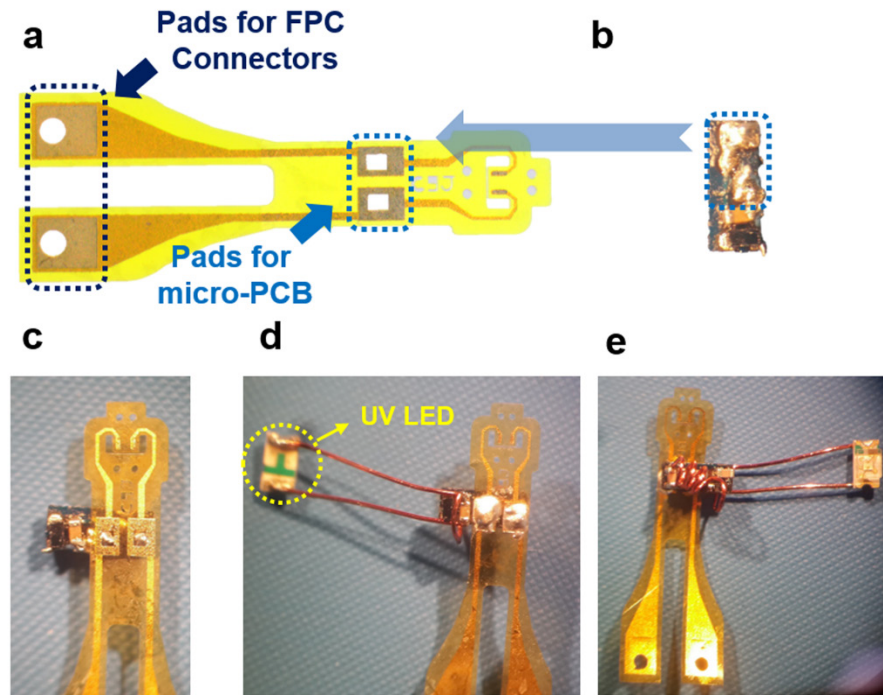


Figure 7.6 Photomicrograph of a) fabricated active FNC and b) micro-PCB soldered with active components. c) After aligning the FNC on the PCB then, d) conductive epoxy was applied and cured. e) The UV LED and coil were soldered and encapsulated with Kwiksil.

in the same manner of the fabrication procedure where contact pads matched with the size of mini-PCB (**Figure 7.6a**). Secondly, wireless components including diodes and capacitors were soldered on the PCB (**Figure 7.6b**). All of them were constructed on a Gold Phoenix printed circuit board (PCB). For the rectifier circuit, two Schottky diodes (Skyworks SMS7630-061) and two 10-pF capacitors were arranged in a one stage rectifier configuration, in which the output voltage is twice the input peak voltage. The FNC was aligned on the PCB, then, silver paste was applied for electrical connections (**Figure 7.6c**). A LED (Bivar, SM0603UV-400) was placed after the rectifier to ensure a constant 2.8v voltage necessary to drive the electrode. The LED was intentionally soldered and extended outside of the wireless FNC to monitor the operation of the device

and wireless stimulation (**Figure 7.6d**). The coil was wound on top of the PCB with an inner diameter of 2 mm using copper wire (Belden, 36-gauge magnet wire, 200 μm diameter), with 3 turns depending on the design frequency ($\sim 1.6\text{GHz}$). The entire FNC was encapsulated in a silicone elastomer (World Precision Instruments, Kwik-Sil Adhesive) except the sensor tips of the electrode. The power used to operate the device was around $\sim 0.1\text{ mW}$.

7.2. Stimulation of sciatic nerve branch for muscle activation

Firstly, we stimulated various sciatic nerve branches: the common peroneal (CP) nerve, tibial nerve, and sural nerve in rats while recording compound muscle action potentials (CMAPs) from the gastrocnemius muscle (GC) and the tibialis anterior (TA) muscles. Even though the sciatic nerve is not a visceral nerve, the size of the smaller branches is comparable to visceral nerves, so it was a good initial test of the FNC. In addition, the specificity of the sciatic nerve branches (i.e. the CP nerve primarily innervates muscles that control ankle dorsiflexion [160] while the tibial nerve mainly activates the GC muscle for ankle extension [65]) makes them ideal for demonstrating the function of the FNC. **Figure 7.7a** shows a schematic diagram of a rat and photomicrographs of the implanted FNC on the CP nerve, the tibial nerve, and the sural nerve, respectively. For electrical stimulation of neural tissue, stimulus amplitude and duration are critical parameters for reliable stimulation. These parameters also directly affect charge- and power-efficiency [164]. Current amplitude (I) and pulse width (PW) are important factors not only for stimulating nerves with respect to charge-efficiency (Charge is the product of I and PW for a rectangular pulse), but for energy-efficiency when to deliver it via wire or wireless from

stimulators to a nerve. The threshold stimulus current amplitude (I_{th}) decreases as the PW increases based on the following equation (8) [164],

$$I_{th} = I_{rh} \left(1 + \frac{T_{ch}}{PW} \right) \quad (8)$$

, where I_{rh} is the rheobase current and T_{ch} is the chronaxie. Short pulses minimize the charge required for excitation, but long pulse minimize threshold stimulus power since instantaneous power is proportional to the square of I (Equation 9). The energy (E) of a rectangular current pulse is the product of its power (P) and PW [164].

$$P = I^2 \cdot R \quad (9)$$

$$E = I^2 \cdot R \cdot PW \quad (10)$$

, where R is the electrode impedance.

Therefore, minimizing energy is analogous to finding the best compromise between charge- and power-efficiencies. It indicates that the most energy-efficient stimulation is when pulse width is equal to the chronaxie of the nerve. An implantable pulse generator will last the longest under this condition [164].

To optimize the energy efficiency, we sought to determine the chronaxie (T_{ch}), which is the shortest pulse width at a current amplitude that is twice the rheobase current (I_{rh})[164]. We measured the threshold current needed to evoke a visible ankle movement as a function of pulse width for the CP nerve and the tibial nerve (**Figure 7.7b**). The biphasic pulse widths were varied between 20 to 1000 μ s. The I_{rh} of the CP nerve was 4 μ A, and the calculated T_{ch} from the curve was 470 μ s. For the tibial nerve, the I_{rh} was 8 μ A, and the T_{ch} was 180 μ s. After that, we demonstrated the CP nerve and tibial nerve stimulation using pulse widths close to their respective T_{ch} , (CP nerve: 500 μ s; tibial nerve: 170 μ s) but at

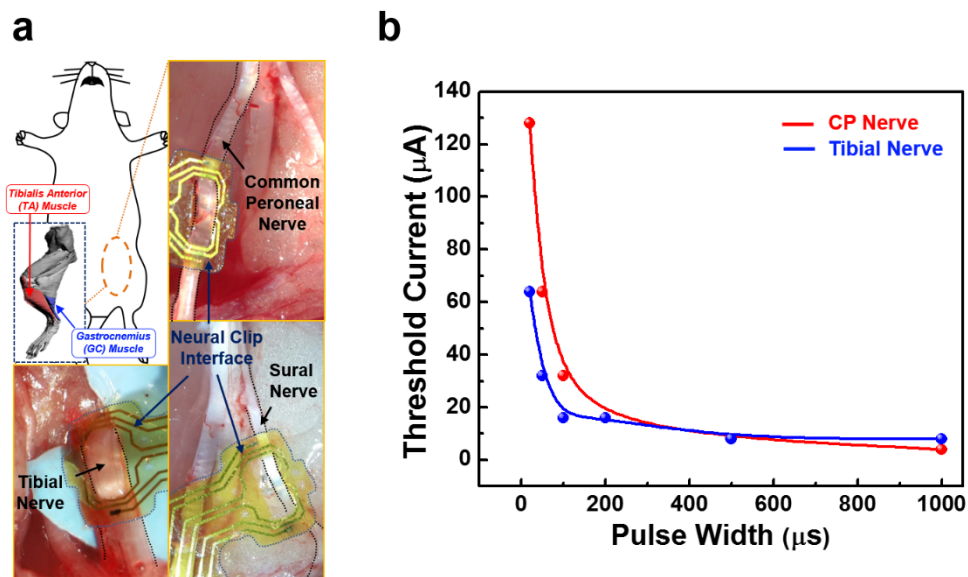


Figure 7.7 Sciatic branch nerve stimulation to control muscles. (a) Schematic diagram and photomicrographs of sciatic nerve branches. (b) Threshold currents versus pulse widths when stimulating the common peroneal (CP) and tibial nerves.

current amplitudes higher than the respective thresholds (**Figure 7.8a**). The TA muscle was activated more than the GC muscle during CP nerve stimulation, and ankle dorsiflexion was clearly observed. During tibial nerve stimulation, the GC muscle was activated more than the TA muscle, and ankle extension (plantar-flexion) with leg stretch visible. To verify whether the muscle activation was a result of the nerve stimulation, we applied lidocaine, which is normally used for blocking nerve function [102], to the CP nerve and conducted the same stimulation procedure again after 10 minutes. **Figure 7.8b** shows CMAP recordings of the TA and the GC muscles after CP nerve stimulation before and after applying lidocaine. After 10 minutes, the CP nerve was blocked completely, and no stimulation-evoked EMG signals were observed. We also attempted stimulation of the sural nerve. However, only small twitches of the middle toe in the rat were observed, with no clear muscle activation in the EMGs

of the TA and the GC muscles. This result is consistent with previous literature showing that the sural nerve mainly includes sensory fibers instead of motor fibers that activate the muscle [165]. These results demonstrate that the FNC can be used on sciatic nerve branches with different sizes, and consequently can be used to evoke different patterns of muscle activation.

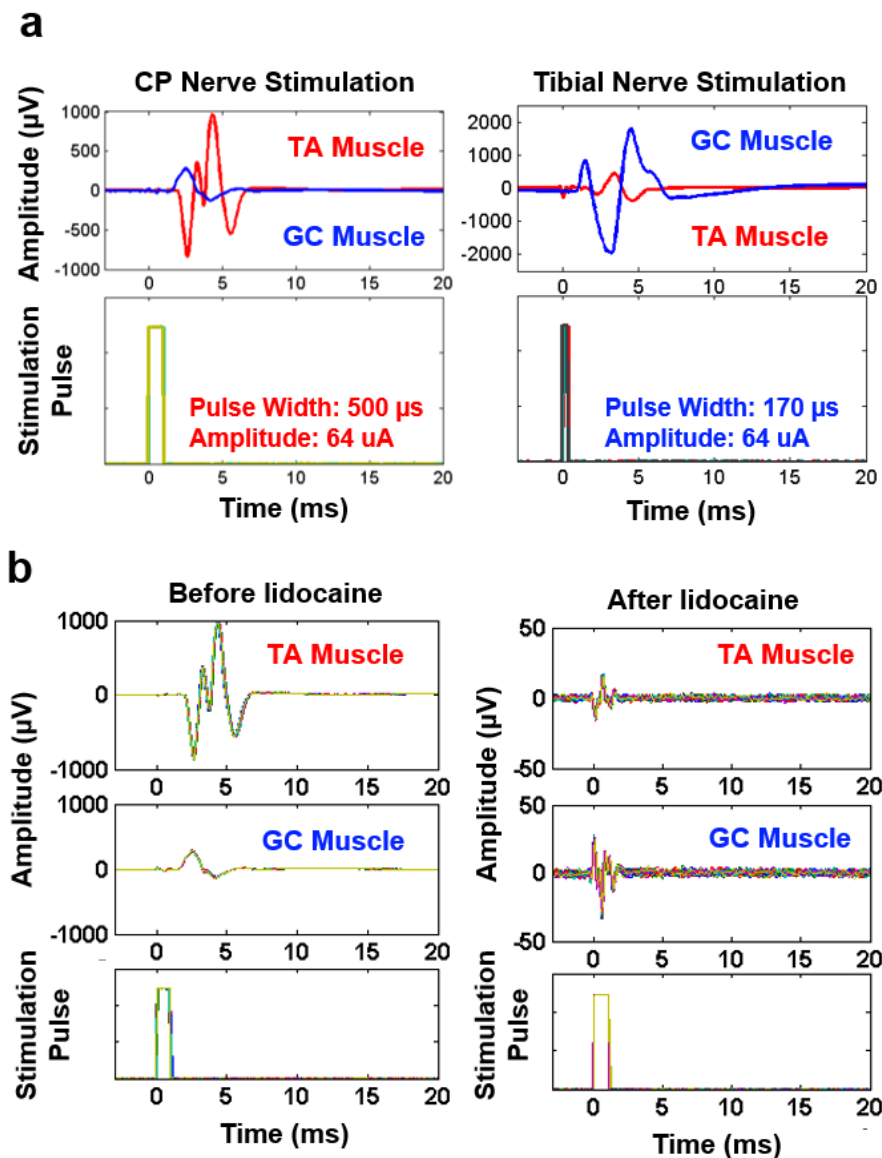


Figure 7.8 (a) The recorded EMG signals and stimulation pulses of the CP and tibial nerve stimulation. (b) The recorded EMG signals and stimulation pulses of the CP nerve stimulation before lidocaine application (left panel) and after lidocaine application (right panel).

7.3. Stimulation of vagus nerve for controlling heart rate

The Food and Drug Administration (FDA) approved vagus nerve stimulation (VNS) as an adjunctive, non-pharmacological therapy for patients with medically refractory partial onset seizures in 1997, as well as an adjunctive long-term therapy for chronic or recurrent major depression in 2005 [78, 166, 167]. Furthermore, VNS has shown other clinical benefits in diseases such as hypertension and rheumatoid arthritis [25, 168, 169]. Recently, VNS has been proposed as a promising therapeutic approach such as heart failure (HF) [72, 170, 171] and cardiac arrhythmia [172, 173] as it provides cardiac autonomic responses such as chronotropic, inotropic and dromotropic effects [73, 74, 168, 174]. For the clinical applications, several VNS factors such as pulse width, current amplitude, number of pulses, interpulse period, and electrode configurations still need to be verified with the physiological effects, though the therapeutic effect has been recognized in pre-clinical and pilot clinical studies [74]. While helical or cuff-type electrodes are commonly used for larger sized vagus nerves [25, 71], implanting these electrodes on smaller nerves are still challenging due to the cylindrical shape and encircling mechanism for good electrode-nerve contact. This is a technical challenge that has to be addressed especially for chronic epilepsy studies of common small animal models such as mice and rats [175, 176].

In this study, we demonstrated that the FNC, with its flatter profile and clip mechanism for achieving contact with nerves, is a novel way to interface with the vagus nerve in rodents. We performed VNS in rats using the FNC to control heart rate (HR) while monitoring the electrocardiogram (ECG) (**Figure 7.9a**). The FNC was implanted easily on the vagus nerve (**Figure 7.9b**), despite the continuous movement of the nerve due to respiration and heartbeats. First, we conducted preliminary tests with a range of stimulation amplitudes and pulse widths derived from a previous study [168].

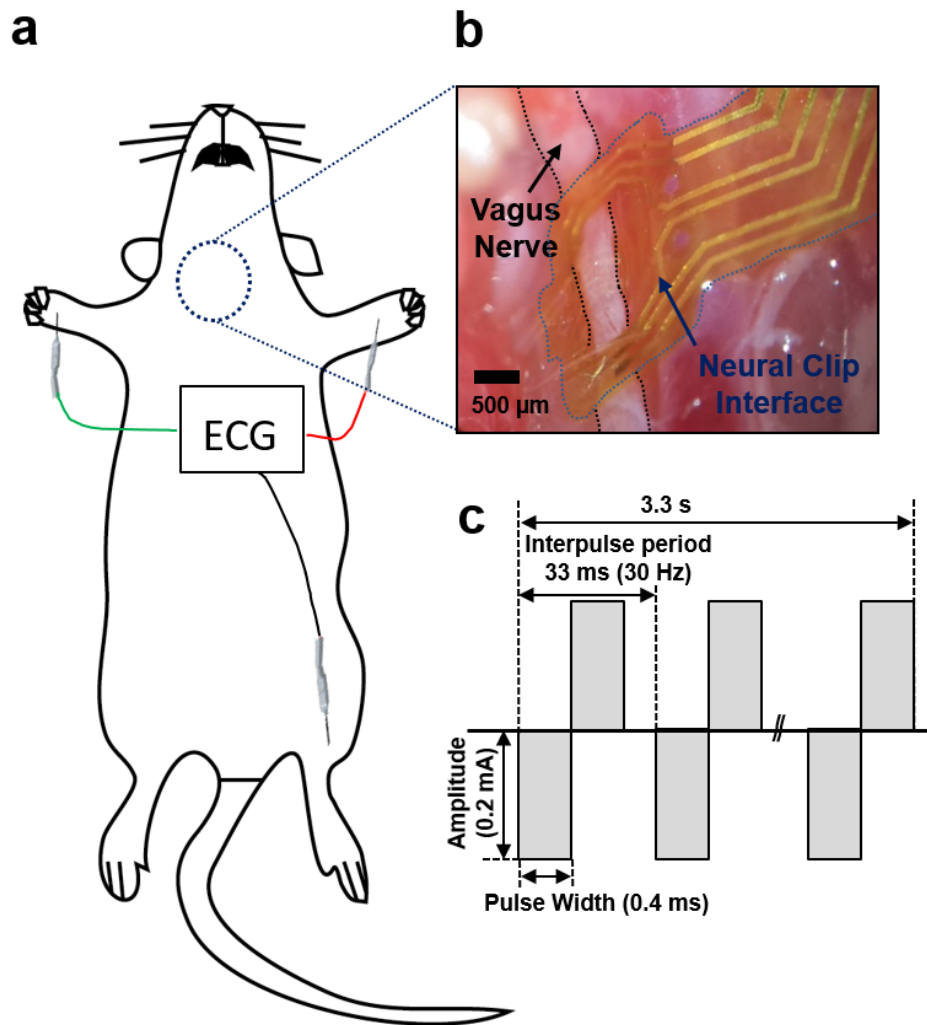


Figure 7.9 a) Schematic diagram of vagus nerve stimulation (VNS) for the control of heart rate (HR). b) A photomicrograph of an implanted flexible neural clip (FNC) on a vagus nerve in a rat. c) Schematic diagram of biphasic pulses for the stimulation.

Afterward, we repeated VNS with one parameter in multiple rats ($n=3$) with the parameter (30 Hz, pulse width of 0.4 ms, duration of 3.3 s, and amplitude of 0.2 mA) (Figure 7.9c). The HR was calculated by inter-beat interval (RR interval) which represent chronotropic effect [74]. The HR was significantly reduced during the stimulation, and recovered to baseline after the stimulation (Figure 7.10a). The mean reduction in the HR was 25.5 % during the stimulation, and the HR recovered to 99.8% ($n=17$) of the HR before stimulation when it was measured at 10 minutes after the

stimulation was stopped (**Figure 7.10b**). The results indicate that the HR changes are comparable or slightly more effective than previous studies [168, 177] within the safety range of the stimulation parameter, though it cannot directly be compared with other studies due to complex stimulation parameters and experimental conditions. The efficacy of our small FNC in visceral vagus neuromodulation was proved.

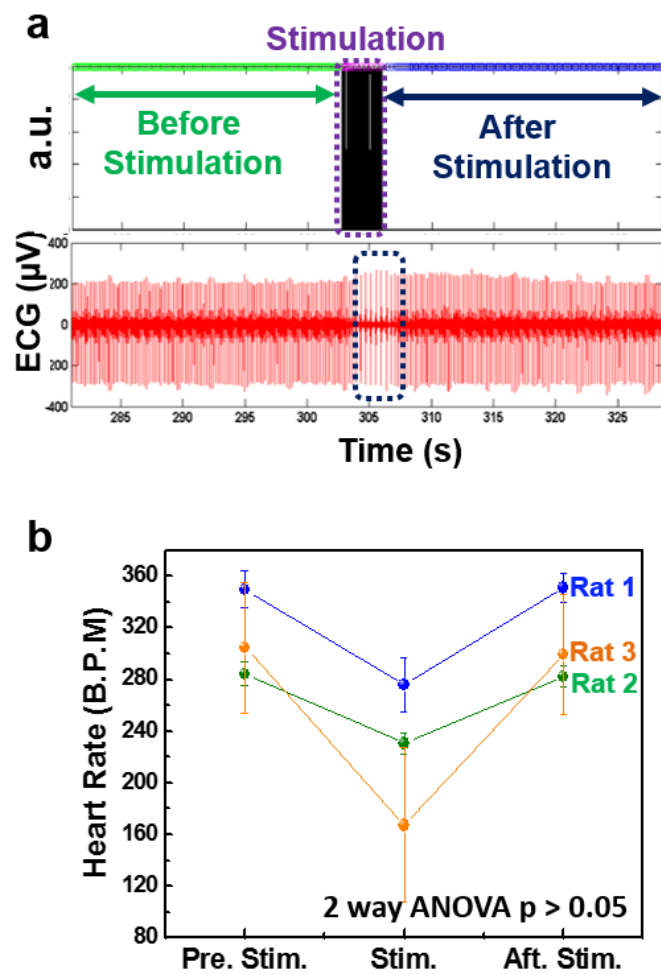


Figure 7.10 a) Electrocardiogram (ECG) recordings before and after VNS. b) The change in HR caused by VNS (2-way ANOVA, $p < 0.05$). Circles indicate the mean value and bars represent the standard error of the mean.

7.4. Stimulation of pelvic nerve for modulation of bladder function

Bladder dysfunction, which remains a major healthcare challenge and can impair daily life of patients, is a widely studied area in the field of neuromodulation [178]. Even though several approaches of neuromodulations such as posterior tibial nerve stimulation (PTNS) and sacral nerve stimulation (SNS) have been explored to control and manage the bladder dysfunction as a second-line therapy, there are still side effects and limitations; i) SNS includes dorsal root rhizotomy which causes side effects such as diminished sexual functions ii) PTNS are conducted with needle electrodes or some commercial devices which indirectly stimulates the target nerve [179, 180]. In contrast to these nerve target, the pelvic nerve is a promising stimulation target for the control of bladder function as it provides parasympathetic inputs to contract the bladder detrusor muscle, and is anatomically and functionally more specific compared to the more commonly targeted sacral nerve roots for bladder neuromodulation [178, 179, 181-183]. However, the pelvic nerves are small visceral nerves located deep within the body, which leads to difficulties in implantation, as well as maintaining contact for reliable stimulation, using current designs of neural electrodes.

We performed stimulation of the pelvic nerves (~250-300 μm) with the miniature FNC to control bladder function in rats to demonstrate the functionality of the FNC for small nerves.

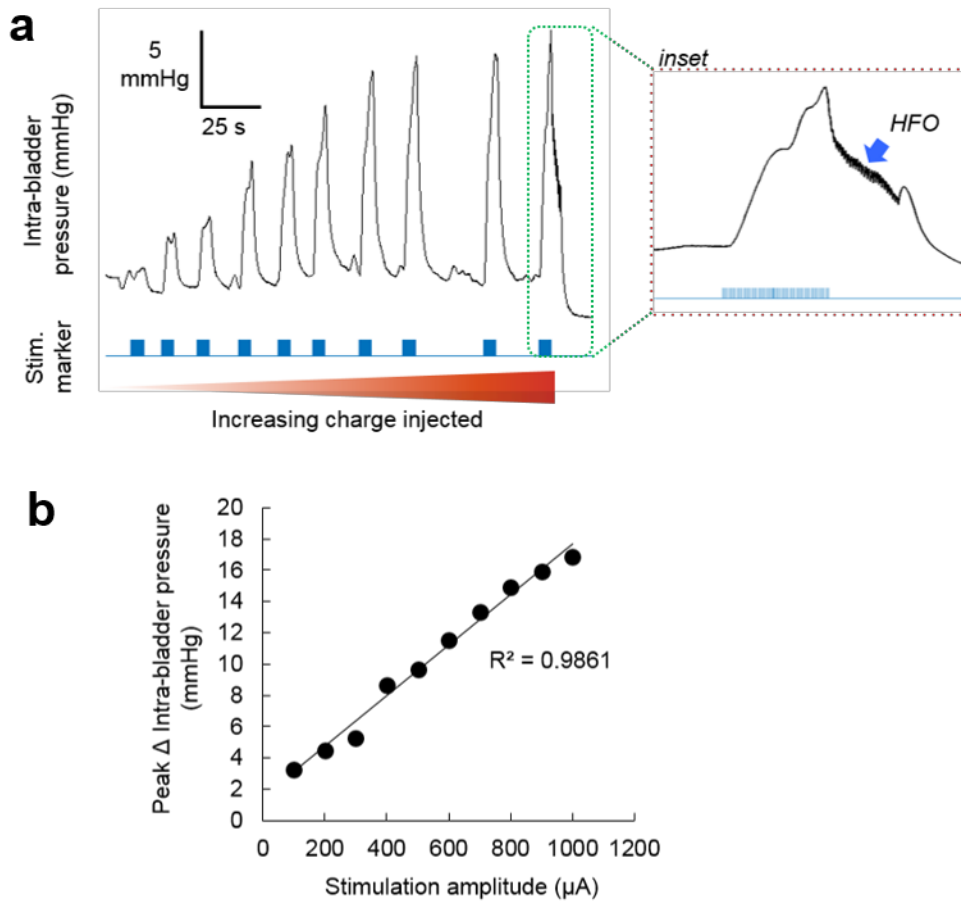


Figure 7.11 Continuous recording of intra-bladder pressure with increasing amount of charge injected via the clip electrode. Duration of stimulation is indicated by blue stimulation markers below the pressure curve. Inset shows the pressure changes associated with the stimulation trial using the highest amplitude (1000 μ A). High frequency oscillations associated (HFO) with voiding response was observed. (b) Peak increase in intra-bladder pressure is linearly correlated with amount of stimulation amplitude used.

Firstly, we conducted preliminary test to ensure correlation between stimulation amplitude and peak intra-bladder pressure changes. Lower ‘subthreshold’ stimulation amplitudes increased bladder pressures without voiding while ‘supra-threshold’ amplitude of 1000 μ A caused the largest pressure changes and led to voiding of urine. The voiding event was also visibly accompanied by high frequency oscillations of the pressure curve due to external

urethral sphincter muscle contractions (**Figure 7.11a**)- a phenomenon previously reported in other rat bladder studies based on pudendal nerve stimulation or physiological perturbation by bladder filling [13–15]. Overall, stimulation amplitude was also linearly correlated with peak intra-bladder pressure changes (**Figure 7.11b**).

To show the reproducibility of pelvic nerve stimulation using clip electrodes, we also performed repeated stimulations using supra-threshold amplitudes (**Figure 7.12a**; $n = 8$ trials). Repeatable voiding responses were obtained in all 8 trials during a single continuous recording session, with similar changes in pressures (**Figure 7.12b**; peak pressure = 12.45 ± 0.18 mmHg; time to reach peak pressure during stimulation = 2.25 ± 0.06 s, values indicate mean \pm S.E.M). To examine how reliable our clip electrodes work across different animals, we reuse the same clip electrode for experiments carried out in two rats on different days. Similar for each of the two rats, using higher stimulation amplitude caused greater peak change in intra-bladder pressures (**Figure 7.12c**) and decreased the time taken to reach the peak pressure (**Figure 7.12d**), indicating that the same clip electrode can be reliably implanted without much lost in electrode performance and is mechanically robust for handling across different experiments.

Figure 7.13a shows schematic diagram of pelvic nerve stimulation for the modulation of bladder function. The FNC also interfaced successfully with the pelvic nerve in two different implantation configurations: either 400 μm (**Figure 7.13b**) or 1600 μm (**Figure 7.13c**) inter- electrode site distance.

Increases

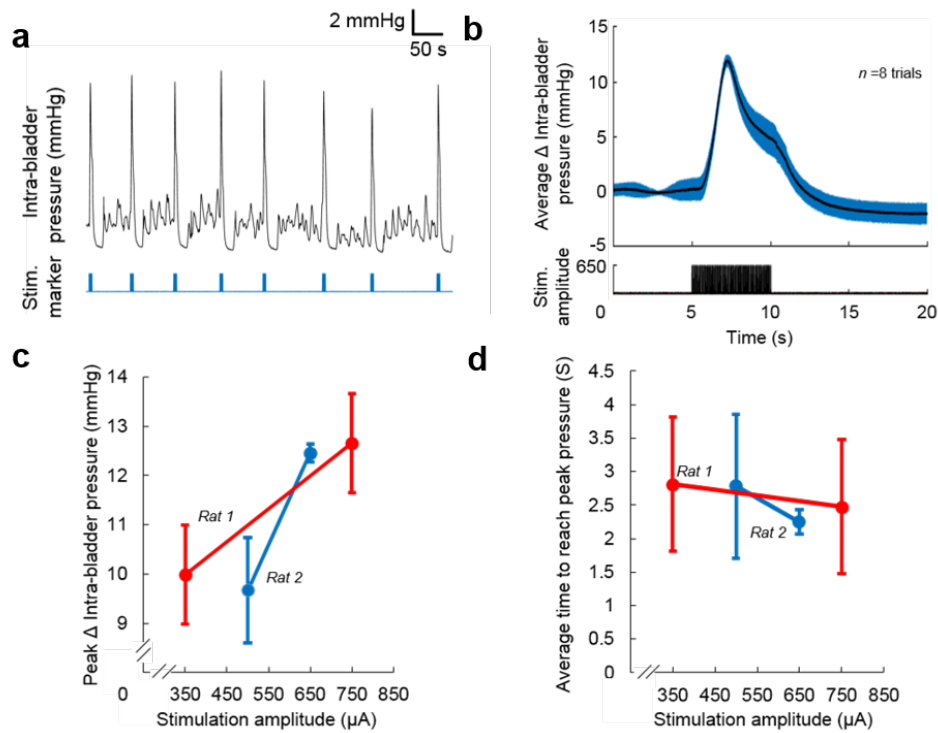


Figure 7.12 Supra-threshold stimulation of pelvic nerve produced repeatable increases in intra-bladder pressure. (a) Continuous recording of intra-bladder pressure (mmHg) during 8 trials of pelvic nerve stimulation at frequency of 10 Hz and amplitude of 650 μA . Voiding responses were observed in all 8 trials. (b) Average change in intra-bladder pressure curve from 8 trials of stimulation is indicated by the black curve while the blue shaded region indicates standard deviation. The same clip electrode produced similar responses in different rats for acute pelvic nerve stimulation experiments. Increasing stimulation amplitudes correlated with increasing peak intra-bladder pressure changes (c) and faster time to reach peak pressure during stimulation (d) in 2 consecutive experiments using the same electrode (N =2 rats).

in bladder pressure due to pelvic nerve stimulation were observed for both implantation configurations at increasing stimulation currents (range: 25- 200 μA , n = 3 trials). Lower ‘subthreshold’ stimulation amplitudes increased bladder pressure without voiding, while higher ‘supra-threshold’ amplitudes (100 and 200 μA) caused larger pressure changes, and led to graded and repeatable voiding of urine. At supra-threshold amplitudes, the urine output (**Figure 7.13a**),

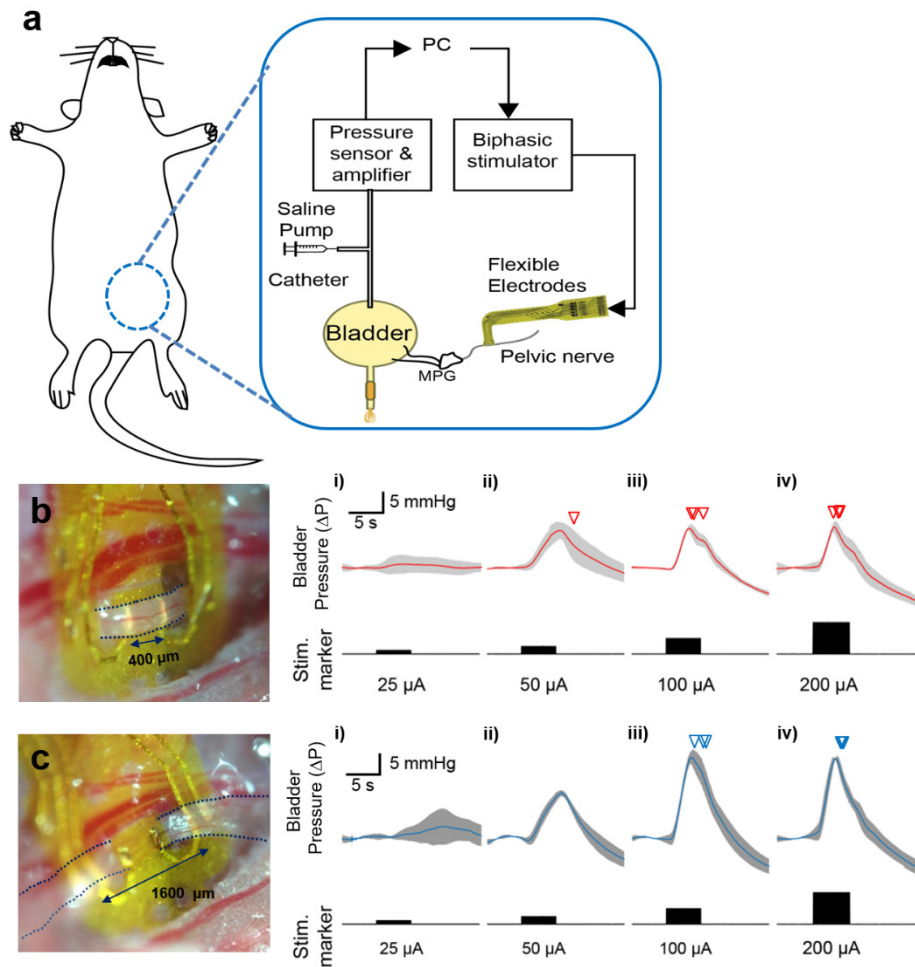


Figure 7.13 Schematic diagram of pelvic nerve stimulation for the modulation of bladder function. Evoked intra-bladder pressure changes and micturition outcome with increasing stimulation amplitudes for (b) short (400 μm) and (c) long inter-lead distances (1600 μm). Photomicrographs of implanted flexible neural clip (FNC) electrodes on the same nerve in two different configurations are shown in (b) and (c). Increases in bladder pressure due to pelvic nerve stimulation was observed for both implantation configurations at increasing stimulation current from (i) 25 μA , (ii) 50 μA , (iii) 100 μA , and (iv) 200 μA , respectively ($n = 3$ trials). Inverted triangles denote the onset of voiding events.

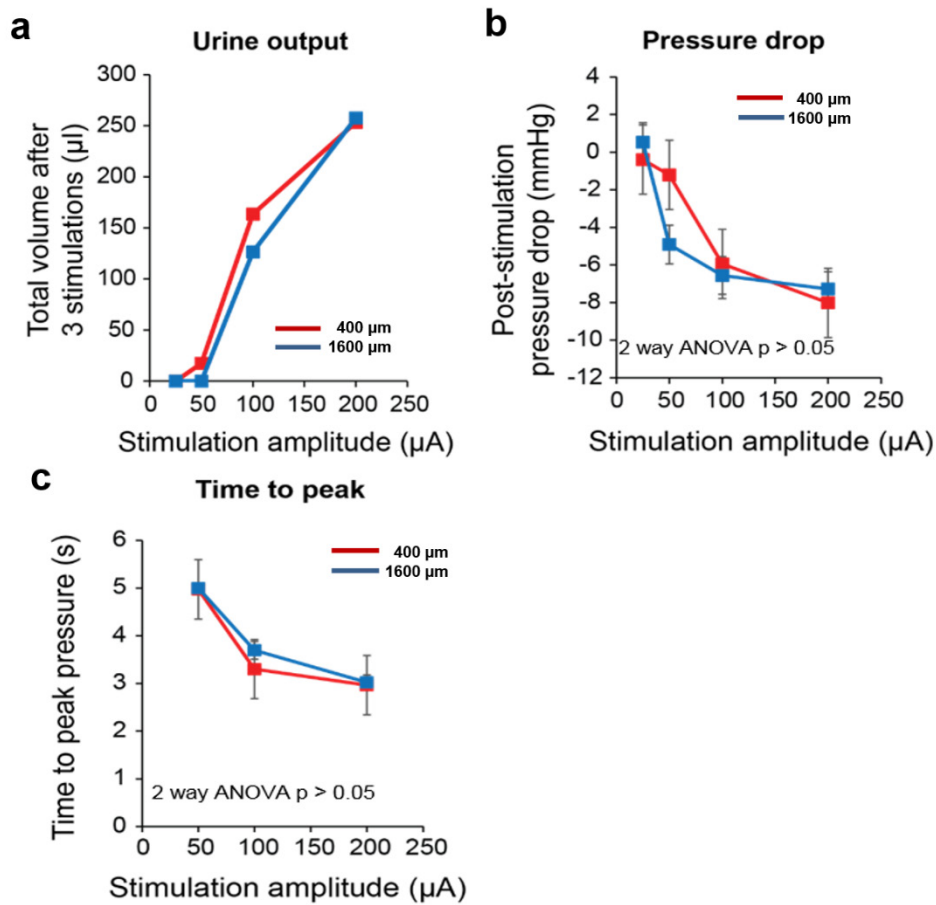


Figure 7.14 (a) Urine output as a result of different stimulation amplitudes. (b) Post stimulation pressure drops as a result of different stimulation amplitudes. (c) Time to reach peak pressure as a result of different stimulation amplitudes. At supra-threshold amplitudes, the post-stimulation pressure drop, and time to reach a peak in bladder pressure were similar and not significantly different between the two implantation configurations (2-way ANOVA, $p > 0.05$, $n = 3$ trials each).

post-stimulation pressure drop (**Figure 7.13b**), and time to reach a peak in bladder pressure (**Figure 7.13c**) were similar and not significantly different between the two implantation configurations, indicating that functional, consistent electrode-nerve interfaces were achieved in both cases. The results demonstrate that 1) the FNC can be reliably implanted onto small pelvic nerves while maintaining electrode performance, and 2) the FNC is mechanically

robust to withstand handling across different experiments. The present findings indicate that the pelvic nerve can be stimulated in a graded manner to control bladder contractions, leading to reproducible voiding events comparable with other published techniques. Notably, we showed that our novel FNC can provide effective electrical contact with the pelvic nerve for reliable and repeatable stimulation in *in vivo* anesthetized situations. The ability to use the FNC for the pelvic nerve enables more studies in the future on the potential of pelvic nerve stimulation as a therapeutic target for bladder dysfunction.

7.5. Wireless Stimulation of pelvic nerve for modulation of bladder function

To demonstrate the feasibility of wireless stimulation using the FNC, we performed wireless stimulation of pelvic nerves using the FNC integrated with midfield powering. Midfield wireless stimulation allows the transfer of milliwatt levels of power to devices in deep tissue (>5 cm) [36, 37]. **Figure 7.15a** shows the procedure for integrating the FNC with the components for midfield wireless energy transfer. The assembled FNC was able to be easily implanted in pelvic nerves in rats (**Figure 7.15b**). To ensure repetitive wireless stimulation, an external coil was fixed and positioned near the active. Firstly, we set the same stimulation parameter that was used in previous pelvic nerve stimulation, then, slightly increased the pulse phase from 150 to 500 μ s.

The prepared wireless FNC was tested in phosphate buffered saline (PBS) solution first before moving to *in vivo* experiments. The wireless FNC was implanted on a pelvic nerve. For consistent repetition of each trial, the wireless

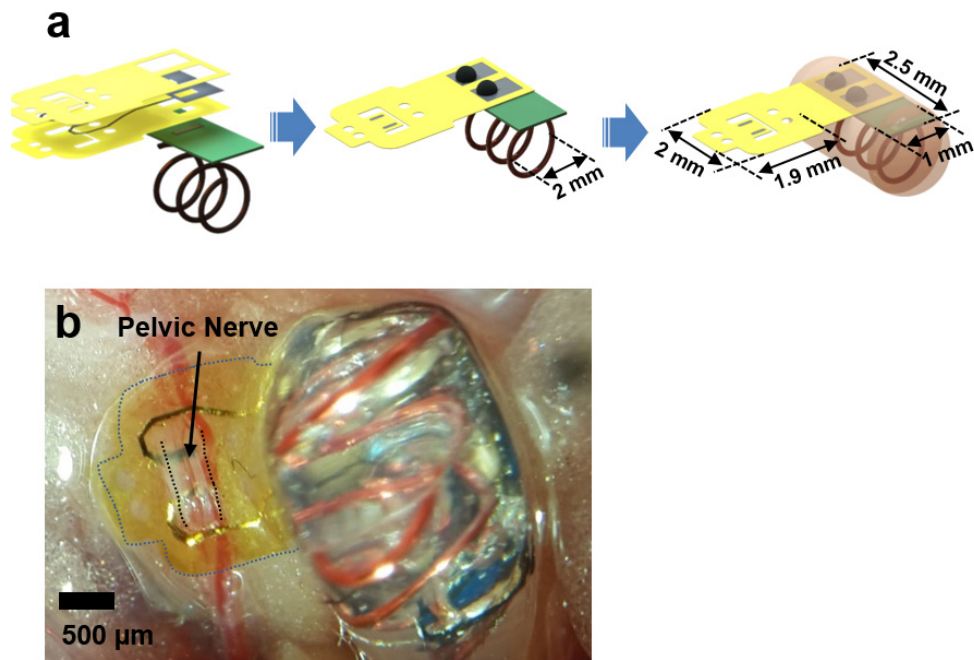


Figure 7.15 (a) Schematic diagram of the assembly of the active FNC. Firstly, active version of FNC was fabricated where contact pads matched with the size of mini-PCB. Secondly, wireless components including diodes and capacitors were soldered first on the PCB. Thirdly, the FNC was aligned on the PCB, then, silver paste was applied for electrical connections. Finally, a coil and UV LED were soldered and the entire FNC was encapsulated in a silicone elastomer except the active electrodes of the FNC. (b) A photomicrograph of the implanted active FNC on a pelvic nerve in a rat.

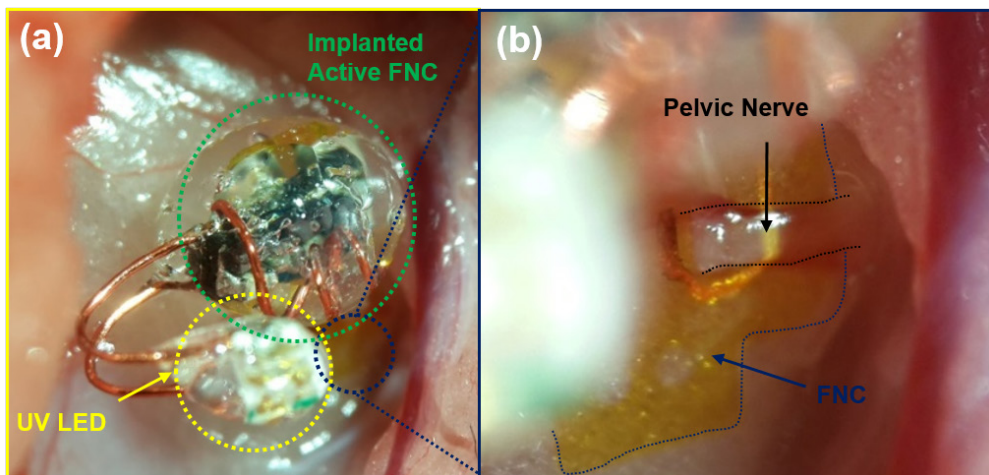


Figure 7.16 (a) A photomicrograph of implanted active flexible neural clip (FNC) interface. (b) A magnified photomicrograph of implanted FNC on a pelvic nerve.

external coil was positioned and fixed at a proper place using a manipulator. UV LED was intentionally soldered and extended outside of the wireless FNC to monitor the operation of the device and wireless stimulation (**Figure 7.16a, b**). During the stimulation, we made the implantation site dry from body fluids. Stimulation parameters were applied with a frequency of 10 Hz, duration of 5-6 seconds, and phase width of 150, 300, and 500 μ s, respectively. Intra-bladder pressure was measured in the same manner of previous test. There was at least 3 minute interval before and after each stimulation.

Figure 7.17 shows the results showing that the pelvic nerve was stably stimulated at all parameters. At the phase width of 150 μ s, overall responses such as normalized pressure and urine volume were relatively stable. The urine output increased when the phase width increased from 150 μ s to 300 μ s, but it slightly decreased from 300 to 500 μ s. Mean response time from stimulation to voiding response was 5.73 ± 0.71 s.

To demonstrate preliminary chronic test, we measured micro CT after suturing the abdomen. **Figure 7.18a** shows a micro CT image of the rat and the implanted FNC (inset) indicating that the small FNC was positioned well near pubis bone. We measured the distance between the implanted FNC and skin, which is 8.5 mm (**Figure 7.18b**). It demonstrates that wireless power transfer from ventral side would be fine due to the short depth of the implantation. A clear future direction would be to perform chronic implantations with the FNC, and assess nerve health and functionality over time so as to validate long-term applications of this novel interface design. All of our current results demonstrate that this novel FNC shows great potential for use in neuromodulation of small peripheral nerves for bioelectronic medicine applications.

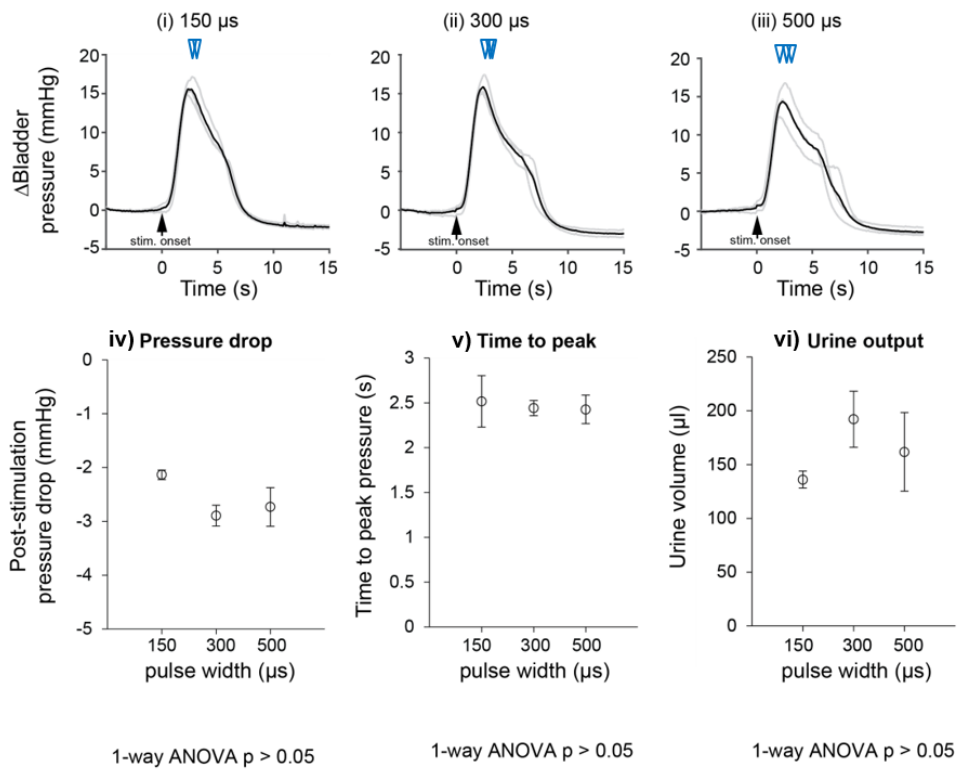


Figure 7.17 Results of the pelvic nerve stimulation on bladder pressure changes, pressure drop, time to reach peak, and urine output as a result of phase width (i) 150 μs , (ii) 300 μs , and (iii) 500 μs , respectively. Actual duration was (i) 5.21 ± 0.21 s, (ii) 6.12 ± 0.58 s, and (iii) 5.86 ± 1.00 s, respectively and the mean was 5.73 ± 0.71 s. Inverted triangles denote the onset of voiding events.

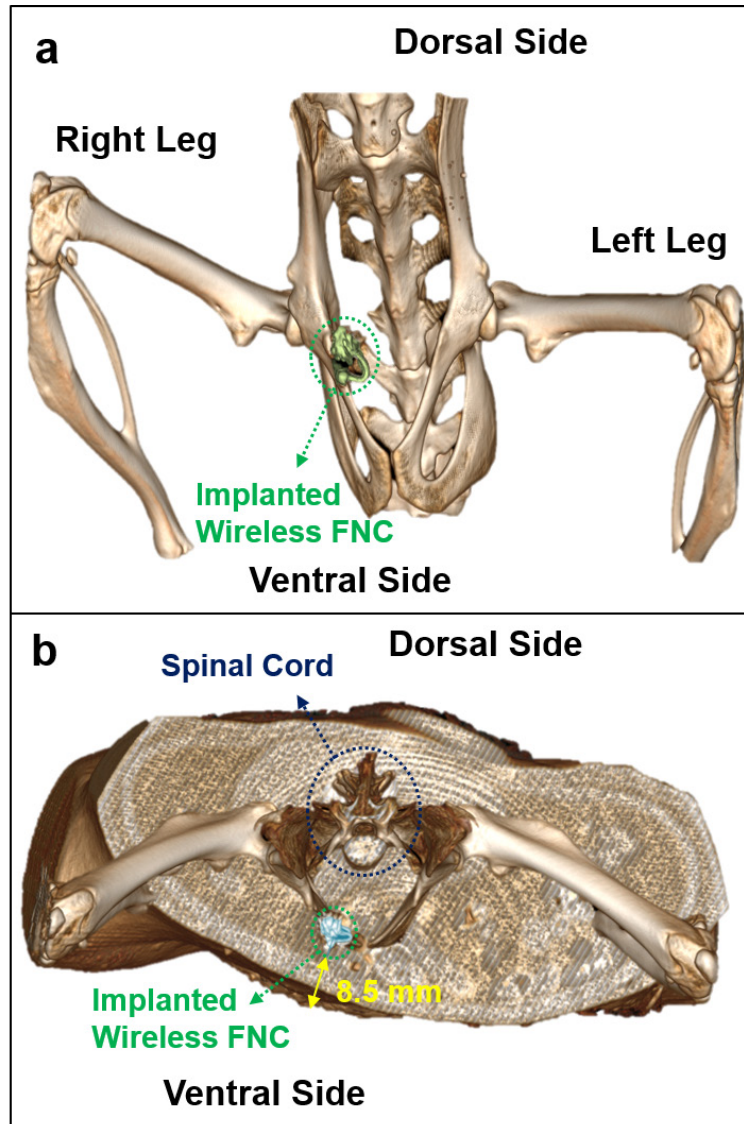


Figure 7.18 (a) Micro CT image of the implanted FNC; (inset) magnified image of the FNC. (b) Cross section view of the Micro CT image.

7.5. Discussion

We demonstrated novel neural clip interface (FNC) to stimulate small peripheral nerves for bioelectronic medicine applications. Sciatic nerve branches (common peroneal (CP) nerve, tibial nerve, and sural nerve), vagus nerve, and bladder pelvic nerves were used for the stimulation not only to validate the FNC performance but also to modulate their functionalities.

For the sciatic nerve application, we approached the branches using the FNC instead of main trunk nerve that is required for precise selective stimulation to modulate leg muscles. We sought chronaxie (T_{ch}) and rheobase current (I_{rh}) of tibial nerve and CP nerve, respectively and conducted each stimulation with the T_{ch} , respectively. We were able to observe clear ankle dorsiflexion while the CP nerve stimulation and ankle extensor (plantar-flexion) with leg stretch while the tibial nerve stimulation. Theoretically, we performed the most energy-efficient stimulation on the branches using the pulse width which is equal to each chronaxie (T_{ch}) [102]. It also indicates that multiple wireless FNCs applied to each most energy-efficient stimulation parameter for individual target nerves would be effective in improving the stimulus selectivity as well as eliminating the efforts of selective stimulation techniques through the main sciatic nerve.

For the vagus nerve application, we performed VNS using the FNC to reduce heart rate (HR) in rats. The FNC could easily be implanted on the vagus nerve despite the continuous movement of the nerve due to respiration and heartbeats. By repeating the VNS with one stimulation parameter in multiple rats, we observed a certain range of reduction of HR that was reasonable or even slightly more effective than previous studies. This result shows that the FNC can provide reliable stimulation on vagus nerves. With a smaller scale of the FNC, such as that used for pelvic nerve stimulation, the electrode could similarly be implanted onto mouse vagus nerves. Addition of more active leads on the clip strip of the FNC may provide increased spatial specificity to the stimulation. Furthermore, the wireless FNC can have great benefits in chronic epilepsy studies of small animals such as mice and rats in the future.

For the bladder nerve application, we stimulated pelvic nerve for the control

of bladder function, which is relatively less explored compared to nerve targets. Part of the reason could be due to the deep abdominal location of the pelvic nerve and respiratory-related movements of the pelvic area, which demands neural interfaces or bioelectronic implants for stable interfacing with thin visceral nerves and that is currently lacking in the field. The present findings indicate that the pelvic nerve can be stimulated in a graded manner to control bladder contractions leading to reproducible voiding events comparable with other published techniques. Notably, we showed that our novel FNC can provide effective electrical contact with the pelvic nerve for reliably and repeatable stimulation in acute in vivo anesthetized situations. The availability of the FNC for the pelvic nerve could facilitate more studies in the future on the potential of pelvic nerve stimulation for various bladder dysfunction.

Lastly, wireless FNC was demonstrated for remote modulation of bladder function in rats. The total size of the wireless FNC was 3 mm x 5 mm, which is significantly smaller size than currently developed neural interfaces and comparable with neural dust (**Figure 6a**) [34]. This tiny and wirelessly powered FNC could be reliably implanted on the small visceral pelvic nerve deeply located in the body and providing remote modulation of micturition in rats. This remote modulation of micturition with a device of several millimeters scale is a significant result that has not yet achieved with current neural interface technologies. Furthermore, we confirmed the implantation of the active FNC using micro CT imaging, indicating that the depth of wireless transfer was preferred. This wireless FNC technique will also be applied for the stimulation of vagus nerves or sciatic nerve branches to enable wireless modulation of each function in the future. With future chronic FNC implantation experiments, we

can assess nerve health and functionality over time to validate long-term efficacy and reliability of the FNC. We anticipate our interface does not only provide sciatic nerves interfacing in a paradigm-shift manner, but also pave a way of doing neural modulation for bioelectronic medicine that requires reliable modulation of small peripheral somatic and visceral nerves, thus advancing implantable bioelectronics toward untapped potential of neuromodulation.

CHAPTER 8. CONCLUSION AND FUTURE WORK

8.1. CONCLUSION

Modulation of nerve signals using implantable bioelectronics has recently been recognized as a potentially powerful way to modulate bodily conditions or communicate neuroprosthetic systems. However, creating a bioelectronic implant with a general purpose neural interface that is easy to implant, and can closely attach to small peripheral nerves without causing damage remains a grand challenge.

The aim of this work was to demonstrate various designs of epineural interface for recording and stimulation of peripheral and visceral nerves. The main results of this work are summarized below, followed by suggestions for future work.

Firstly, flexible epineural strip electrodes (FLESE) were demonstrated for neural recording of main sciatic nerves in rats. Using Au-CNT coated three sensing electrodes, bipolar and differential bipolar configurations for the recording were demonstrated. The FLESE design showed good adhesion to the sciatic nerve and branches, providing the high quality of recordings.

Secondly, selective stimulation and recording of sciatic nerves were conducted using the proposed flexible split-ring and flexible sling electrode, respectively. The split-ring interface enabled easy and quick implantation on the nerve, demonstrating the selective stimulation and recording with a transversal configuration. This design would be used for quick and easy implantation at any desired position on peripheral nerves, which is a powerful advantage

for a neural interface used in physiological studies and neuromodulation applications.

Furthermore, we demonstrated the flexible sling interface for the selective stimulation and recording for sciatic nerves. The results of the selective recording demonstrated that compound neural action potentials (CNAPs) were clearly recorded with different amplitudes and latencies. It indicated the location of the particular axon inside the sciatic nerve connecting to a common peroneal (CP) nerve, and provided a reasonable nerve conduction velocity (NCV) of the sciatic nerve. In addition, the results of the selective stimulation demonstrated that different muscle activation patterns of gastrocnemius medialis (GM) and tibialis anterior (TA) muscles were achieved. It also suggested that transverse configuration can provide more effective stimulation of the muscles using this interface. For the validation test of the sling interface for the pressure applied on the nerve, we demonstrated the blood flow measurement demonstrating that the pressure applied on the nerve by the flexible neural interface was less than that applied by commercial cuff electrodes.

As an advanced neural interface, we developed a new concept of battery-free neural interface combining the sling interface with triboelectric nanogenerators (TENGs). We proposed and optimized TENGs as a power source for direct stimulation of sciatic nerves. We demonstrated the effect of the number of layer, frequency, and confinement length to optimize the performance of the device for nerve stimulation. Direct stimulation without external sources was performed using this novel platform to modulate TA muscles. This proof-of-concept indicates that this technology could be the way

of realizing battery-free wearable neuromodulators in the future.

Finally, we demonstrated a novel neural clip (FNC) interface that allows conformal and reliable implantation on various peripheral nerves providing reliable stimulation of sciatic nerve branches, vagus nerves, and pelvic nerves for bioelectronic medicine applications. TA and the gastrocnemius (GC) muscles were selectively activated by stimulating a CP nerve and a tibial nerve, respectively. A vagus nerve was reliably stimulated using the FNC to provide safe and reversible reduction of the HR, which may be useful for heart failure (HF) and cardiac arrhythmia in the future. A Pelvic nerve was reliably and repetitively stimulated using the FNC in acute *in vivo* anesthetized situations. Finally, active FNC provided wireless stimulation of visceral pelvic nerves located deep in the body. We anticipate this interface to be useful for bioelectronic medicine that require reliable modulation of visceral nerves. Different sizes and locations of visceral nerves can be reliably stimulated using the FNC, which will be crucial in facilitating advances in neuromodulation applications in the future.

To conclude this work, the simple comparison is presented in **Figure 1.1**. Since all interfaces are non-invasive approach, only cuff electrode is included in this figure. Y axis indicates that how the interface to easily and reliably approach to small nerves. X axis presents selective functionality indicating that the capabilities of selective stimulation and recording as well as specific modulation functions. Since the FNC shows reliable stimulation of three different nerves including wireless stimulation, which any neural interfaces could not achieve, it is marked the best.

8.2. Future Work

A clear future direction would be to demonstrate chronic implantation of the proposed designs to validate the functionality for clinical applications. The histological impact of the interfaces will have to be assessed for chronic implantations outside the scope of this thesis. With future chronic implantation experiments, the nerve's health will be demonstrated by performing histological staining examining factors such as axon count, fibrosis and myelination.

Furthermore, battery-free neural interface would be more developed for clinical application by various combinations of the neural interface designs with wearable platforms of TENGs. For instance, well designed and wearable TENGs implanted on the muscle would provide a self-sustainable platform beyond the battery-free neural interfaces. The TENGs convert mechanical energy to electrical energy then neural interfaces connected with the TENGs transfer the electrical energy to electrochemical energy leading to stimulation of a peripheral nerve. Thereafter, the stimulated nerve innervates muscle activation. This muscle activation transfers mechanical energy to the TENGs again resulting in forming a closed-loop (**Figure 8.1**). Depending on theme of applications, design, position, and material of neural interfaces and TENGs can be optimized differently.

Finally, the active components can be integrated with other proposed neural interfaces. It leads to active split ring, strip, and sling interfaces as well. Depending on target nerves and functionalities, multiple implantation of various combinations of active neural interfaces will be realized. This would show great potential for use in remote neuromodulation of small peripheral nerves for

bioelectronic medicine in the future (Figure 8.2).

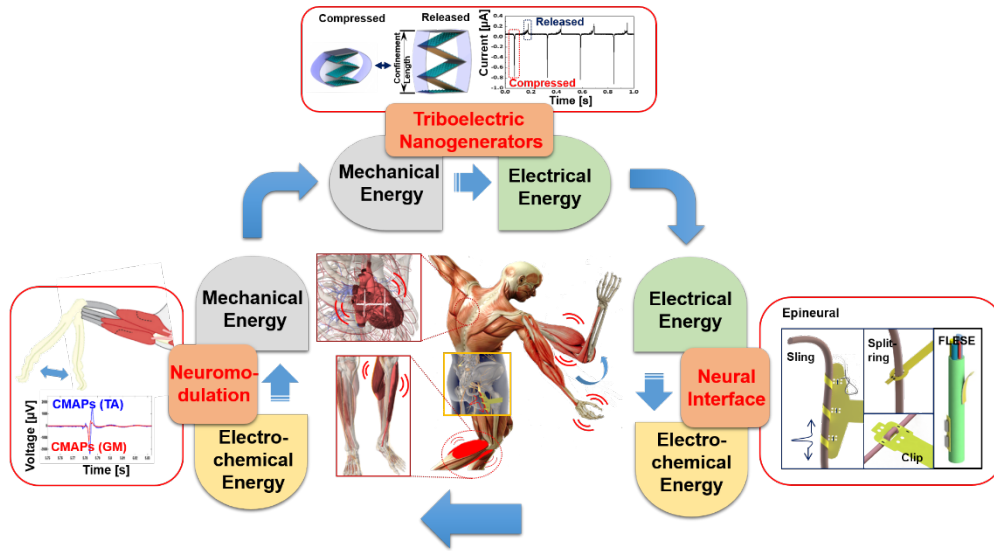


Figure 8.1 Schematic diagram of a self-sustainable platform for neuromodulation combining neural interfaces and triboelectric nanogenerators (TENGs)

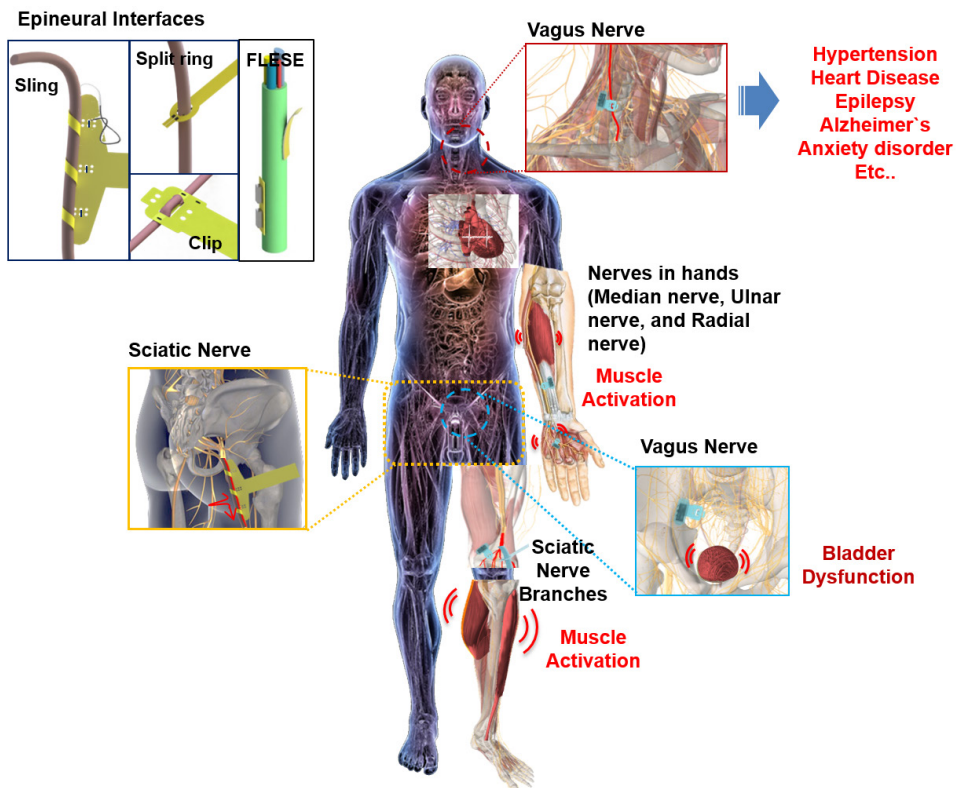


Figure 8.2 Schematic diagram of multiple implantation and applications of the neural interfaces.

BIBLIOGRAPHY

- [1] D. W. Tan, M. A. Schiefer, M. W. Keith, J. R. Anderson, J. Tyler, and D. J. Tyler, "A neural interface provides long-term stable natural touch perception," *Sci Transl Med*, vol. 6, no. 257, p. 257ra138, Oct 08 2014.
- [2] S. Raspopovic *et al.*, "Restoring natural sensory feedback in real-time bidirectional hand prostheses," *Sci Transl Med*, vol. 6, no. 222, p. 222ra19, Feb 05 2014.
- [3] D. Farina and O. Aszmann, "Bionic limbs: Clinical reality and academic Promises," *Sci Transl Med*, vol. 6, no. 257, p. 257ps12, 2014.
- [4] M. Capogrosso *et al.*, "A brain-spine interface alleviating gait deficits after spinal cord injury in primates," *Nature*, vol. 539, no. 7628, pp. 284-288, Nov 10 2016.
- [5] K. Famm, B. Litt, K. J. Tracey, E. S. Boyden, and M. Slaoui, "Drug discovery: a jump-start for electroceuticals," *Nature*, vol. 496, no. 7444, pp. 159-61, Apr 11 2013.
- [6] S. Reardon, "Electroceuticals spark interest," *Nature*, vol. 511, p. 18, 2014.
- [7] I. Adameyko, "Neural circuitry gets rewired," *Science*, vol. 354, no. 6314, pp. 833-834, 2016.
- [8] G. G. NAPLES, J. T. MORTIMER, A. SCHEINER, and J. D. SWEENEY, "A spiral nerve cuff electrode for peripheral nerve stimulation," *IEEE Transacs Biomed Eng*, vol. 35, p. 905, 1988.
- [9] J. K. Chapin and K. A. Moxon, *Neural Prostheses for Restoration of Sensory and Motor Function*. USA: CRC Press LLC, 2001.
- [10] D. J. Tyler and D. M. Durand, "Functionally selective peripheral nerve stimulation with a flat interface nerve electrode," *IEEE Trans Neural Syst Rehabil Eng*, vol. 10, no. 4, pp. 294-303, Dec 2002.
- [11] H. A. Wark *et al.*, "A new high-density (25 electrodes/mm²) penetrating microelectrode array for recording and stimulating sub-millimeter neuroanatomical structures," *J Neural Eng*, vol. 10, no. 4, p. 045003, Aug 2013.
- [12] M. B. Christensen, S. M. Pearce, N. M. Ledbetter, D. J. Warren, G. A. Clark, and P. A. Tresco, "The foreign body response to the Utah Slant Electrode Array in the cat sciatic nerve," *Acta Biomater*, vol. 10, no. 11, pp. 4650-60, Nov 2014.
- [13] H. A. Wark, K. S. Mathews, R. A. Normann, and E. Fernandez, "Behavioral and cellular consequences of high-electrode count Utah Arrays chronically implanted in rat sciatic nerve," *J Neural Eng*, vol. 11, no. 4, p. 046027, Aug 2014.
- [14] N. Lago, K. Yoshida, K. P. Koch, and X. Navarro, "Assessment of biocompatibility of chronically implanted polyimide and platinum intrafascicular electrodes," *IEEE Trans Biomed Eng*, vol. 54, no. 2, pp. 281-90, Feb 2007.
- [15] T. Boretius *et al.*, "A transverse intrafascicular multichannel electrode (TIME) to interface with the peripheral nerve," *Biosens Bioelectron*, vol. 26, no. 1, pp. 62-9, Sep 15 2010.
- [16] J. Badia, T. Boretius, A. Pascual-Font, E. Udina, T. Stieglitz, and X. Navarro, "Biocompatibility of chronically implanted transverse intrafascicular multichannel electrode (TIME) in the rat sciatic nerve," *IEEE Trans Biomed Eng*, vol. 58, no. 8, Aug 2011.
- [17] S. P. Lacour, R. Atta, J. J. FitzGerald, M. Blamire, E. Tarte, and J. Fawcett, "Polyimide micro-channel arrays for peripheral nerve regenerative implants," *Sensors and Actuators A: Physical*, vol. 147, no. 2, pp. 456-463, 2008.

- [18] S. P. Lacour, J. J. Fitzgerald, N. Lago, E. Tarte, S. McMahon, and J. Fawcett, "Long micro-channel electrode arrays: a novel type of regenerative peripheral nerve interface," *IEEE Trans Neural Syst Rehabil Eng*, vol. 17, no. 5, pp. 454-60, Oct 2009.
- [19] I. P. Clements, V. J. Mukhatyar, A. Srinivasan, J. T. Bentley, D. S. Andreasen, and R. V. Bellamkonda, "Regenerative scaffold electrodes for peripheral nerve interfacing," *IEEE Trans Neural Syst Rehabil Eng*, vol. 21, no. 4, pp. 554-66, Jul 2013.
- [20] J. Scheib and A. Hoke, "Advances in peripheral nerve regeneration," *Nat Rev Neurol*, vol. 9, no. 12, pp. 668-76, Dec 2013.
- [21] G. Di Pino *et al.*, "Invasive neural interfaces: the perspective of the surgeon," *J Surg Res*, vol. 188, no. 1, pp. 77-87, May 01 2014.
- [22] G. E. Loeb and R. A. Peck, "Cuff electrodes for chronic stimulation and recording of peripheral nerve activity," *J Neurosci Methods*, vol. 64, pp. 95-103, 1996.
- [23] J. J. Struijk, M. Thomsen, J. O. Larsen, and T. Sinkjaer, "Cuff electrodes for long-term recording of natural sensory information," *IEEE EMBS*, vol. 18, no. 3, pp. 91-98, 1999.
- [24] J. M.-M. Max Ortiz-Catalan, Jean Delbeke, Bo Hakansson, Rickard Branemark, "Effect on signal-to-noise ratio of splitting the continuous contacts of cuff electrodes into smaller recording areas," *J Neuroeng Rehabil*, vol. 10, no. 22, pp. 1-15, 2013.
- [25] A. P. Amar, M. L. Levy, C. Y. Liu, and M. L. J. Apuzzo, "Vagus Nerve Stimulation," *Proceedings of the IEEE*, vol. 96, no. 7, pp. 1142-1151, 2008.
- [26] V. M. Tronnier, "Vagus Nerve Stimulation: Surgical Technique and Complications," *Prog Neurol Surg*, vol. 29, pp. 29-38, 2015.
- [27] S. Lee *et al.*, "Selective stimulation and neural recording on peripheral nerves using flexible split ring electrodes," *Sensors and Actuators B: Chemical*, 2016.
- [28] D. N. Heo *et al.*, "Flexible and Highly Biocompatible Nanofiber-Based Electrodes for Neural Surface Interfacing," *ACS Nano*, Feb 17 2017.
- [29] S. Lee *et al.*, "Flexible Epineural Strip Electrode for Recording in Fine Nerves," *IEEE Trans Biomed Eng*, vol. 63, no. 3, pp. 581-7, Mar 2016.
- [30] Z. Xiang *et al.*, "Mapping of Small Nerve Trunks and Branches Using Adaptive Flexible Electrodes," *Advanced Science*, vol. 3, no. 9, p. 1500386, 2016.
- [31] Z. Xiang *et al.*, "Progress of Flexible Electronics in Neural Interfacing - A Self-Adaptive Non-Invasive Neural Ribbon Electrode for Small Nerves Recording," *Adv Mater*, vol. 28, no. 22, pp. 4472-9, Jun 2016.
- [32] S. Lee *et al.*, "Development of battery-free neural interface and modulated control of tibialis anterior muscle via common peroneal nerve based on triboelectric nanogenerators (TEENGs)," *Nano Energy*, vol. 33, pp. 1-11, 2017.
- [33] S. W. Lee, F. Fallegger, B. D. F. Casse, and S. I. Fried, "Implantable microcoils for intracortical magnetic stimulation," *Sci Adv*, vol. 2, p. e1600889, 2016.
- [34] D. Seo *et al.*, "Wireless Recording in the Peripheral Nervous System with Ultrasonic Neural Dust," *Neuron*, vol. 91, no. 3, pp. 529-39, Aug 03 2016.
- [35] D. R. Agrawal *et al.*, "Conformal phased surfaces for wireless powering of bioelectronic microdevices," *Nature Biomedical Engineering*, vol. 1, no. 3, p. 0043, 2017.
- [36] J. S. Ho *et al.*, "Wireless power transfer to deep-tissue microimplants," *Proc Natl Acad Sci U S A*, vol. 111, no. 22, pp. 7974-9, Jun 3 2014.
- [37] S. Kim, J. S. Ho, L. Y. Chen, and A. S. Y. Poon, "Wireless power transfer to a cardiac implant," *Applied Physics Letters*, vol. 101, no. 7, p. 073701, 2012.

- [38] M. Amjadi, K.-U. Kyung, I. Park, and M. Sitti, "Stretchable, Skin-Mountable, and Wearable Strain Sensors and Their Potential Applications: A Review," *Advanced Functional Materials*, vol. 26, no. 11, pp. 1678-1698, 2016.
- [39] S. Choi, H. Lee, R. Ghaffari, T. Hyeon, and D. H. Kim, "Recent Advances in Flexible and Stretchable Bio-Electronic Devices Integrated with Nanomaterials," *Adv Mater*, vol. 28, no. 22, pp. 4203-18, Jun 2016.
- [40] A. Chortos, J. Liu, and Z. Bao, "Pursuing prosthetic electronic skin," *Nat Mater*, vol. 15, no. 9, pp. 937-50, Sep 2016.
- [41] Y. Khan, A. E. Ostfeld, C. M. Lochner, A. Pierre, and A. C. Arias, "Monitoring of Vital Signs with Flexible and Wearable Medical Devices," *Adv Mater*, vol. 28, no. 22, pp. 4373-95, Jun 2016.
- [42] T. Q. Trung and N. E. Lee, "Flexible and Stretchable Physical Sensor Integrated Platforms for Wearable Human-Activity Monitoring and Personal Healthcare," *Adv Mater*, vol. 28, no. 22, pp. 4338-72, Jun 2016.
- [43] X. Wang, L. Dong, H. Zhang, R. Yu, C. Pan, and Z. L. Wang, "Recent Progress in Electronic Skin," *Advanced Science*, vol. 2, no. 10, p. 1500169, 2015.
- [44] T. Someya, Z. Bao, and G. G. Malliaras, "The rise of plastic bioelectronics," *Nature*, vol. 540, no. 7633, pp. 379-385, Dec 14 2016.
- [45] K. Birmingham *et al.*, "Bioelectronic medicines: a research roadmap," *Nat Rev Drug Discov*, vol. 13, no. 6, pp. 399-400, Jun 2014.
- [46] J. Kim, R. Ghaffari, and D.-H. Kim, "The quest for miniaturized soft bioelectronic devices," *Nature Biomedical Engineering*, vol. 1, no. 3, p. 0049, 2017.
- [47] J. J. Norton *et al.*, "Soft, curved electrode systems capable of integration on the auricle as a persistent brain-computer interface," *PNAS*, vol. 112, no. 13, pp. 3920-3925, 2015.
- [48] "Durable miniaturized bioelectronics," *Nature Biomedical Engineering*, vol. 1, no. 3, p. 0053, 2017.
- [49] J. Thimot and K. L. Shepard, "Bioelectronic devices: Wirelessly powered implants," *Nature Biomedical Engineering*, vol. 1, no. 3, p. 0051, 2017.
- [50] S. P. Lacour, G. Courtine, and J. Guck, "Materials and technologies for soft implantable neuroprostheses," *Nature Reviews Materials*, vol. 1, no. 10, p. 16063, 2016.
- [51] L. Luan *et al.*, "Ultraflexible nanoelectronic probes form reliable, glial scar-free neural integration," *Sci Adv*, vol. 3, p. e1601966, 2017.
- [52] C. Xie, J. Liu, T. M. Fu, X. Dai, W. Zhou, and C. M. Lieber, "Three-dimensional macroporous nanoelectronic networks as minimally invasive brain probes," *Nat Mater*, vol. 14, no. 12, pp. 1286-92, Dec 2015.
- [53] I. R. Mineev *et al.*, "Electronic dura mater long term multimodal neural interfaces," *Science*, vol. 347, pp. 159-163, 2015.
- [54] K. T. Patton, *Anatomy & Physiology*. Elsevier, 2010.
- [55] K. M. Musick *et al.*, "Chronic multichannel neural recordings from soft regenerative microchannel electrodes during gait," *Sci Rep*, vol. 5, p. 14363, Sep 24 2015.
- [56] G. E. Rutkowski, C. A. Miller, S. Jeftinija, and S. K. Mallapragada, "Synergistic effects of micropatterned biodegradable conduits and Schwann cells on sciatic nerve regeneration," *J Neural Eng*, vol. 1, no. 3, pp. 151-7, Sep 2004.
- [57] C. Xu *et al.*, "Electrical stimulation promotes regeneration of defective peripheral nerves after delayed repair intervals lasting under one month," *PLoS One*, vol. 9, no. 9, p. e105045, 2014.
- [58] R. Mohammadi, D. Faraji, H. Alemi, and A. Mokarizadeh, "Pulsed electromagnetic fields accelerate functional recovery of transected sciatic

- nerve bridged by chitosan conduit: an animal model study," *Int J Surg*, vol. 12, no. 12, pp. 1278-85, Dec 2014.
- [59] G. A. Leitao-Sene, F. F. Almeida-Sousa, V. S. Fazan, and C. H. Barbieri, "Effects of laser therapy in peripheral nerve regeneration," *Acta Ortop Bras*, vol. 21, pp. 226-270, 2013.
- [60] A. Branner, S. R. B., and R. A. Normann, "Selective stimulation of cat scaitic nerve using an array of varying length microelectrodes," *J Neurophysiol*, vol. 85, pp. 1585-1594, 2001.
- [61] S. Micera *et al.*, "On the use of longitudinal intrafascicular peripheral interfaces for the control of cybernetic hand prostheses in amputees," *IEEE Trans Neural Syst Rehabil Eng*, vol. 16, no. 5, pp. 453-72, Oct 2008.
- [62] P. M. rossi *et al.*, "Double nerve intraneural interface implant on a human amputee for robotic hand control," *Clin Neurophy*, vol. 121, pp. 777-783, 2010.
- [63] X. Navarro, T. B. Krueger, N. Lago, S. Micera, T. Stieglitz, and P. Dario, "A critical review of interfaces with the peripheral nervous system for the control of neuroprostheses and hybrid bionic systems," *J Peirpher Nerv Sys*, vol. 10, pp. 229-258, 2005.
- [64] C. Hassler, T. Boretius, and T. Stieglitz, "Polymers for neural implants," *Journal of Polymer Science Part B: Polymer Physics*, vol. 49, no. 1, pp. 18-33, 2011.
- [65] M. A. Schiefer *et al.*, "Selective activation of the human tibial and common peroneal nerves with a flat interface nerve electrode," *J Neural Eng*, vol. 10, no. 5, p. 056006, Oct 2013.
- [66] A. Branner and R. A. Normann, "A multielectrode array for intrafascicular recording and stimulation in sciatic nerve of cats," *Brain Res*, vol. 51, no. 4, p. 293, 2000.
- [67] K. S. Mathews *et al.*, "Acute monitoring of genitourinary function using intrafascicular electrodes: selective pudendal nerve activity corresponding to bladder filling, bladder fullness, and genital stimulation," *Urology*, vol. 84, no. 3, pp. 722-9, Sep 2014.
- [68] A. K. Thota *et al.*, "A Multi-lead Multi-electrode System for Neural-interface Enabled Advanced Prostheses," pp. 109-110, 2013.
- [69] S. M. Restaino, E. Abliz, K. Wachrathit, V. Krauthamer, and S. B. Shah, "Biomechanical and functional variation in rat sciatic nerve following cuff electrode implantation," *J Neuroeng Rehabil*, vol. 11, p. 73, 2014.
- [70] B. Hiebl *et al.*, "In vivo assessment of tissue compatibility and functionality of a polyimide cuff electrode for recording afferent peripheral nerve signals," *Appl Cardiopulm Pathophysiol*, vol. 14, pp. 212-219, 2010.
- [71] D. T. Plachta *et al.*, "Blood pressure control with selective vagal nerve stimulation and minimal side effects," *J Neural Eng*, vol. 11, no. 3, p. 036011, Jun 2014.
- [72] A. J. Camm and I. Savelieva, "Vagal nerve stimulation in heart failure," *Eur Heart J*, vol. 36, no. 7, pp. 404-6, Feb 14 2015.
- [73] S. W. Lee *et al.*, "Chronic cyclic vagus nerve stimulation has beneficial electrophysiological effects on healthy hearts in the absence of autonomic imbalance," *Physiol Rep*, vol. 4, no. 9, p. e12786, May 2016.
- [74] D. Ojeda *et al.*, "Sensitivity Analysis of Vagus Nerve Stimulation Parameters on Acute Cardiac Autonomic Responses: Chronotropic, Inotropic and Dromotropic Effects," *PLoS One*, vol. 11, no. 9, p. e0163734, 2016.
- [75] Y. M. Dweiri, T. E. Eggers, L. E. Gonzalez-Reyes, J. Drain, G. A. McCallum, and D. M. Durand, "Stable Detection of Movement Intent From Peripheral Nerves: Chronic Study in Dogs," *Proceedings of the IEEE*, vol. 105, no. 1, pp. 50-65, 2017.

- [76] H. Yu, W. Xiong, H. Zhang, W. Wang, and Z. Li, "A Parylene Self-Locking Cuff Electrode for Peripheral Nerve Stimulation and Recording," *Journal of Microelectromechanical Systems*, vol. 23, no. 5, pp. 1025-1035, 2014.
- [77] X. Kang, J.-Q. Liu, H. Tian, B. Yang, Y. Nuli, and C. Yang, "Self-Closed Parylene Cuff Electrode for Peripheral Nerve Recording," *Journal of Microelectromechanical Systems*, vol. 24, no. 2, pp. 319-332, 2015.
- [78] J. Pisapia and G. Baltuch, "Vagus nerve stimulation: Introduction and technical aspects," in *Neuromodulation in Psychiatry*, C. Hamani, P. Holtzheimer, A. M. Lozano, and H. Mayberg, Eds. UK: John Wiley & Sons, Ltd, 2016.
- [79] T. Stieglitz, M. Schuettler, B. Rubehn, T. Boretius, J. Badia, and X. Navarro, "Evaluation of polyimide as substrate material for electrodes to interface the peripheral nervous system," in *IEEE EMBS*, 2011.
- [80] T. Stieglitz, M. Schuettler, and K. P. Koch, "Implantation biomedical microsystems for neural prostheses," presented at the IEEE Engineering in medicine and biology magazine, 2005.
- [81] P. E. K. Donaldson and B. J. Aylett, *Aspects of silicone rubber as encapsulant for neurological prostheses*. Medical and Biological Engineering and Computing, 1995.
- [82] C. Hassler, R. P. von Metzen, P. Ruther, and T. Stieglitz, "Characterization of parylene C as an encapsulation material for implanted neural prostheses," *J Biomed Mater Res B Appl Biomater*, vol. 93, no. 1, pp. 266-74, Apr 2010.
- [83] A. A. Fomani and R. R. Mansour, "Fabrication and characterization of the flexible neural microprobes with improved structural design," *Sensors and Actuators A: Physical*, vol. 168, no. 2, pp. 233-241, 2011.
- [84] Y. Sun, S. P. Lacour, R. A. Brooks, N. Rushton, J. Fawcett, and R. E. Cameron, "Assessment of the biocompatibility of photosensitive polyimide for implantable medical device use," *J Biomed Mater Res A*, vol. 90, no. 3, pp. 648-55, Sep 01 2009.
- [85] X. Jiang *et al.*, "In vitro and in vivo evaluation of a photosensitive polyimide thin-film microelectrode array suitable for epiretinal stimulation," *J Neuroeng Rehabil*, vol. 10, p. 48, May 29 2013.
- [86] Y. X. Kato, S. Furukawa, K. Samejima, N. Hironaka, and M. Kashino, "Photosensitive-polyimide based method for fabricating various neural electrode architectures," *Front Neuroeng*, vol. 5, p. 11, 2012.
- [87] J. H. Kim *et al.*, "An Electroplating-Free and Minimal Noise Polyimide Microelectrode for Recording Auditory Evoked Potentials From the Epicranium," *IEEE Trans Biomed Eng*, vol. 60, no. 12, pp. 3425-31, Dec 2013.
- [88] J. Badia, T. Boretius, D. Andreu, C. Azevedo-Coste, T. Stieglitz, and X. Navarro, "Comparative analysis of transverse intrafascicular multichannel, longitudinal intrafascicular and multipolar cuff electrodes for the selective stimulation of nerve fascicles," *J Neural Eng*, vol. 8, no. 3, p. 036023, Jun 2011.
- [89] K. Gao, G. Li, L. Liao, J. Cheng, J. Zhao, and Y. Xu, "Fabrication of flexible microelectrode arrays integrated with microfluidic channels for stable neural interfaces," *Sensors and Actuators A: Physical*, vol. 197, pp. 9-14, 2013.
- [90] K. W. Horch and G. S. Dhillon, *Neuroprosthetics: Theory and Practice* (no. 2). World Scientific Publishing Co. Pte. Ltd., 2004.
- [91] Z. Xiang *et al.*, "Ultra-thin flexible polyimide neural probe embedded in a dissolvable maltose-coated microneedle," *Journal of Micromechanics and Microengineering*, vol. 24, no. 6, p. 065015, 2014.
- [92] K. Wang, H. A. Fishman, H. Dai, and J. S. Harris, "Neural stimulation with a carbon nanotube microelectrode array," *Nano lett*, vol. 6, no. 9, pp. 2043-2048, 2006.

- [93] P. Galvan-Garcia *et al.*, "Robust cell migration and neuronal growth on pristine carbon nanotube sheets and yarns," *J Biomater Sci Polym Ed*, vol. 18, no. 10, pp. 1245-61, 2007.
- [94] A. O. Lobo, E. F. Antunes, A. H. A. Machado, C. Pacheco-Soares, V. J. Trava-Airoldi, and E. J. Corat, "Cell viability and adhesion on as grown multi-wall carbon nanotube films," *Materials Science and Engineering: C*, vol. 28, no. 2, pp. 264-269, 2008.
- [95] G. Cellot *et al.*, "Carbon nanotubes might improve neuronal performance by favouring electrical shortcuts," *Nat Nanotechnol*, vol. 4, no. 2, pp. 126-33, Feb 2009.
- [96] A. O. Fung *et al.*, "Electrochemical properties and myocyte interaction of carbon nanotube microelectrodes," *Nano Lett*, vol. 10, no. 11, pp. 4321-7, Nov 10 2010.
- [97] E. W. Keefer, B. R. Botterman, M. I. Romero, A. F. Rossi, and G. W. Gross, "Carbon nanotube coating improves neuronal recordings," *Nat Nanotechnol*, vol. 3, no. 7, pp. 434-9, Jul 2008.
- [98] S. Minnikanti and N. Peixoto, "Implantable electrodes with carbon nanotube coatings," in *Carbon nanotubes applications on electron devices: InTech*, 2011.
- [99] W. Franks, I. Schenker, P. Schmutz, and A. Hierlemann, "Impedance characterization and modeling of electrodes for biomedical applications," *IEEE Trans Biomed Eng*, vol. 52, no. 7, pp. 1295-302, Jul 2005.
- [100] R. S. Martins, M. G. Siqueira, C. F. D. Silva, B. O. D. Godoy, and J. P. P. Plese, "Electrophysiologic assessment of generation in rat sciatic nerve repair using suture, fibrin glue or a combination of both techniques," *Arq Neuropsiquiatr*, vol. 63, pp. 601-604, 2005.
- [101] M. E. Walsh, L. B. Sloane, K. E. Fischer, S. N. Austad, A. Richardson, and H. Van Remmen, "Use of Nerve Conduction Velocity to Assess Peripheral Nerve Health in Aging Mice," *J Gerontol A Biol Sci Med Sci*, vol. 70, no. 11, pp. 1312-9, Nov 2015.
- [102] J. G. Thalhammer, M. Vladimirova, B. Bershady, and G. R. Strichartz, "Neurologic evaluation of the rat during sciatic nerve block with lidocaine," *Anesthesiology*, vol. 82, pp. 1013-1025, 1995.
- [103] H. K. Naser Pour Aryan, Albrecht Rothermel, *Stimulation and Recording Electrodes for Neural Prostheses*. Springer, 2015.
- [104] S. F. Cogan, "Neural stimulation and recording electrodes," *Annu Rev Biomed Eng*, vol. 10, pp. 275-309, 2008.
- [105] E. Slavcheva, R. Vitushinsky, W. Mokwa, and U. Schnakenberg, "Sputtered Iridium Oxide Films as Charge Injection Material for Functional Electrostimulation," *Journal of The Electrochemical Society*, vol. 151, no. 7, p. E226, 2004.
- [106] L. D. Liao *et al.*, "Imaging brain hemodynamic changes during rat forepaw electrical stimulation using functional photoacoustic microscopy," *Neuroimage*, vol. 52, no. 2, pp. 562-70, Aug 15 2010.
- [107] M. Ortiz-Catalan, J. Marin-Millan, J. Delbeke, B. Hakansson, and R. Branemark, "Effect of signal-to-noise ratio of splitting the continuous contacts of cuff electrodes into smaller recording areas," *J Neuroeng Rehabil*, vol. 10, no. 22, pp. 1-15, 2013.
- [108] Y. F. Rui, J. Q. Liu, B. Yang, K. Y. Li, and C. S. Yang, "Parylene-based implantable platinum-black coated wire microelectrode for orbicularis oculi muscle electrical stimulation," *Biomed Microdevices*, vol. 14, no. 2, pp. 367-73, Apr 2012.
- [109] C. Zhang *et al.*, "Implantable electrode array with platinum black coating for brain stimulation in fish," *Microsystem Technologies*, vol. 21, no. 1, pp. 139-145, 2013.

- [110] A. Mallik and A. I. Weir, "Nerve conduction studies: essentials and pitfalls in practice," *J Neurol Neurosurg Psychiatry*, vol. 76 Suppl 2, pp. ii23-31, Jun 2005.
- [111] N. Huseyinoglu, I. Ozaydin, U. Huseyinoglu, S. Yayla, and O. Aksoy, "Minimally Invasive Motor Nerve Conduction Study of the Rat Sciatic and Tail Nerves," *Kafkas Universitesi Veteriner Fakultesi Dergisi*, 2013.
- [112] T. N. Nielsen, G. A. Kurstjens, and J. J. Struijk, "Transverse versus longitudinal tripolar configuration for selective stimulation with multipolar cuff electrodes," *IEEE Trans Biomed Eng*, vol. 58, no. 4, pp. 913-9, Apr 2011.
- [113] L. D. Liao *et al.*, "Investigation of the cerebral hemodynamic response function in simple blood vessel by functional photoacoustic microscopy," *J Biomed Opt*, vol. 17, p. 061210, 2012.
- [114] L. D. Liao *et al.*, "Transcranial imaging of functional cerebral hemodynamic changes in single blood vessels using in vivo photoacoustic microscopy," *J Cereb Blood Flow Metab*, vol. 32, no. 6, pp. 938-51, Jun 2012.
- [115] R. Hinchet, W. Seung, and S. W. Kim, "Recent Progress on Flexible Triboelectric Nanogenerators for Self-Powered Electronics," *ChemSus Chem*, vol. 8, pp. 2327-2344, 2015.
- [116] F. R. Fan, W. Tang, and Z. L. Wang, "Flexible Nanogenerators for Energy Harvesting and Self-Powered Electronics," *Adv Mater*, vol. 28, no. 22, pp. 4283-305, Jun 2016.
- [117] H. Wang, G. Pastorin, and C. Lee, "Toward Self-Powered Wearable Adhesive Skin Patch with Bendable Microneedle Array for Transdermal Drug Delivery," *Adv Sci (Weinh)*, vol. 3, no. 9, p. 1500441, Sep 2016.
- [118] H. Wang *et al.*, "Triboelectric liquid volume sensor for self-powered lab-on-chip applications," *Nano Energy*, vol. 23, pp. 80-88, 2016.
- [119] R. Jegadeesan, S. Nag, K. Agarwal, N. V. Thakor, and Y. X. Guo, "Enabling wireless powering and telemetry for peripheral nerve implants," *IEEE J Biomed Health Inform*, vol. 19, no. 3, pp. 958-70, May 2015.
- [120] R. Latham, "Biomedical applications of batteries," *Solid State Ionics*, vol. 172, no. 1-4, pp. 7-11, 2004.
- [121] D. C. Bock, A. C. Marschilok, K. J. Takeuchi, and E. S. Takeuchi, "Batteries used to Power Implantable Biomedical Devices," *Electrochim Acta*, vol. 84, Dec 1 2012.
- [122] J. Xie, C. Lee, and H. Feng, "Design, Fabrication, and Characterization of CMOS MEMS-Based Thermoelectric Power Generators," *Journal of Microelectromechanical Systems*, vol. 19, no. 2, pp. 317-324, 2010.
- [123] J. H. We, S. J. Kim, and B. J. Cho, "Hybrid composite of screen-printed inorganic thermoelectric film and organic conducting polymer for flexible thermoelectric power generator," *Energy*, vol. 73, pp. 506-512, 2014.
- [124] Z. Lu, H. Zhang, C. Mao, and C. M. Li, "Silk fabric-based wearable thermoelectric generator for energy harvesting from the human body," *Applied Energy*, vol. 164, pp. 57-63, 2016.
- [125] S. J. Kim, J. H. We, and B. J. Cho, "A wearable thermoelectric generator fabricated on a glass fabric," *Energy Environ Sci*, vol. 7, no. 6, p. 1959, 2014.
- [126] M. Hyland, H. Hunter, J. Liu, E. Veety, and D. Vashaee, "Wearable thermoelectric generators for human body heat harvesting," *Applied Energy*, vol. 182, pp. 518-524, 2016.
- [127] H. Zhang *et al.*, "A flexible and implantable piezoelectric generator harvesting energy from the pulsation of ascending aorta: in vitro and in vivo studies," *Nano Energy*, vol. 12, pp. 296-304, 2015.
- [128] X. Cheng *et al.*, "Implantable and self-powered blood pressure monitoring based on a piezoelectric thinfilm: Simulated, in vitro and in vivo studies," *Nano Energy*, vol. 22, pp. 453-460, 2016.

- [129] G. T. Hwang *et al.*, "Self-powered deep brain stimulation via a flexible PIMNT energy harvester," *Energy Environ Sci*, vol. 8, no. 9, pp. 2677-2684, 2015.
- [130] C. K. Jeong *et al.*, "Flexible highly-effective energy harvester via crystallographic and computational control of nanointerfacial morphotropic piezoelectric thin film," *Nano Research*, 2016.
- [131] G. Sahara, W. Hijikata, K. Tomioka, and T. Shinshi, "Implantable power generation system utilizing muscle contractions excited by electrical stimulation," *Proc Inst Mech Eng H*, vol. 230, no. 6, pp. 569-78, Jun 2016.
- [132] F.-R. Fan, Z.-Q. Tian, and Z. L. Wang, "Flexible triboelectric generator," *Nano Energy*, vol. 1, no. 2, pp. 328-334, 2012.
- [133] G. Zhu *et al.*, "Toward large-scale energy harvesting by a nanoparticle-enhanced triboelectric nanogenerator," *Nano letters*, vol. 13, no. 2, pp. 847-853, 2013.
- [134] Y. Xie *et al.*, "Rotary triboelectric nanogenerator based on a hybridized mechanism for harvesting wind energy," *ACS nano*, vol. 7, no. 8, pp. 7119-7125, 2013.
- [135] B. Meng *et al.*, "A transparent single-friction-surface triboelectric generator and self-powered touch sensor," *Energy Environ. Sci.*, vol. 6, no. 11, pp. 3235-3240, 2013.
- [136] L. Dhakar, P. Pitchappa, F. Tay, and C. Lee, "An intelligent skin based self-powered finger motion sensor integrated with triboelectric nanogenerator," *Nano Energy*, 2015.
- [137] J. Chen *et al.*, "Harmonic-Resonator-Based Triboelectric Nanogenerator as a Sustainable Power Source and a Self-Powered Active Vibration Sensor," *Advanced Materials*, vol. 25, no. 42, pp. 6094-6099, 2013.
- [138] G. Zhu, J. Chen, T. Zhang, Q. Jing, and Z. L. Wang, "Radial-arrayed rotary electrification for high performance triboelectric generator," *Nature communications*, vol. 5, 2014.
- [139] Z. H. Lin, G. Cheng, L. Lin, S. Lee, and Z. L. Wang, "Water–Solid Surface Contact Electrification and its Use for Harvesting Liquid-Wave Energy," *Angewandte Chemie International Edition*, vol. 52, no. 48, pp. 12545-12549, 2013.
- [140] Y. Yang, H. Zhang, and Z. L. Wang, "Direct-Current Triboelectric Generator," *Advanced Functional Materials*, vol. 24, no. 24, pp. 3745-3750, 2014.
- [141] R. Hinchet and S. W. Kim, "Wearable and Implantable Mechanical Energy Harvesters for Self-Powered Biomedical Systems," *ACS Nano*, vol. 9, no. 8, pp. 7742-5, Aug 25 2015.
- [142] J. Chun *et al.*, "Boosted output performance of triboelectric nanogenerator via electric double layer effect," *Nat Commun*, vol. 7, p. 12985, Oct 05 2016.
- [143] X. H. Li, C. B. Han, L. M. Zhang, and Z. L. Wang, "Cylindrical spiral triboelectric nanogenerator," *Nano Research*, vol. 8, no. 10, pp. 3197-3204, 2015.
- [144] R. G. Horn and D. T. Smith, "Contact electrification and adhesion between dissimilar materials," *Science*, vol. 256, no. 5055, pp. 362-364, 1992.
- [145] H. Baytekin, A. Patashinski, M. Branicki, B. Baytekin, S. Soh, and B. A. Grzybowski, "The mosaic of surface charge in contact electrification," *Science*, vol. 333, no. 6040, pp. 308-312, 2011.
- [146] J. Lowell and A. Rose-Innes, "Contact electrification," *Advances in Physics*, vol. 29, no. 6, pp. 947-1023, 1980.
- [147] J. Sun, W. Li, G. Liu, W. Li, and M. Chen, "Triboelectric Nanogenerator Based on Biocompatible Polymer Materials," *The Journal of Physical Chemistry C*, vol. 119, no. 17, pp. 9061-9068, 2015.

- [148] K. N. Kim *et al.*, "Silk fibroin-based biodegradable piezoelectric composite nanogenerators using lead-free ferroelectric nanoparticles," *Nano Energy*, vol. 14, pp. 87-94, 2015.
- [149] F. R. Fan, Z. Q. Tian, and Z. L. Wang, "Flexible triboelectric generator," *Nano Energy*, vol. 1, no. 2, pp. 328-334, 2012.
- [150] B. Meng, W. Tang, X. S. Zhang, M. Han, W. Liu, and H. Zhang, "Self-powered flexible printed circuit board with integrated triboelectric generator," *Nano Energy*, vol. 2, no. 6, pp. 1101-1106, 2013.
- [151] P. Bai *et al.*, "Integrated Multilayered Triboelectric Nanogenerator for Harvesting Biomechanical Energy from Human Motions," *ACS Nano*, vol. 7, pp. 3713-3719, 2013.
- [152] Q. Zheng *et al.*, "In Vivo Self-Powered Wireless Cardiac Monitoring via Implantable Triboelectric Nanogenerator," *ACS Nano*, vol. 10, no. 7, pp. 6510-8, Jul 26 2016.
- [153] Q. Zheng *et al.*, "In vivo powering of pacemaker by breathing-driven implanted triboelectric nanogenerator," *Adv Mater*, vol. 26, no. 33, pp. 5851-6, Sep 3 2014.
- [154] Y. Ma *et al.*, "Self-Powered, One-Stop, and Multifunctional Implantable Triboelectric Active Sensor for Real-Time Biomedical Monitoring," *Nano Lett*, vol. 16, no. 10, pp. 6042-6051, Oct 12 2016.
- [155] Z. Li, G. Zhu, R. Yang, A. C. Wang, and Z. L. Wang, "Muscle-driven in vivo nanogenerator," *Adv Mater*, vol. 22, no. 23, pp. 2534-7, Jun 18 2010.
- [156] Q. Zheng *et al.*, "Biodegradable triboelectric nanogenerator as a life-time designed implantable power source," *Sci Adv*, vol. 2, p. e1501478, 2016.
- [157] X. S. Zhang *et al.*, "High-performance triboelectric nanogenerator with enhanced energy density based on single-step fluorocarbon plasma treatment," *Nano Energy*, vol. 4, pp. 123-131, 2014.
- [158] W. Tang, B. Meng, and H. Zhang, "Investigation of power generation based on stacked triboelectric nanogenerator," *Nano Energy*, vol. 2, no. 6, pp. 1164-1171, 2013.
- [159] S. Niu *et al.*, "Simulation method for optimizing the performance of an integrated triboelectric nanogenerator energy harvesting system," *Nano Energy*, vol. 8, pp. 150-156, 2014.
- [160] J. H. Burridge and D. L. McLellan, "Relation between abnormal patterns of muscle activation and response to common peroneal nerve stimulation in hemiplegia," *J Neurol Neurosurg Psychiatry*, vol. 69, pp. 353-361, 2000.
- [161] X. Y. Kang, J. Q. Liu, H. C. Tian, B. Yang, Y. NuLi, and C. S. Yang, "Fabrication and electrochemical comparison of SIROF, AIROF EIROF microelectrodes for neural interfaces," *IEEE Eng Med Biol Soc*, pp. 478-481, 2014.
- [162] R. D. Meyer, S. F. Cogan, T. H. Nguyen, and R. D. Rauh, "Electrodeposited iridium oxide for neural stimulation and recording electrodes," *IEEE T Neur Sys Reh*, vol. 9, no. 1, pp. 2-11, 2001.
- [163] S. Kakooei, M. C. Ismail, and B. A. Wahjoedi, "Electrochemical study of iridium oxide coating on stainless steel substrate," *Int J Electrochem Sci*, vol. 8, pp. 3290-3301, 2013.
- [164] D. T. Brocker and W. M. Grill, "Principles of electrical stimulation of neural tissue," *Handb Clin Neurol*, vol. 116, pp. 3-18, 2013.
- [165] J. E. Swett, Y. T. Torigoe, V. R. Elie, C. M. Bourassa, and P. G. Miller, "Sensory neurons of the rat sciatic nerve," *Exp Neurol*, vol. 114, pp. 82-103, 1991.
- [166] J. P. Oreardon, P. Chistancho, and A. D. Peshek, "Vagus nerve stimulation (VNS) and treatment of depression: To the brainstem and beyond," *Psychiatry*, vol. 3, no. 5, pp. 54-63, 2006.

- [167] D. A. Groves and V. J. Brown, "Vagal nerve stimulation: a review of its applications and potential mechanisms that mediate its clinical effects," *Neurosci Biobehav Rev*, vol. 29, no. 3, pp. 493-500, May 2005.
- [168] M. Gierthmuehlen and D. T. Plachta, "Effect of selective vagal nerve stimulation on blood pressure, heart rate and respiratory rate in rats under metoprolol medication," *Hypertens Res*, vol. 39, no. 2, pp. 79-87, Feb 2016.
- [169] S. Onuora, "Rheumatoid arthritis: Vagus nerve stimulation reduces RA severity in patients," *Nat Rev Rheumatol*, vol. 12, no. 9, p. 500, Sep 2016.
- [170] J. H. Duarte, "Heart failure: Vagal stimulation in patients with HF," *Nat Rev Cardiol*, vol. 11, no. 11, p. 621, Nov 2014.
- [171] H. U. Klein and G. M. Ferrari, "Vagus nerve stimulation: A new approach to reduce heart failure," *Cardiol J*, vol. 17, no. 6, pp. 638-643, 2010.
- [172] E. Vanoli, G. M. Ferrari, M. Stramba-Badiale, S. S. Hull, R. D. Forman, and P. J. Schwartz, "Vagal stimulation and prevention of sudden death in conscious dogs with a healed myocardial infarction," *Circ Res*, vol. 68, no. 5, pp. 1471-1481, 1991.
- [173] Z. Wang *et al.*, "Chronic intermittent low-level transcutaneous electrical stimulation of auricular branch of vagus nerve improves left ventricular remodeling in conscious dogs with healed myocardial infarction," *Circ Heart Fail*, vol. 7, no. 6, pp. 1014-21, Nov 2014.
- [174] E. M. Annoni *et al.*, "Intermittent electrical stimulation of the right cervical vagus nerve in salt-sensitive hypertensive rats: effects on blood pressure, arrhythmias, and ventricular electrophysiology," *Physiol Rep*, vol. 3, no. 8, Aug 2015.
- [175] M. Aalbers, J. Vles, S. Klinkenberg, G. Hoogland, M. Majoie, and K. Rijkers, "Animal models for vagus nerve stimulation in epilepsy," *Experimental Neurology*, vol. 230, no. 2, pp. 167-175, 2011.
- [176] W. Loscher, "Critical review of current animal models of seizures and epilepsy used in the discovery and development of new antiepileptic drugs," *Seizure*, vol. 20, no. 5, pp. 359-68, Jun 2011.
- [177] H. P. Buschman, C. J. Storm, D. J. Duncker, P. D. Verdouw, H. E. V. D. Aa, and P. V. D. Kemp, "Heart rate control via vagus nerve stimulation," *Neuromodulation*, vol. 9, pp. 214-220, 2006.
- [178] W. C. Groat and C. Tai, "Impact of bioelectronic medicine on the neural regulation of pelvic visceral function," *Bioelectron Med*, vol. 22, pp. 25-36, 2015.
- [179] T. F. Al-Shaiji, M. Banakhar, and M. M. Hassouna, "Pelvic electrical neuromodulation for the treatment of overactive bladder symptoms," *Adv Urol*, vol. 2011, p. 757454, 2011.
- [180] M. Slovak, C. R. Chapple, and A. T. Barker, "Non-invasive transcutaneous electrical stimulation in the treatment of overactive bladder," *Asian Journal of Urology*, vol. 2, no. 2, pp. 92-101, 2015.
- [181] J. N. Langley and M. B. Anderson, "The innervation of the pelvic and adjoining viscera," *J Physiol*, vol. 20, no. 4-5, pp. 372-406, 1896.
- [182] O. R. Langworthy, "Innervation of the pelvic organs of the rat," *Invest Urol*, vol. 2, pp. 491-511, 1965.
- [183] J. W. Lee, D. Kim, S. Yoo, H. Lee, G. H. Lee, and Y. Nam, "Emerging neural stimulation technologies for bladder dysfunctions," *Int Neurourol J*, vol. 19, no. 1, pp. 3-11, Mar 2015.

Appendix 1: Detailed fabrication process for Photosensitive Polyimide

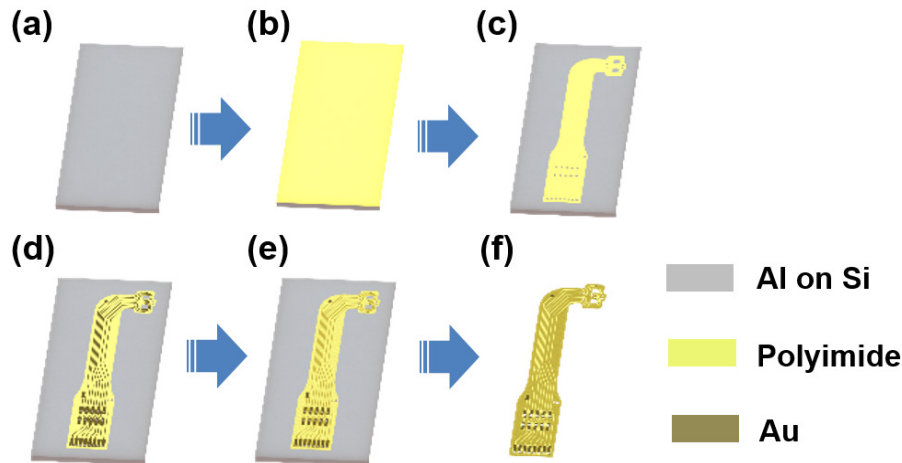


Figure A1. Fabrication process for photosensitive polyimide (Durimide 7505).

The flexible neural clip (FNC) consisted of a polyimide-Au-polyimide sandwiched structure fabricated by micro-electro-mechanical system (MEMS) technology. The fabrication process follows standard photolithographic and clean room procedures. Firstly, a 1 μm thick aluminum (Al) layer was evaporated onto the silicon substrate by physical vapor deposition (**Figure A1a**). It acted as a sacrificial layer to release the final device from the substrate. Then a 8 μm base layer of photosensitive polyimide (Durimide 7505, Fujifilm, Japan) was spun onto the Al coated substrate with a speed of 2000 rpm (**Figure A1b**). After exposure under ultraviolet (UV) light with a dosage of 120 mJ cm^{-2} , the base layer was post-baked and developed in HTRD2 and RER 600 (Fujifilm, Japan), which defined the bottom layer pattern of the FNC. The base polyimide layer was cured at 200 $^{\circ}\text{C}$ in N_2 for 30 minutes. In this way, it creates a chemically and physically stable surface for further processing (**Figure A1c**).

After that, a layer of AZ 9260 (AZ Electronic Materials, USA) was spun onto the polyimide base layer. This AZ layer was exposed and the electrode traces were patterned. A layer of 20 nm chrome (Cr) was deposited to improve the adhesion of the next conduction layer by sputtering. After a 250 nm gold layer was deposited, the conductive metal layer was patterned by a lift-off process in acetone (**Figure A1d**). Another 8 μm top layer of polyimide was spun onto the processed metal layer, and patterned to expose the sensing contacts and connection pads (**Figure A1e**). Then, we adopted an anodic metal dissolution approach to release the whole device that not only ensured a flat planar structure was released (**Figure. A1f**), but also was significantly faster than the traditional wet etching process. Briefly, the wafer was immersed in a 2 M NaCl solution, and connected to an external positive terminal of a voltage source at 1 V. A platinum (Pt) mesh electrode was connected to the negative terminal. A magnetic stir bar was also put inside the solution to keep the concentration of NaCl uniform. After around 20 minutes, the exposed portions of the Al sacrificial layer were removed, and only the covered portions of the Al sacrificial layer were left. Since the contact area between the Al sacrificial layer and the NaCl solution decreased, the current dropped, and the Al etching rate was reduced. Thus, the voltage was then increased to 20 V to speed up the release process. After the entire Al sacrificial layer was removed after 2 hours, the final device was released. The pads of the electrodes can be connected to FPC connectors (Hirose Electric Co. Ltd.), customized Omnetics connectors (Omnetics Connector Corp., MN, USA).

Appendix 2: Rat Preparation for *in vivo* experiments

Adult female Sprague-Dawley rats (200-300g) were used for acute *in vivo* experiments in this study. All procedures were performed in accordance with protocols approved by the Institutional Animal Care and Use Committee of the National University of Singapore. The methods were carried out in accordance with the 143/12 protocol. For each experiment, the rat was anesthetized with a mixture (0.2 ml/100 g) of ketamine (37.5 mg/ml) and xylazine (5 mg/ml) intraperitoneally (I.P.), and supplementary doses of 0.1 ml/ 100 g were injected for maintenance.

For the sciatic nerve branch experiments, after an adequate depth of anesthesia was attained, the right sciatic nerves were exposed through a gluteal-splitting incision for flexible epineural strip electrodes (FLESEs), flexible splitting electrode, and flexible and adjustable sling electrodes. The FNCs were implanted on the sciatic nerve branches. For the vagus nerve experiment (N = 3 rats), the right vagus nerves were exposed carefully then, the FNCs were implanted. For the bladder experiment (N = 1 rat), the animal was placed in the supine position, and a ventral midline incision of the lower abdomen was first made to expose the bladder and then extended laterally to expose the pelvic nerve. The underlying muscles were cut, and adipose and connective tissues were removed or pushed aside to expose about 2 mm of the nerve for electrode implantation.

Appendix 3: List of Publication and Award

Journal Paper

1. **Sanghoon Lee**, Wendy Yen Xian Peh, Jiahui Wang, Fengyuan Yang, John S. Ho, Nitish V. Thakor, Shih-Cheng Yen, and Chengkuo Lee, “Toward Bioelectronic Medicine- Neuromodulation of Small Peripheral Nerves Using Flexible Neural Clip (FNC)”, **Adv. Sci. (Wiley)**, To be published.
2. **Sanghoon Lee**, Hao Wang, Qiongfeng Shi, Lokesh Dhakar, Jiahui Wang, Nitish V. Thakor Shih-Cheng Yen, and Chengkuo Lee, “Development of battery-free neural interface and modulated control of tibialis anterior muscle via common peroneal nerve based on triboelectric nanogenerators (TENGs)”, **Nano Energy**, vol. 33, pp. 1-11, 2017.
3. **Sanghoon Lee**, Swathi Sheshadri, Zhuolin Xiang, Ignacio Delgado Martinez, Ning Xue, Tao Sun, Nitish V. Thakor, Shih-Cheng Yen and Chengkuo Lee, “Selective stimulation and neural recording on peripheral nerves using flexible split ring electrodes”, **Sensors and Actuators B: Chemical**, vol. 242, pp. 1165-1170, 2017.
4. **Sanghoon Lee**, Shih-Cheng Yen, Swathi Sheshadri, Ignacio Delgado Martinez, Ning Xue, Zhuolin Xiang, Nitish V. Thakor and Chengkuo Lee, Flexible Epineural Strip Electrode (FLESE) for Recording in Fine Nerves, **IEEE Trans. Biomed. Eng.**, vol. 63, no. 3, pp. 581-587, 2016.
5. Zhuolin Xiang, Swathi Sheshadri, **Sang-Hoon Lee**, Jiahui Wang, Ning Xue, Nitish V. Thakor, Shih-Cheng Yen and Chengkuo Lee, “Mapping of Small Nerve Trunks and Branches Using Adaptive Flexible Electrodes”, **Adv. Sci. (Wiley)**. 3, 9, 1500386 (2016).
6. Zhuolin Xiang, Shih-Cheng Yen, Swathi Sheshadri, Jiahui Wang, **Sanghoon Lee**, Yu-Hang Liu, Lun-De Liao, Nitish V. Thakor, and Chengkuo Lee, “Progress of Flexible Electronics in Neural Interfacing – A self-Adaptive Non-Invasive Neural Ribbon Electrode for Small Nerves Recording”, **Adv. Mat.** 28, 22, 4472-4479 (2016).
7. Ning Xue, Tao Sun, Wei Mong Tsang, Ignacio Delgado-Martinez, **Sanghoon LEE**, Swathi Sheshadri, Zhoulin Xiang, Srinivas Merugu, Yuandong Gu, Shih-Cheng Yen and Nitish V. Thakor, “Polymeric C-shaped Cuff Electrode for Recording of Peripheral Nerve Signal, **Sensors and Actuator B: Chemical**, 210, pp.640-648, (2015).

Conference Paper

1. **Sanghoon Lee**, Wendy Yen Xian Peh, Jiahui Wang, Nitish V. Thakor Shih-Cheng Yen, and Chengkuo Lee “Vagus nerve stimulation (VNS) for heart rate control using novel neural interfaces”, **The 19th International Conference on Solid State Sensors, Actuators and Microsystems (Transducer 2017)**, Kaohsiung, Taiwan, June 18-22, Transducer 2017.
2. **Sanghoon Lee**, Hao Wang, Qiongfeng Shi, Lokesh Dhakar, Jiahui Wang, Nitish V. Thakor Shih-Cheng Yen, and Chengkuo Lee, “Combining neural electrodes and triboelectric nanogenerators (TEGs) to enable a self-sustainable platform for neuromodulation”, **The 19th International Conference on Solid State Sensors, Actuators and Microsystems (Transducer 2017)**, Kaohsiung, Taiwan, June 18-22, 2017.
3. **Sanghoon Lee**, Shih-Cheng Yen, Lun-De Liao, Gil Gerald Lasam Gammad, Nitish V. Thakor and Chengkuo Lee, “Flexible sling electrode for bidirectional neural signal recording and selective stimulation”, **The 29th IEEE International Conference on Micro Electro Mechanical Systems (MEMS 2016)**, Shanghai, China, Jan. 24-28, 2016.
4. Jiahui Wang, Zhuolin Xiang, **Sanghoon Lee**, Rangarajan Jegadeesan, Shih-Cheng Yen, Nitish V. Thakor, and Chengkuo Lee, “Flexible multi-channel muscle electrode for functional electrical stimulation and in-vivo ph monitoring”, **The 29th IEEE International Conference on Micro Electro Mechanical Systems (MEMS 2016)**, Shanghai, China, Jan. 24-28, 2016.
5. Zhuolin Xiang, **Sanghoon Lee**, Jiahui Wang, Nitish V. Thakor and Chengkuo Lee, “Development of self-adaptive noninvasive neural ribbon electrodes for small nerve applications”, **Intern. Conf. on BioElectronics, BioSensor, BioMedical Devices, BioMEMS/NEMS and Applications 2015 (Bio4Apps 2015)**, I-2, Fukuoka, Japan, Dec. 9-11, 2015.
6. Zhuolin Xiang, Shih-Cheng Yen, Swathi Sheshadri, Ning Xue, **Sanghoon Lee**, Jiahui Wang, Nitish V. Thakor, and Chengkuo Lee, “Flexible and Self-Adaptive Neural Ribbon with Three-Dimensional Electrodes for Sciatic Nerve Recording”, **IEEE Engineering in Medicine and Biology Society (EMBS)**, Milan, Italy, August 25-29, 2015.
7. **Sanghoon Lee**, Swathi Sheshadri, Ning Xue, Tao Sun, Chengkuo Lee, Nitish V. Thakor, Shih-Cheng Yen, and Ignacio Delgado-Martínez, “Selective stimulation of peripheral motor nerve using a flexible split-ring electrode”, **7th International IEEE EMBS Neural Engineering Conference**, Montpellier, France, April. 22 – 24th, 2015.
8. **Sanghoon Lee**, Swathi Sheshadri, Ignacio Delgado Martinez, Xue Ning, Zhuolin Xiang, Kian Ann Ng, Anoop Patil, Shih-Cheng yen, Nitish V. Thakor and Chengkuo Lee, Tripolar Sling Electrode for Neural Signal Recording of

Sciatic Nerve, **The 6th International Symposium on Microchemistry and Microsystems (ISMM 2014)**, pp. 200-201, Singapore, Jul. 29 – Aug. 1, 2014.

9. **Sanghoon Lee**, Xue Ning, Xiang Zhuolin, Ignacio Delgado Martinez, Kian Ann NG, Swathi Sheshadri, Sun Tao, Shih-Cheng Yen, Nitish V. Thakor, LEE Chengkuo, “Flexible sling electrode for neural signal recording”, **7th Asia-Pacific Conference on Transducers and Micro/Nano Technologies (APCOT 2014)**, Daegu, Korea, Republic of Korea, June 29 – July 2, 2014.

Award

1. **Best Paper Award (Gold)** recipients for Annual Seminar 2015, Korea-Singapore International Global Health Forum held by Korean Scientist and Engineers Association in Singapore (KSEASG)

Sanghoon Lee

The winning entry is entitled “Selective Recording and Stimulation on Peripheral Nerves using Flexible Epineural Electrodes for Electroceuticals”.

2. **Best Paper Award (2nd Place)** recipients for Graduate Student Symposium (GSS) 2014 held by Department of Electrical and Computer Engineering, National University of Singapore

Sanghoon Lee

The winning entry is entitled “Tripolar sling electrode for neural signal recording of sciatic nerve”.